DISSERTATION

CHARACTERIZING REACTION AND TRANSPORT PROCESSES IN AN ELECTROLYTIC REACTOR FOR IN SITU GROUNDWATER TREATMENT

Submitted by

Matthew Alan Petersen

Department of Chemical & Biological Engineering

In partial fulfillment of the requirements

For the Degree of Doctor of Philosophy

Colorado State University

Fort Collins, Colorado

Spring 2007

COLORADO STATE UNIVERSITY

February 7, 2007

WE HEREBY RECOMMEND THAT THE DISSERTATION PREPARED UNDER OUR SUPERVISION BY MATTHEW ALAN PETERSEN ENTITLED **CHARACTERIZING REACTION AND TRANSPORT PROCESSES IN AN ELECTROLYTIC REACTOR FOR IN SITU GROUNDWATER TREATMENT** BE ACCEPTED AS FULLFILLING IN PART REQUIREMENTS FOR THE DEGREE OF DOCTOR OF PHILOSOPHY.

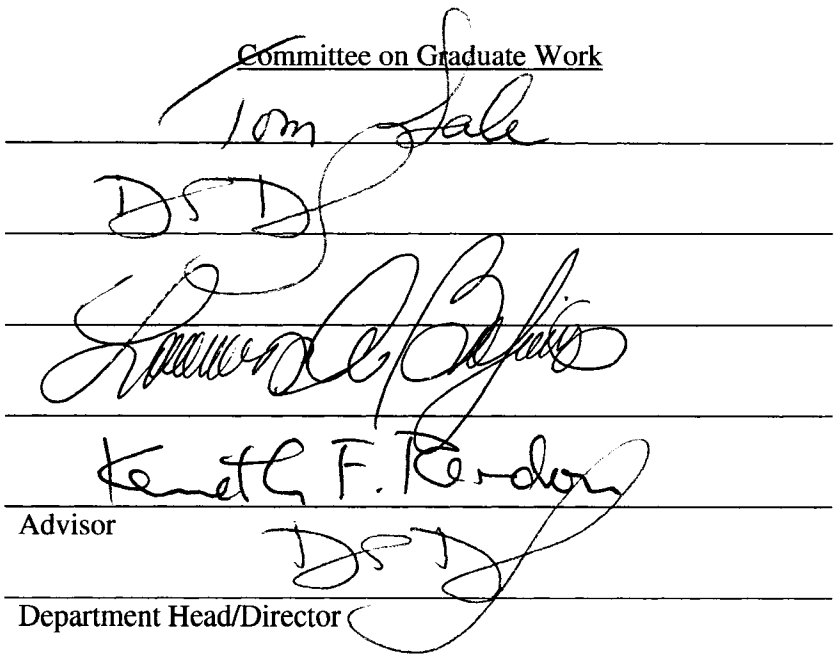

Committee on Graduate Work

Advisor

Department Head/Director

ABSTRACT OF DISSERTATION

CHARACTERIZING REACTION AND TRANSPORT PROCESSES IN AN ELECTROLYTIC REACTOR FOR IN SITU GROUNDWATER TREATMENT

Groundwater contamination poses a long-term threat to subsurface water resources. Effective mitigation of the risk posed by migrating contaminant plumes requires sustainable strategies and technologies due to the expected longevity of contaminant source and plume lifetimes. Electrochemical-based plume control systems have the potential to meet niche applications in a sustainable manner. A commonly proposed technology format for in situ plume control is a permeable reactive barrier (PRB). Effectively deploying an electrolytic reactor in this format requires a fundamental understanding of reaction and transport processes that occur over multiple length scales to properly design and assess system performance.

The governing processes in an electrolytic PRB were characterized using an integrated experimental and modeling approach. The PRB utilized thin expanded mesh electrodes consisting of a titanium substrate coated with a binary mixture of TiO_2 and IrO_2 (Ti/MMO). The first objective of this research was to address the effectiveness of Ti/MMO as a cathode substrate in terms of the ability to degrade model contaminant mixtures and material stability. Nitroaromatic and heterocyclic nitramines were the model contaminants. Nitro-group reduction at the metal oxide surface was found to occur via an adsorbed hydrogen atom by a mechanism that did not include rate inhibition when multiple species were present. Prolonged cell operation led to depletion of surface

roughness on the convex front face of the mesh geometry. Reaction rates increased on the smoother aged surface, indicating that mass transfer limitations to active sites on the surface were diminished. The second objective of this research was to elucidate the distribution of reaction conditions over the mesh electrode surface. Using a computational fluid dynamics model to explore the implications of mesh geometry on current density distribution, new electrode geometries were evaluated. The current density distribution was predicted to flatten, resulting in larger overall flux reduction rates when less accessible regions within the mesh aperture were deemphasized. The third overall research objective was to examine and quantify the effect of gas-induced mixing within the electrode assembly on system performance. Gas evolution that normally occurs concomitant with contaminant degradation served to mix the fluid within the electrode assembly effectively enough that reactor performance resembled a continuously-stirred tank reactor at very low flowrates.

These results illustrate the effectiveness of metal oxide electrodes to reduce organic contaminants, a substrate not previously explored in this type of application, in a thin cross-flow reactor. Additionally, this study lays a foundation for further development of the electrochemical-based remediation systems, and exploring new cathode materials and deployment platforms for environmental technologies.

Matthew Alan Petersen
Department of Chemical & Biological Engineering
Colorado State University
Fort Collins, CO 80523
Spring 2007

ACKNOWLEDGEMENTS

Many individuals contributed to research presented in this dissertation. I would like to acknowledge my advisor, Dr. Ken Reardon, and dissertation committee members Dr. Tom Sale, Dr. Dave Dandy, and Dr. Larry Belfiore, for their input, time, and constructive criticism throughout this project. I would like to thank Dr. Reardon for his guidance and friendship throughout my time in the research group. I would also like to thank Dr. Sale and Dr. Dave Gilbert for their support, encouragement, and friendship over the 5½ years that spent working together on electrolytic remediation systems in the laboratory and field.

Several others have contributed technical and/or moral support to this research: Don Dick and Dr. Pat McCurdy for assistance with chromatography, spectroscopy, and microscopy methods, Brian Vencalek for his assistance with the transient tracer experiments, other staff and students in the Center for Contaminant Hydrology, and students in the KFR lab for letting me bore them with my group meeting talks.

I have utilized financial support from the US Department of Defense ESTCP program and the University Consortium for Field Focused Groundwater Contamination Research. I would like to thank each of these organizations for their support of our program.

Finally, I would like to express a deep amount of gratitude to my friends and family for their companionship, support, and tolerance during the rough times of this process. I would especially like to thank my wife, Kristin, for her love and encouragement throughout this experience, and I look forward to where our next steps take us.

TABLE OF CONTENTS

LIST OF FIGURES

LIST OF TABLES

CHAPTER I:

CHALLENGES TO THE CONTROL OF GROUNDWATER CONTAMINANT PLUMES

The development of solutions to manage environmental contamination, specifically for groundwater resources, has been a research thrust for public and private sector stakeholders since the mid 1980s (NRC, 1994; Pankow et al., 1996; NRC, 1997; Shackelford and Jefferis, 2000; NRC, 2005). Over that timespan, the focus of research and development has shifted to more pragmatic and cost effective technologies and site-care strategies. Central to this are efforts to develop a more fundamental understanding of the underlying processes that govern specific remediation or containment approaches. The overarching goal of this research is to elucidate the underlying mechanisms of an innovative plume control technology that utilizes controlled electrochemically-driven processes.

1.1 General Problem Description

Groundwater contamination sites have the potential to be very complex geomorphologically, hydrologically, geochemically, and biologically. Furthermore, the distribution and form of contaminant species within the aquifer is heterogeneous

(Boulding and Ginn, 2004). A conceptual contaminated site illustrating a portion of these complexities is presented in Figure 1-1. All of these aspects impact the selection and design of a strategy to mitigate the risk posed by the presence of the contaminant species. A major point in the remedial action decision process is the projected benefit of removing the contamination source footprint. Often, the benefit of removing released source material from the subsurface is insufficient to justify omitting further steps to remediate the downstream zones (i.e., signal or receptor zone in Figure 1-1) (Kavanaugh et al., 2003).

Actions taken to control the signal from source footprints (plumes) are often necessary when contamination receptors are dispersed (e.g., surface water resources) or include multiple stakeholders (e.g., cross property boundaries). Technologies that can be deployed in situ have become popular tools because of their relatively small operating cost compared to pump and treat techniques. Several challenges to effectively reducing or controlling groundwater contamination plumes exist. Two primary concerns are the site-specific recalcitrance of the contaminant, or contaminant mixtures, and the degree of geologic heterogeneity in the aquifer. Site-specific recalcitrance and heterogeneity may sustain concentrations within a plume through competition/inhibition in the case of mixtures (Semprini et al., 1991; Tratnyek et al., 2001; Klausen et al., 2003) and matrix diffusion processes (Sudicky et al., 1985; Broholm et al., 1999). Additionally, formation heterogeneity can impose a wide distribution of groundwater velocities through a single treatment zone (Eykholt et al., 1999; Benner et al., 2001). This can further complicate system design and performance monitoring. The motivation to use applied electrochemical systems is based on the assumption that more effective in situ

remediation technologies can be developed by taking advantage of electrolytic processes to overcome the background environmental conditions.

1.2 System Description

The proposed electrochemical system consists of closely spaced (e.g., 1 cm) permeable planar electrodes emplaced below the subsurface to intercept a plume of contaminated groundwater (Figure 1-2). Applying a low voltage potential difference between the electrodes induces oxidizing conditions at the anode (positive electrode) and reducing conditions at the cathode (negative electrode). In this configuration, the dissolved contaminants are subjected to sequential oxidation-reduction or reduction–oxidation, depending on the configuration of the cell. The proposed system consists of three integrated components: the electrode material, the electrode assembly, and the assembly support. The electrode assembly ensures that the physical environment in which the electrodes are emplaced allows flow through the barrier and keeps the conductive components electrically isolated. The assembly support is the structure necessary for installation of the system, and prevents contaminated groundwater from by-passing the electrodes.

The electrodes used in the system are an expanded titanium mesh coated with a binary mixture of transition metal oxides (Ti/MMO). The selection of Ti/MMO is based on its structural and chemical stability over a wide range of applied electrical potentials. This allows for flexibility in the polarity configuration during normal operation (i.e., oxidation-reduction or reduction-oxidation) and precipitate control strategies (i.e., periodic polarity reversal). Ti/MMO electrodes fall under the general classification of

materials known as dimensionally stable electrodes (DSEs). DSEs have been widely reported as effective substrates for oxidizing organic pollutants either through direct electron transfer at the electrode surface (Rodgers et al., 1999; Panizza and Cerisola, 2003, 2004) or by generating non-specific oxidizing agents such as hydroxyl radicals (Comninellis and Pulgarin, 1993; Rodgers et al., 1999; Kim et al., 2002; Pelegrino et al., 2002; Panizza and Cerisola, 2003, 2004). Characterization of cathodically polarized DSEs have focused only on the hydrogen evolution reaction (Kötz and Stucki, 1987; Kodintsev and Trasatti, 1994; Burke and Naser, 2005).

The electrode assembly is a composite of three materials (Figure 1-3). It consists of the electrodes sandwiched between layers of high-density polyethylene geonet as the electrode spacer, and geotextile fabric on the external surfaces to prevent infiltration of backfill into the assembly. The use of geonet between the electrodes provides a very high porosity and permeability zone within the active area of the system. This serves several functions, including the provision of:

1 a large permeability contrast between the system and the surrounding formation, which convergences flow into the electrodes,
2 seepage velocities through the system that are lower than that of the formation, allowing for greater residence time than a porous reactive substrate,
3 a path for H_2 and O_2 gas, products of water electrolysis, to escape the system in a safe manner.

Electrode spacing can be varied depending on site-specific conditions (e.g., specific conductivity of groundwater) to limit the power requirement. Typical spacing distances implemented have been from 1 to 2.5 cm.

The most convenient approach to system fabrication and installation is to use a modular design for the assembly support. Suitable materials used for the assembly support are non-conductive (electrically and hydraulically), sealable between individual modules, compatible with the contaminants present, and cost practical.

1.3 Research Objectives and Approach

The underlying mechanisms of the proposed system were elucidated using an integrated experimental and modeling approach. The specific studies presented in this dissertation identify and explore reaction and transport processes that occur over a range of characteristic length scales (e.g., surface oxide layer depth → mesh aperture width → electrode sheet height). This approach was undertaken to deconvolute the system and reconstruct a process-oriented conceptual model of the technology over multiple length scales. This system perspective will allow for better understanding of technology advantages/limitations, and ease translating insights acquired to future studies.

Starting from a microscopic perspective, reactions of organic molecules at a Ti/MMO *cathode* are not very well understood. The first objective of this research was to address the issues related to utilizing Ti/MMO as a cathode substrate in terms of ability to degrade model contaminants and material stability. Reduction reactions at oxide-water interfaces have been well described for less noble metals, such as iron (Scherer et al., 1999), compared to those employed in the present MMO system. Furthermore, from

inspection of the standard reduction potentials for most transition metal oxides, the high oxidized state of the transition metals while under cathodic polarization (especially in the realm of H_2 gas evolution) is not the preferred thermodynamic state. Using a mixture of nitroaromatics and heterocyclic nitramines as model contaminants, the reduction mechanism for this important class of groundwater contaminant was investigated on both fresh and aged cathodes. Fresh and aged cathodes were used to investigate the impact of prolonged cathodic polarization on Ti/MMO electrodes.

The second objective of this research was to elucidate the distribution of reaction conditions over a mesh electrode surface. This was accomplished using a three-dimensional numerical model of a representative element of system volume. The research objective transfers the focus from a particular electrochemical system to the vehicle in which that system is deployed in an application. Specifically, the Ti/MMO material is configured into a thin expanded mesh, which is then placed perpendicular to the hydraulic gradient such that flow is through the mesh apertures. The resulting structure is similar to a honeycomb monolith reactor. However, in diffusion controlled environments such as groundwater systems, diffusion to the electrode mesh surface may be the rate-limiting process due to the short residence time through the thin electrode assembly.

The third objective of this research was to examine and quantify the effect of gas-induced mixing within the electrode assembly on system performance. Gas-evolution from the electrolysis of water is often concomitant with contaminant degradation in this system. The non-ideal flow through the electrode assembly may affect how reactants are distributed within the assembly. This can ultimately lead to different reactor behavior

than would be observed under ideal flow conditions. Specifically, gas-evolution induced mixing has been shown to increase two processes in heterogeneous reaction systems. First, from a macroscopic perspective, dispersion coefficient generally increases to reflect the large-scale mixing that occurs (Wu et al., 1993). Second, from a microscopic perspective, mass-transport can be enhanced from the bulk liquid phase to the electrode surface by agitating the fluid near the point of bubble formation and detachment (Janssen, 1987; Shah and Jorne, 1989; Bisang, 1993; Wu and Rangaiah, 1993). Cross-flow through a thin mesh is a novel electrolysis cell configuration, and the implications of gas evolution on system performance in this configuration were necessary to understand.

Assembling each of these three objectives into an overall project architecture (Figure 1-4) illustrates how they can be utilized to develop a foundation for system analysis.

1.4 Document Organization

This dissertation is organized into three separate studies, each addressing one of the three research objectives described in the previous section. The document has been organized into the following chapters, listing more specific aims after each chapter title:

Chapter II:Impact of Electrode Surface Morphology on the Electrochemical Reduction Kinetics of Nitroaromatics and Heterocyclic Nitramines Mixtures

- Develop a mechanistic interpretation of the reduction kinetics using a mixture of heterocyclic nitramines and nitroaromatics.

- Evaluate the impact of electrode aging on oxide surface morphology and composition.
- Propose a conceptual model of surface evolution, and the ultimate impact on reduction kinetics.

Chapter III: ***The Influence of Electrode Geometry on the Distribution of Reaction Conditions Over a Three-Dimensional Mesh Electrode Surface***

- Visualize how surface reaction and transport conditions are distributed over the mesh electrode surface.
- Elucidate how that distribution changes as a function of electrode geometry.

Chapter IV: Modeling Contaminant Mass Transport and Degradation in a Gas-Evolving Electrolytic Permeable Reactive Barrier

- Identify the macroscopic manifestations of gas evolution at the electrode surface and mixing within the electrode assembly.
- Assemble a toolset to understand the non-ideal processes in the system that potentially impact overall performance.

Chapter V: Conclusions and Relevance to Future Work

- Organize results of studies into an overarching framework for system analysis
- Identify future areas of research

1.5 References

Benner, S.G., Blowes, D.W.,Molson, J.W.H., 2001. Modeling preferential flow in reactive barriers: Implications for performance and design. Ground Water 39, 371-379.

Bisang, J.M., 1993. Effect of Mass Transfer on the Current Distribution in Monopolar and Bipolar Electrochemical Reactors with a Gas-Evolving Electrode. Journal of Applied Electrochemistry 23, 966-974.

Boulding, J.R.,Ginn, J.S., 2004. Practical Handbook of Soil, Vadose Zone, and Ground-Water Contamination: Assessment, Prevention, and Remediation. Lewis Publishers, Boca Raton, FL.

Broholm, K., Feenstra, S.,Cherry, J.A., 1999. Solvent release into a sandy aquifer. 1. Overview of source distribution and dissolution behavior. Environmental Science and Technology 33, 681-690.

Burke, L.D.,Naser, N.S., 2005. Metastability and electrocatalytic activity of ruthenium dioxide cathodes used in water electrolysis cells. Journal of Applied Electrochemistry 35, 931-938.

Comninellis, C.,Pulgarin, C., 1993. Electrochemical oxidation of phenol for wastewater treatment using SnO_2 anodes. Journal of Applied Electrochemistry 23, 108-112.

Eykholt, G.R., Elder, C.R.,Benson, C.H., 1999. Effects of aquifer heterogeneity and reaction mechanism uncertainty on a reactive barrier. Journal of Hazardous Materials 68, 73-96.

Janssen, L.J.J., 1987. Mass Transfer at Gas-Evolving Vertical Electrodes. Journal of Applied Electrochemistry 17, 1177-1189.

Kavanaugh, M.C., Rao, P.S., Abriola, L., Cherry, J.A., Newell, C., Sale, T., Destouni, G., Falta, R., Shoemaker, S., Siegrist, R., Major, D., Mercer, J., Teutsch, G.,Udell, K., 2003. The DNAPL Remediation Challenge: Is there a Case for Source Depletion? US Environmental Protection Agency

Kim, K.-W., Lee, E.-H., Kim, J.-S., Shin, K.-H.,Jung, B.-I., 2002. A study on performance improvement of Ir oxide-coated titanium electrode for organic destruction. Electrochimica Acta 47, 2525-2531.

Klausen, J., Vikesland, P.J., Kohn, T., Burris, D.R., Ball, W.P.,Roberts, A.L., 2003. Longevity of granular iron in groundwater treatment processes: Solution composition effects on reduction of organohalides and nitroaromatic compounds. Environmental Science and Technology 37, 1208-1218.

Kodintsev, I.M.,Trasatti, S., 1994. Electrocatalysis of H_2 evolution on RuO_2 + IrO_2 mixed oxide electrodes. Electrochimica Acta 39, 1803-1808.

Kötz, E.R.,Stucki, S., 1987. Ruthenium dioxide as a hydrogen-evolving cathode. Journal of Applied Electrochemistry 17, 1190-1197.

NRC, 1994. Alternative for Ground Water Cleanup. National Academies Press, Washington, DC.

NRC, 1997. Innovations in Ground Water and Soil Cleanup: From Concept to Commercialization. National Academy Press

NRC, 2005. Contaminants in the Subsurface: Source Zone Assessment and Remediation. The National Academies Press, Washington, D.C.

Panizza, M.,Cerisola, G., 2003. Influence of anode material on the electrochemical oxidation of 2-naphthol: part 1. cyclic voltammetry and potential step experiments. Electrochimica Acta 48, 3491-3497.

Panizza, M.,Cerisola, G., 2004. Influence of anode material on the electrochemical oxidation of 2-naphthol: part 2. bulk electrolysis experiments. Electrochimica Acta 49, 3221-3226.

Pankow, J.F., Feenstra, S., Cherry, J.A.,Ryan, M.C., 1996. Dense chlorinated solvents in groundwater: background and history of the problem. In: Pankow, J.F. and Cherry, J.A. (Eds.). Dense Chlorinated Solvents and other DNAPLs in Groundwater. Waterloo Press, Portland, OR, pp. 1-52.

Pelegrino, R.L., Di Iglia, R.A., Sanches, C.G., Avaca, L.A.,Bertazzoli, R., 2002. Comparative study of commercial oxide electrodes performance in electrochemical degradation of organics in aqueous solutions. Journal of the Brazilian Chemical Society 13, 60-65.

Rodgers, J.D., Jedral, W.,Bunce, N.J., 1999. Electrochemical oxidation of chlorinated phenols. Environmental Science and Technology 33, 1453-1457.

Scherer, M.M., Balko, B.A.,Tratnyek, P.G., 1999. The role of oxides in reduction reactions at the metal-water interface. ACS Symposium Series 715, 301-322.

Semprini, L., Hopkins, G.D., Roberts, P.V., Grbicgalic, D.,Mccarty, P.L., 1991. A Field-Evaluation of Insitu Biodegradation of Chlorinated Ethenes .3. Studies of Competitive-Inhibition. Ground Water 29, 239-250.

Shackelford, C.D.,Jefferis, S.A. (**2000**). Geoenvironmental engineering for in situ remediation. International Conference on Geotechnical and Geoenvironmental Engieering (GeoEng2000), Melbourne, Australia.

Shah, A.,Jorne, J., 1989. Mass transfer under bubble-induced convection in a vertical electrochemical cell. Journal of the Electrochemical Society 136.

Sudicky, E.A., Gillham, R.W.,Frind, E.O., 1985. Experimental Investigation of Solute Transport in Stratified Porous-Media .1. The Nonreactive Case. Water Resources Research 21, 1035-1041.

Tratnyek, P.G., Scherer, M.M., Deng, B.L.,Hu, S.D., 2001. Effects of natural organic matter, anthropogenic surfactants, and model quinones on the reduction of contaminants by zero-valent iron. Water Research 35, 4435-4443.

Wu, W.S.,Rangaiah, G.P., 1993. Effect of Gas Evolution on Mass Transfer in an Electrochemical Reactor. Journal of Applied Electrochemistry 23, 1139-1146.

Wu, W.S., Rangaiah, G.P.,Fleischmann, M., 1993. Effect of Gas Evolution on Dispersion in an Electrochemical Reactor. Journal of Applied Electrochemistry 23, 113-119.

Figures

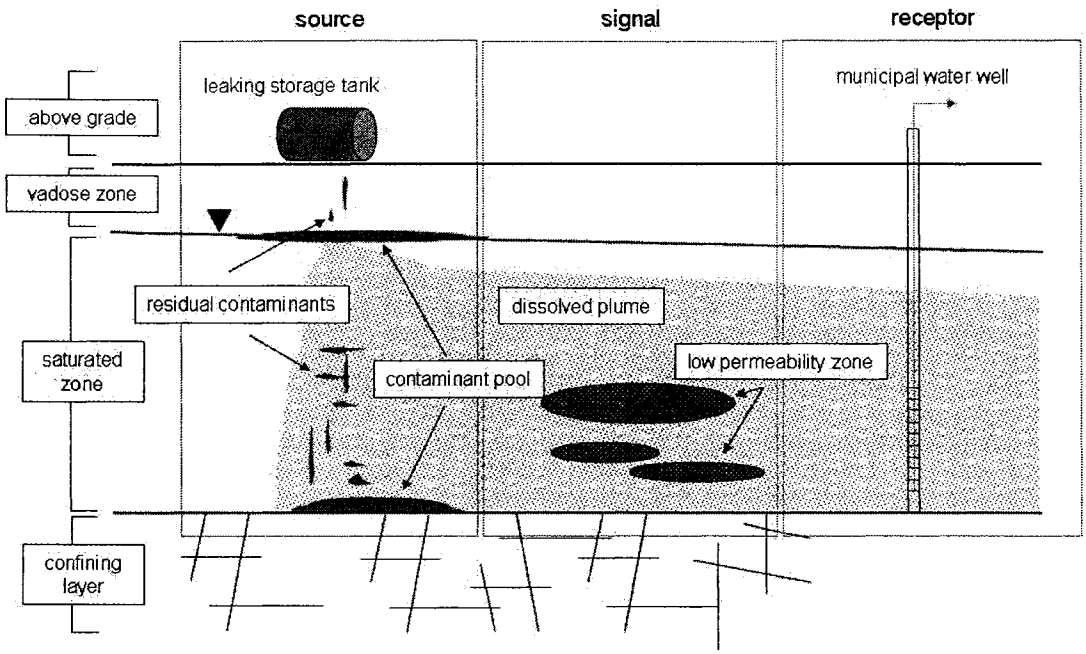

Figure 1-1 Conceptual interpretation of a typical contaminated groundwater site.

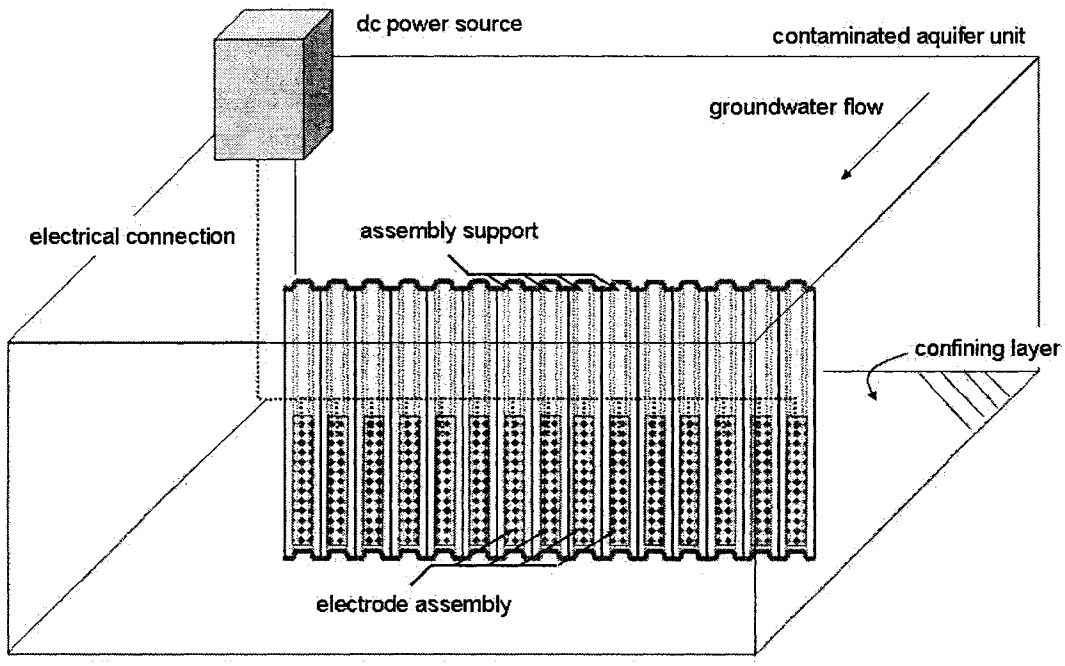

Figure 1-2 Diagram of a field-scale implementation illustrating the electrode assembly and assembly support.

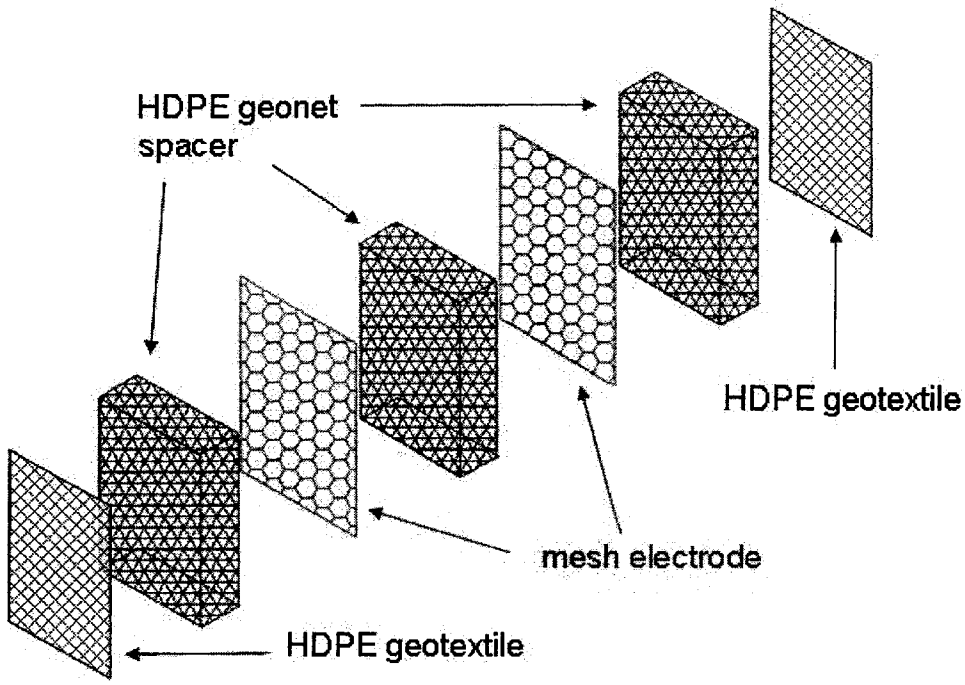

Figure 1-3 Detailed diagram of the electrode assembly.

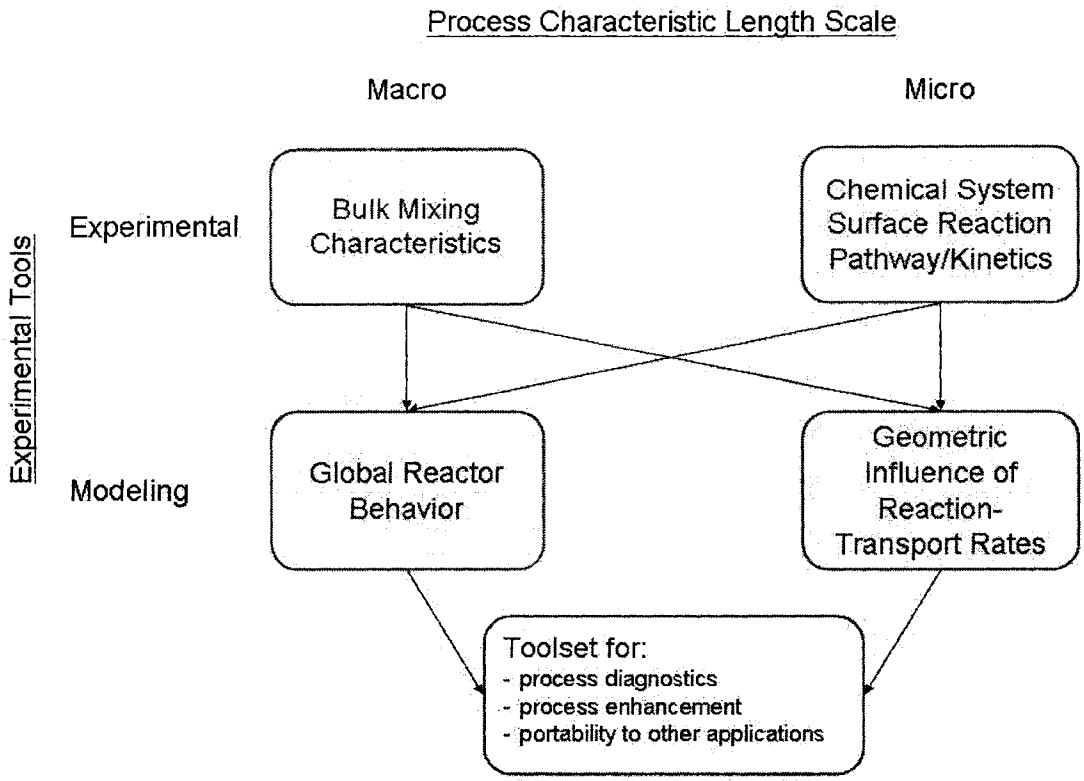

Figure 1-4 Research project architecture illustrating the relationships between individual studies.

CHAPTER II:

IMPACT OF ELECTRODE SURFACE EVOLUTION ON THE ELECTROCHEMICAL REDUCTION KINETICS OF NITROAROMATIC AND HETEROCYCLIC NITRAMINE MIXTURES

Abstract

Utilizing electrochemical processes to manage aquifers contaminated with heterocyclic nitramines and nitroaromatic may circumvent challenges presented by recalcitrance, range of physicochemical properties of these compounds, and by their occurrence as mixtures within the environment. The evolution of electrode surface over the lifetime of an implementation adds to the difficulty of designing an appropriate technology solution. Utilizing a TiO_2/IrO_2 coated titanium substrate as the cathode (Ti/MMO), the reduction kinetics of hexahydro-1,3,5-trinitro-1,3,5-triazine (RDX) and 2,4,6-trinitrotoluene (TNT) were investigated on fresh and aged cathodes. The mechanistic interpretation of reaction kinetics for RDX and TNT mixtures suggests that electron transfer to the target compounds proceeds via a mediator species, specifically, adsorbed atomic hydrogen. Correspondingly, reaction rates were relatively fast compared to other commonly studied reaction substrates, and competition for active surface sites was not observed. The oxide coating morphology and composition was

altered as the surface aged, resulting in an iridium-depleted, smoother surface compared to the fresh material. The observed psuedo-first order reaction rate constant for RDX reduction increased by approximately 30% on the aged electrode in a batch reactor experiment. The results suggest that as the rough electrode surface became smoother, reaction sites remained active and became more accessible to the large contaminant molecules. The results of this study demonstrate the effectiveness and durability of Ti/MMO cathodes to reduce mixtures of dissolved explosive compounds. Exploration of new, effective reactive materials expands the scope of remediation technologies available to achieve environmental restoration objectives.

2.1 Introduction

Wastewater streams containing explosive compounds from ordinance manufacturing, handling, and disposal activities significantly contribute to groundwater contamination (Spain et al., 2000). Due to the manner in which explosives are produced and utilized, mixtures of several compounds are often present in the natural systems impacted by these waste streams (e.g., Clausen et al. (2004)). Two of the most widely utilized classes of explosive compounds are heterocyclic nitramines and nitroaromatics. The heterocyclic nitramine octahydro-1,3,5,7-tetranitro-1,3,5,7-tetrazine (HMX) is often produced simultaneously with hexahydro-1,3,5-trinitro-1,3,5-triazine (RDX) as a synthesis by-product (Gibbs and Popolato, 1980). Similarly, dinitrotoluene (DNT) isomers (2,4-DNT and 2,6-DNT) may also be generated in large fractions from 2,4,6-

trinitrotoluene (TNT) production (Spanggord et al., 1991; Nishino et al., 1999). These two classes of compounds exhibit a range of degradation and sorption characteristics in natural systems (Walker and Kaplan, 1992; Gorontzy et al., 1994; Talmage et al., 1999). The complexities of contaminant mixtures present an engineering challenge to the design of remediation strategies for explosives-contaminated groundwater.

Research into the aerobic and anaerobic biodegradation of nitroaromatics and heterocyclic nitramines has been conducted over the past two decades. Aerobic pathways for nitroaromatic biodegradation generally proceed through a mechanism enzymatically catalyzed by either mono- or dioxygenase to form phenolic or catecholic derivatives (Spain, 1995). The aromatic rings are subsequently opened to form organic acids (Spain, 1995). RDX is biodegraded aerobically when utilized as the sole nitrogen source and forms easily metabolized intermediates (Binks et al., 1995; Coleman et al., 1998). Nitro groups are reduced in the anaerobic biological degradation pathways of both nitroaromatics and heterocyclic nitramines. Nitroaromatics are generally transformed to their amine analogs (Spain, 1995). The heterocyclic rings of RDX and HMX are more unstable than the aromatic ring after the initial two electron reduction of the nitro group. Therefore, pathways either incorporate initial ring-cleavage or form nitroso derivatives, which both eventually decompose to small molecular weight nitrogen and carbon containing compounds (McCormick et al., 1981; Hawari et al., 2000; Hawari et al., 2001).

Abiotic degradation mechanisms of aqueous phase explosives have also received attention as possible remediation strategies. Base catalyzed hydrolysis (Heilmann et al.,

1996; Emmrich, 1999) and advanced oxidation processes (Bier et al., 1999; Spanggord et al., 2000; Hawari et al., 2002; Adam et al., 2004; Chen et al., 2005) may be viable approaches for highly concentrated source areas or controlled waste streams. Reduction of explosive compounds on Fe^0 (Agrawal and Tratnyek, 1996; Hundal et al., 1997; Singh et al., 1998, 1999; Bandstra et al., 2005; Monteil-Rivera et al., 2005) or surface bound Fe^{2+} (Klausen et al., 1995; Gregory et al., 2004) has been reported to proceed through pathways similar to those observed under anaerobic microbiological systems. Contaminant reduction by oxidized iron surfaces normally require biological mediators to keep the active Fe^{2+} sites reduced (Borch et al., 2005). Following a pathway similar to biodegradation, TNT and DNT are reduced to the corresponding aminotoluenes. This normally requires coupling reduction techniques with a subsequent oxidation process (Hess et al., 1998; Hwang et al., 2000; Kröger et al., 2004). Recently, the electrochemical mechanisms and reaction kinetics of explosive compounds have been reported for a variety of cathode materials and reactor configurations (Rodgers and Bunce, 2001; Doppalapudi et al., 2002, 2003; Bonin et al., 2004; Palaniswamy et al., 2004). Taking advantage of the inherent reductive and oxidative processes within electrolytic cells, robust remediation technologies may be developed from an electrochemical platform.

Very few studies have been reported that specifically deal with aspects of degrading explosive compound mixtures. Devlin et al. (1998) observed inhibited reaction rates via competition for active sites on Fe^0 using various substituted nitroaromatics. These effects may be exacerbated on aged surfaces, where active site

density may be reduced from blockage or inactivation. No prior electrochemical studies of competition effects of mixed contaminant streams were found. Since mixtures of nitroaromatics and heterocyclic nitramines are normally found in groundwater contaminant plumes, the impact of co-contaminants on technology efficacy is imperative to establish. Our laboratory has developed a novel remediation technology based on in situ electrochemical degradation of dissolved organic contaminants that can be easily deployed in a permeable reactive barrier format (Gilbert and Sale, 2005; Wani et al., 2006; Petersen et al., 2007). All prior work with this technology has utilized a titanium substrate coated with a binary mixture of TiO_2 and IrO_2 (ca. 90/10 Ti/Ir by mol fraction) for both the anode and the cathode. The activity and stability of similar materials under modest hydrogen-evolution conditions has previously been characterized (Kötz and Stucki, 1987; Kodintsev and Trasatti, 1994; Burke and Naser, 2005). However, only a limited number of investigations have utilized metal oxide electrodes as a substrate to reduce organic compounds.

The objective of this work is to evaluate reaction kinetics for the electrochemical reduction of heterocyclic nitramines and nitroaromatic mixtures on fresh and aged Ti/MMO cathodes. In order to gain a clear understanding of reactant competition for active sites on the cathode, the surface reaction mechanism required further elucidation than had been previously postulated. Surface morphology and composition have been cited as a large reason for changes in activity of heterogeneous reaction systems, especially at oxide-water interfaces. Considering how the Ti/MMO surface evolves under controlled conditions provides a foundation for assessing expected changes over

relatively modest implementation lifetimes. More significantly, how the surface evolution affects observed reaction kinetics plays a role in assessing the efficacy of a remediation technology.

2.2 Materials and Methods

2.2.1 Chemicals

Solid phase RDX and HMX were obtained from OSI/HAAP at 90.90% and 100% purity, respectively. Analytical grade TNT and DNT were purchased from AccuStandard, Inc. One hundred milligrams of each was dissolved in 1 L of HPLC grade methanol to create lab stock solutions for reaction kinetic experiments. All electrolyte and pH buffer reagents purchased were ACS grade and used without further purification. Deionized water was used as the solvent in all experiments.

2.2.2 Batch Reactor

Reaction kinetics were measured in a two-chambered electrolytic cell with a 1-L working electrode chamber. The two chambers were separated by a Teflon electrode assembly that contained a Nafion membrane in between the anode and cathode. Each electrode was an 8 cm × 8 cm square section of electrode material (ELGARD 150 Anode Ribbon Mesh, Corrpro Companies, Inc.), with a surface area to bulk area ratio of 2.5. The electrodes were attached to insulated copper wires. A small section of glass tubing was placed around the connection and filled with epoxy to prevent the copper from

oxidizing. Electrical connections were routed through ports in the reactor cap and sealed by Swagelock fittings. The electrodes were polarized by applying a potential between the working and counter electrodes using a GW Laboratory DC Power Supply (model GPS-3030D). The electrochemical potential of the cathode was measured against an Ag/AgCl reference electrode (Dri-Ref, World Precision Instruments Inc.) placed inside the working electrode chamber. The working electrode potential and cell current were monitored using digital multimeters (Fluke model 189). Electrolyte pH and temperature in the cathode chamber was monitored using a Denver Instruments pH/ATX plastic body combination electrode attached to a Denver Instruments AP25 pH/Ion/FET meter. The temperature of the electrolyte was not controlled, but remained between 22 to 25 °C. The reactor contents were stirred at a constant rate using a 1-in Teflon stir bar on a magnetic stir plate.

2.2.3 Kinetics Experiments

Reaction kinetics were measured in the batch reactor at a constant cathode potential relative to the Ag/AgCl reference electrode. All reported potentials are relative to the standard hydrogen half cell potential. Reactants were introduced into the reactor by adding a known quantity of the lab stock solutions for each species to achieve the desired initial concentration to the supporting electrolyte. A 0.1 M sodium acetate buffer served as the supporting electrolyte. The pH of the buffer was adjusted using 5 M acetic acid prior to each experiment. After introducing the reactants, the contents were allowed to mix for several hours. An electrical bias was applied between the electrodes at time =

0 min to set the cathode to the desired electrochemical potential relative to the reference electrode. The bias was manually adjusted to maintain the cathode at the desired potential throughout the experiment. Samples were withdrawn at 20- to 60-minute intervals after initiating the experiment. Approximately 2 mL were withdrawn from the cathode chamber using a 10-ml glass syringe with a hypodermic needle through a Teflon-faced silicon septum attached to the reactor cap. Acetic acid (5 M) was periodically added to the cathode chamber to maintain the desired pH during the experiments.

2.2.4 Electrode Aging

Two 20 cm × 15 cm sections of the mesh electrode were attached to insulated copper wires with glass sleeves epoxied over the connection and placed in a glass tank. The tank was filled with a 0.05 M aqueous solution of $NaClO_4$. A potential difference of 3.5 V was applied between the electrodes using a GW Laboratory DC Power Supply (model GPS-3030D). The tank was covered with aluminum foil and left undisturbed until 1.7×10^5 A hr at 40 A m^{-2} were passed through the cell. The electrodes were then removed from the tank, washed in distilled water, and dried in a vacuum desiccator. Two 8 cm × 8 cm sections were cut and placed in the batch reactor electrode assembly. Small sections were removed for analysis of the surface layer composition and morphology after the extended period of use.

2.2.5 *Electrode Surface Analysis*

Electrode surface composition and morphology were evaluated by scanning electron microscopy (SEM) with energy dispersive x-ray spectrometry (EDS). SEM and EDS were performed with a JOEL JSM-6500F scanning electron microscope equipped with a Thermo Electron EDS system. The incident electron beam acceleration voltage was 15 kV. Samples were cut from fresh and the aged electrode and dried in a vacuum desiccator that was shielded from ambient light. Electrode sections were placed on a sample tray using two-sided tape with the side of the electrode that was exposed to the complementary electrode facing up.

2.2.6 *Sample Analysis*

Aqueous phase concentrations for explosives and their high molecular weight products were determined using an Agilent 1100 HPLC equipped with a UV detector and a Finnigan LCQ-DUO ion-trap mass spectrometer. The HPLC was equipped with a C18 column (26 cm long × 2.1 mm ID; 5 μm particle size). The mobile phase was isocratic at 50:50 methanol:water at a flowrate of 0.25 mL min^{-1}. The UV detector wavelength was set at 254 nm. Sample introduction to the mass spectrometer was through an electrospray interface. Ionization was performed in the negative ion mode. Concentrations were quantified by comparing peak areas from the unknown samples with calibration standards. The calibration standards were created by serially diluting commercial standards obtained from SRI International. The detection limit of the method was

estimated to be 0.16 and 0.13 μM for RDX and HMX, respectively; and 0.05 and 0.03 μM for TNT and 2,4-DNT, respectively.

Formaldehyde concentration was determined by derivatization with 2,4-dinitrophenylhydrazine (DNPH, Aldrich, reagent grade) followed by HPLC/UV (EPA Method 8315a). A 4-mL sample was collected from the batch reactor and transferred to a 10-mL culture tube. Four ml of 5 M acetate buffer was added to the sample and the pH was adjusted to 5 by dropwise addition of dilute HCl or NaOH. Three drops of a 3.0 mg mL^{-1} solution of DNPH in acetonitrile (HPLC grade) were added to the culture tube, which was then placed in a 40 °C sand batch on a rotary shaker table for 1-hr. Samples were then extracted with three volumes of methylene chloride. The methylene chloride solvent was exchanged with HPLC grade acetonitrile in a N_2 concentrator apparatus. The acetonitrile sample matrix was then diluted to a 70% acetonitrile volume fraction with HPLC water. The derivatized HCHO-DNPH complex was quantified on an agilent 1100 HPLC (C18 column; 26 cm long × 2.1 mm ID; 5 μm particle size) with a UV detector set to 360 nm. The mobile phase was a 70/30 (by volume) acetonitrile/water solution flowing isocratically at 0.32 ml min^{-1}. Sample peaks were quantified by comparing unknowns with standards created in the laboratory from a stock formaldehyde solution that was derivatized by the same procedure. The method detection limit was 2.3 μM.

2.3 Results and Discussion

2.3.1 Hypothesized Surface Mechanisms

Competition for active sites on fresh Ti/MMO electrodes were evaluated in terms of two hypothesized surface reaction mechanisms. The first hypothesized mechanism considers pure reactant competition at the electrode surface to form an activated surface complex prior to an electron transfer step. For heterocyclic nitramines and nitroaromatics, reduction mechanisms similar to this have been suggested to occur on metallic iron surfaces (Agrawal and Tratnyek, 1996; Singh et al., 1999; Bandstra et al., 2005; Wanaratna et al., 2006). Reaction kinetics of this mechanistic scenario have been treated using the Langmuir-Hinshelwood-Hougen-Watson (LHHW) rate law. Assuming electron transfer to an adsorbed surface complex (e.g., for RDX) is the rate-limiting step, the rate is

$$R_{RDX} = -\frac{C_{RDX} k_{RDX} K_{RDX}}{1 + K_{RDX} C_{RDX} + \sum_{j \neq RDX} K_j C_j}, \qquad (2\text{–}1)$$

where R_{RDX} is the reaction rate of RDX, C_i is the aqueous concentration of reactant i in the well-mixed solution, and K_i is the Langmuir adsorption constant of i (RDX or other reactant) at the Ti/MMO active site.

The second hypothesized mechanism for heterocyclic nitramine and nitroaromatic degradation at a Ti/MMO cathode is reduction via a mediator species, such as catalytic

hydrogenation. For the catalytic hydrogenation of nitroaromatics, the external nitro groups are reduced by a surface-adsorbed hydrogen atom (Benedetti et al., 1991). A similar mechanism was expected for heterocyclic nitramines. The formation of an active hydrogen atom on Ti/MMO surfaces, available to react with aqueous phase organic molecules, is an extension of the hydrogen evolution reaction on a transition metal oxide surface.

$$M\text{-}OH + H^+ \longrightarrow M\text{-}OH_2^+ \xrightarrow{+e^-} M\text{-}OH_2 \qquad (2\text{–}2a)$$

$$M\text{-}OH_2 \xrightarrow[-OH^-]{+e^-} M\text{-}H \xrightarrow[-H_2]{+H_2O} M\text{-}OH \qquad (2\text{–}2b)$$

At the completion of Reaction 2–2a, the reduced surface hydroxide site serves as an active site for hydrogenation of nitro groups. The resulting reaction kinetics are expected to be first-order with respect to concentration of the organic molecule (assuming no adsorption of the molecule prior to reaction with the adsorbed hydrogen atom) under this mechanistic scenario.

2.3.2 Single-Analyte Experiments

RDX and TNT concentrations were measured in batch degradation experiments starting at two different initial concentrations. The results from both experiments for each analyte were simultaneously fit to Equation 2–1 (Figure 2–1). The rate law parameters k_i and K_i for RDX were 1.9×10^{-3} μmol cm^{-2} min^{-1} and 0.09 μM^{-1},

respectively. The corresponding parameters for TNT were 1.8×10^{-2} μmol cm^{-2} min^{-1} and 0.009 μM^{-1}. The extent of self-inhibition observed in the experimental data and corresponding regression curves was not very large for the order-of-magnitude difference in initial concentrations. From these data, the role of contaminant adsorption/desorption in the overall mechanism was not important under the laboratory reactor conditions.

Analyzing the data using the mediated electron transfer mechanism, the observed first-order rate constants, k_{obs}, calculated from the simultaneous regression of both high and low initial concentration experiments were 0.017±0.002 and 0.025±0.002 min^{-1} for RDX and TNT, respectively. Rate constant uncertainty decreased when the low and high initial concentration experiments were analyzed separately. The concentration dependent reaction rates indicated that self-inhibition, consistent with the first hypothesized mechanism, may be a viable pathway. Differences between high and low initial concentration experiments were significant at a 5% level, but comparing both reaction rates were difficult given the larger scatter and measurement error of the low initial concentration data. Rate inhibition due to inter-species competition was further explored in multi-analyte experiments.

Formaldehyde is the major product of RDX reduction in both biological and electrochemical systems (McCormick et al., 1981; Bonin et al., 2004). The carbon mass balance for RDX was verified in the single-analyte experiments by measuring formaldehyde concentrations. The mass balance over a 3-hr degradation experiment at -1100 mV and neutral pH was approximately 90% (Figure 2–2).

The impact of mass transfer on the observed reaction rates was investigated by repeating the single-analyte tests at three different reactor agitation rates. The change in reaction rate as a function of stir rate, ω, was quantified using k_{obs} as a metric. Observed first-order rate constants increased for TNT and RDX by approximately 5% for the 15% increases in $\omega^{1/2}$ (Figure A–1); however, not to the extent expected for a purely mass-transfer controlled system (approximately 10% to 20%).

2.3.3 Multi-Analyte Experiments

Utilizing the kinetic parameters calculated from the single-analyte experiments, the simultaneous degradation of RDX and TNT was modeled under the LHHW mechanistic assumptions. The initial concentrations of RDX and TNT in the combined experiment were 27 and 45 μM, respectively. The surface area density in the batch reactor was approximately 0.16 cm^2 mL^{-1}, much smaller than the surface area density (1 to 1.65 × 10^4 cm^2 ml^{-1}) used to elucidate competition between chlorinated aliphatic reduction on Fe^0 surfaces (Wüst et al., 1999; Arnold and Roberts, 2000). Comparing the experimental and kinetic model predictions, a relatively large rate inhibition was expected for RDX that was not reflected in the experimental observations (Figure 2–3). Results from the combined degradation experiment did not appear to notably change compared to the single-analyte tests, which have also been included in Figure 2–2 for illustrative purposes at the similar initial concentration.

Experiments utilizing HMX and 2,4-DNT as competing reactants for RDX and TNT, respectively, were subsequently performed. Observed first-order rate constants

from the single and multi-analyte experiments (Table 2–1) did not significantly change for the competing reactants within the same compound class. This suggests that the same active sites were used by all species. The common active site model assumes Reactions 2–2a and 2–2b are frequently turned over, such that adsorbed H atoms are immediately replenished after reaction with the target species. Under this scenario, without a strong adsorption complex required for electron transfer, rate inhibition from co-reactants is not expected based on the rate-law formulation.

A subsequent multi-analyte experiment was performed at unequal initial concentrations in an attempt to verify that the lack of any considerable competition for active sites on the Ti/MMO surface. Starting at initial RDX and TNT concentrations of 1 and 40 μM, respectively, if competition were a significant reaction rate inhibitor the rate of RDX reduction was expected to be significantly decreased based on the single-analyte experiments using the LHHW mechanism assumption. As was the case in the previous combined tests, reaction rate inhibition was not observed in the experimental results (Figure A–2). This supports the conclusion that electron-transfer reactions occur without the organic reactants significantly adsorbing to the active site on the Ti/MMO surface that is utilized by both compound classes.

2.3.4 Electrolyte pH

Under the second hypothesized mechanism, decreasing electrolyte pH was expected to translate to an increased active site concentration, and therefore increased reaction rate. At a constant cathode potential of -1100 mV, the pH was lowered from

approximately 6.5 to 3. The observed reaction rates increased by approximately 25% for TNT and RDX (Figure 2–4). This cathode potential is similar or greater in magnitude than voltammetry peaks reported for both RDX (Bonin et al., 2004) and TNT (Rodgers and Bunce, 2001). At -700 mV, a potential still less negative than the reduction potentials for TNT, but larger than that of RDX, a concentration decline was still observed for each species. This indicated that reactions remained energetically viable at -700 mV. At the more positive cathode potential, the pH rate enhancement decreased and was essentially negligible for TNT.

The reduction of RDX at potentials more positive than the peak potential reported in Bonin et al. (2004) was supported by the transient formation of the nitroso-RDX analogs (hexahydro-1-nitroso-3,5-dinitro-1,3,5-triazine or MNX; hexahydro-1,3-dinitroso-5-nitro-1,3,5-triazine or DNX; hexahydro-1,3,5-trinitroso-1,3,5-triazine or TNX) and eventual accumulation of formadelhyde (Figure 2–5a). The lack of rate inhibition from multiple reactants present in the system, coupled with the observed enhancement in reduction kinetics when the electrolyte pH was decreased, suggests that the electrocatalytic hydrogenation mechanism is the viable reaction pathway on the fresh Ti/MMO surface. The overall reaction kinetics reflect an Eley-Rideal mechanism, which is first-order with respect to the concentration of the organic reactant.

2.3.5 Electrode Surface Evolution

The aging was conducted in a clean laboratory environment to avoid artifacts that may arise in more complex electrolytes (e.g., natural ground water). Analysis of the

cathode and anode aged in the $NaClO_4$ electrolyte indicated that changes in surface composition and morphology occurred during the aging process. The ratio of atomic abundances of O, Ti, and Ir calculated from the EDS spectra were used to evaluate the composition changes between the aged and fresh electrodes (Table 2–2). The spectra were sampled from a broad region on the electrode and at more specific locations to understand how the surface evolution is distributed across the electrode geometry. The electrode regions are defined in Figure 2–6. Only the common elements of the mixed metal oxide coating were compared between the three electrodes. The other elements detected were associated with the $NaClO_4$ supporting electrolyte.

The standard reduction potentials of IrO_2 to Ir(III) and Ir(III) to Ir(0) in acidic conditions are 223 and 1156 mV (relative to the standard hydrogen electrode), respectively (Bard et al., 1985). Therefore, the reduction of iridium was expected to occur at the operating potential in the aging electrolysis cell, and the loss of iridium content from dissolution was expected at the cathode. On the aged cathode the Ir:O ratio decreased and Ti:O ratio increased in the broad sample relative to the fresh electrode. Iridium was ubiquitous on the electrode surface at the highest magnification level (33X) (Figures A–3 - A–5). Atomic abundance ratios at the corner and front face of the electrode mesh reflected the overall trend in iridium depletion and titanium enrichment at the electrode surface.

The fresh TiO_2-IrO_2 coated electrodes exhibited the cracked-mud morphology (Figure 2–6a & d) that was observed in prior studies of transition metal oxide electrode coatings prepared by thermal decomposition of a metal chloride salt over a titanium

substrate (Morimitsu et al., 2000; Wang et al., 2001; Børresen et al., 2002; Da Silva et al., 2004). After the aging process, the cracked-mud features were much less prevalent on the aged anode and cathode. The result was a much smoother surface based on the SEM images (Figures 2–6). Some surface area dense regions remained, mainly in the corner regions of the electrode, but complimentary studies have suggested that the majority of electron-transfer activity occurs at front regions of the electrode (Chapter III). No indication of extensive pitting or cracks were found upon inspection of the electrodes, suggesting that reactions were not confined to microscopic features or imperfections on the surface (Gaspar et al., 2002).

2.3.6 Impact of Aging on Reaction Processes

The changes in electrode morphology and composition are important with respect to modifying the governing electrochemical processes over time. The impact of those changes was evaluated in terms of reaction kinetics, product distribution, and reactant competition leveraging the *a priori* knowledge of their behavior on the fresh electrodes. Using RDX as the probe contaminant in this analysis, a subset of batch reactor experiments were conducted using the aged anode and cathode as the electrode substrate.

The reaction kinetics of RDX reduction in the batch system were measured at -700 mV and two constant pH conditions (3 and 6.5). This cathode potential was chosen to isolate the electrocatalytic hydrogenation pathway and exclude the direct reduction of a nitro group, which may occur at more negative cathode potentials. Additionally, any impact of surface evolution was expected to be emphasized at more positive cathode

potentials. This is based on the hypothesis that less energetic reaction conditions prevent processes (e.g., electron tunneling) that would circumvent insulating features of the altered oxide surface.

The reaction rate enhancement observed when the electrolyte pH was lowered from 6.5 to 3 was lowered was not as large on the aged electrode as on the fresh surface (Figure 2–7). The k_{obs} increased 16% on the aged electrodes compared to 37% on the fresh electrode at -700 mV. However, rate constants were larger on the smoother, aged surface. This unexpected result suggested that the activity of the electrode surface was developed over the timeframe of the laboratory aging process.

Examination of the RDX product distribution and competition effects in the batch reactor supported this conclusion. The transient appearance of mono-, di-, and tri-nitroso RDX analogs (MNX, DNX, and TNX, respectively) was observed using both electrode substrates at -700 mV (Figure 2–5). In all experiments, MNX and DNX concentrations grew to approximately 5% of the initial RDX molar concentration after one hour in the reactor. The concentration of each species then began to decline to a level below the detection limit of the analytical method (ca. 0.15 μM for all nitroso-derivatives). On the fresh electrode, TNX accumulation was observed over the entire 240-min experiment. At the end of the experiment, the TNX accounted for approximately 15% of the initial moles of RDX in the reactor. In the experiment with the aged electrode, TNX accumulated to about 7% of the initial RDX molar concentration, then declined after 120 min. The final concentration of TNX in the aged electrode experiment was 4.5% of the initial RDX concentration, about 1.2 μM.

Using TNT as a secondary reactant, site competition was reevaluated on the aged electrode surface. As was the case when using fresh electrodes, the presence of TNT did not inhibit the RDX reduction rate in the system. This further supported the mediated hydrogenation pathway as the viable degradation mechanism on the Ti/MMO electrode surface.

Overall, higher activities on the aged surface suggest a conceptual model in which active sites on the electrode surface are exposed on the (qualitatively) smoother electrode surface. The active site density on metal oxide surfaces that exhibit the cracked-mud morphology are often reported to increase with time of polarization (Ribeiro and de Andrade, 2004). At short time-scales, this was attributed to an increased wetting of the originally inaccessible active sites within the surface coating cracks. Electrodes were exposed to the electrolyte and reactant for several hours prior to polarization. Therefore, the surface film was expected to be fully saturated for both the fresh and aged electrode experiments. Active sites within the surface coating pore structure may have been unavailable for the relatively large reactant molecules in this system. Similar relationships between reactant molecular size and surface morphology have been reported when characterizing the oxidation efficiency of comparably sized organic molecules over RuO_2 (Zanta et al., 1999; Malpass et al., 2006). As the initially rough surface was smoothed through undetermined mechanisms while aging, the increased electrode activity suggested a larger fraction of total active sites becoming exposed to the bulk solution, resulting in a surface that was overall more active for the target compounds.

2.4 Conclusion

The results of this research illustrate the encouraging aspects of using Ti/MMO electrodes as cathodes in an electrochemical system for the remediation of explosives-contaminated groundwater or waste streams. The electrochemical reduction of heterocyclic nitramines and nitroaromatics was initiated at a Ti/MMO cathode through mediated pathway with adsorbed hydrogen molecules. Consequently, accounting for reaction inhibition during system design may be avoided due to the lack of active site competition between co-contaminants at the concentrations investigated in this study. Additionally, enhanced reaction rates at lower pH conditions through the hypothesized electrocatalytic hydrogenation pathway support an anode-cathode sequence of contaminant exposure in flow-through reactors. This conclusion was validated in flow-through column experiments that tested both the anode-cathode and cathode-anode sequences (Gilbert and Sale, 2005).

The evolution of electrode surface morphology in natural systems is expected to resemble the progression characterized in this study. Site-specific characteristics such as alkalinity and dissolved metals may lead to secondary aging artifacts; however, transition metal oxide electrodes have been shown to be fairly resistant to metal poisoning when cathodically polarized (Kötz and Stucki, 1987). After extended periods of use, iridium depletion and loss of cathodic activity may be a system limitation. Future research should be directed towards understanding the governing processes in long-term electrode

deactivation, especially with regards to reducing organic contaminants. Activities such as these will promote the use and further investigation of transition metal oxide electrodes for novel technologies.

2.5 References

Adam, M.L., Comfort, S.D., Morley, M.C.,Snow, D.D., 2004. Remediating RDX-contaminated ground water with permanganate: laboratory investigations for the Pantex perched aquifer. Journal of Environmental Quality 33, 2165-2173.

Agrawal, A.,Tratnyek, P.G., 1996. Reduction of nitro aromatic compounds by zero-valent iron metal. Environmental Science and Technology 30, 153-160.

Arnold, W.A.,Roberts, A.L., 2000. Pathways ad kinetics of chlorinated ethylene and chlorinated acetylene reaction with Fe(0) particles. Environmental Science and Technology 34, 1794-1805.

Bandstra, J.Z., Miehr, R., Johnson, R.L.,Tratnyek, P.G., 2005. Reduction of 2,4,6-trinitrotoluene by iron metal: Kinetic controls on product distributions in batch experiments. Environmental Science and Technology 39, 230-238.

Bard, A.J., Parsons, R.,Jordan, J., 1985. Standard Potentials in Aqueous Solutions. Marcel Dekkar, New York.

Benedetti, A., Fagherazzi, G., Pinna, F., Rampazzo, G., Selva, M.,Strukul, G., 1991. The influence of a second metal component (Cu, Sn, Fe) on Pd/SiO_2 activity in the hydrogenation of 2,4-dinitrotoluene. Catalysis Letters 10, 215-224.

Bier, E.L., Singh, J., Li, Z., Comfort, S.D.,Shea, P.J., 1999. Remediating hexahydro-1,3,5-trinitro-1,3,5-triazine-contaminated water and soil by Fenton oxidation. Environmental Toxicology and Chemistry 18, 1078-1084.

Binks, P.R., Nicklin, S.,Bruce, N.C., 1995. Degradation of hexahydro-1,3,5-trinitro-1,3,5-triazine (RDX) by *Stenotrophomonas maltophilia* PB1. Applied and Environmental Microbiology 61, 1318-1322.

Bonin, P.M.L., Bejan, D., Schutt, L., Hawari, J.,Bunce, N.J., 2004. Electrochemical reduction of hexahydro-1,3,5-trinitro-1,3,5-triazine in aqueous solutions. Environmental Science and Technology 38, 1595-1599.

Borch, T., Inskeep, W.P., Harwood, J.A.,Gerlach, R., 2005. Impact of ferrihydrite and anthraquinone-2,6-disulfonate on the reductive transformation of 2,4,6-trinitrotoluene by a gram-positive fermenting bacterium. Environmental Science and Technology 39, 7126-7133.

Børresen, B., Hagen, G.,Tunold, R., 2002. Hydrogen evolution on $Ru_xTi_{1-x}O_2$ in 0.5 M H_2SO_4. Electrochimica Acta 47, 1819-1827.

Burke, L.D.,Naser, N.S., 2005. Metastability and electrocatalytic activity of ruthenium dioxide cathodes used in water electrolysis cells. Journal of Applied Electrochemistry 35, 931-938.

Chen, W.-S., Juan, C.-N.,Wei, K.-M., 2005. Mineralization of dinitrotoluenes and trinitrotoluene of spent acid in toluene nitration process by Fenton oxidation. Chemosphere 60, 1072-1079.

Clausen, J., Robb, J., Curry, D.,Korte, N., 2004. A case study of contaminants on military ranges: Camp Edwards, Massachusetts, USA. Environmental Pollution 129, 13-21.

Coleman, N.V., Nelson, D.R.,Duxbury, T., 1998. Aerobic biodegradation of hexahydro-1,3,5-trinitro-1,3,5-triazine (RDX) as a nitrogen source by a *Rhodococcus* sp., strain DN22. Soil Biology and Biochemistry 30, 1159-1167.

Da Silva, L.M., Franco, D.V., De Faria, L.A.,Boodts, J.F.C., 2004. Surface, kinetics, and electrocatalytic properties of Ti/(IrO_2 + Ta_2O_5) electrodes, prepared using controlled cooling rate, for ozone production. Electrochimica Acta 49.

Devlin, J.F., Klausen, J.,Schwarzenbach, R.P., 1998. Kinetics of nitroaromatic reduction on granular iron in recirculating batch experiments. Environmental Science and Technology 32, 1941-1947.

Doppalapudi, R.B., Sorial, G.A.,Maloney, S.W., 2002. Electrochemical reduction of simulated munitions wastewater in a bench-scale batch reactor. Environmental Engineering Science 19, 115-129.

Doppalapudi, R.B., Sorial, G.A.,Maloney, S.W., 2003. Electrochemical reduction of 2,4-dinitrotoluene in a continuous flow laboratory scale reactor. journal of Environmental Engineering 129, 192-201.

Emmrich, M., 1999. Kinetics of the alkaline hydrolysis of 2,4,6-trinitrotoluene in aqueous solution and highly contaminated soils. Environmental Science and Technology 33, 3802-3805.

Gaspar, D.J., Lea, A.S., Engelhard, M.H.,Baer, D.R., 2002. Evidence for localization of reaction upon reduction of carbon tetrachloride by granular iron. Langmuir 18, 7688-7693.

Gibbs, T.R.,Popolato, A., Eds. (**1980**). LASL Explosive Property Data. Berkeley, CA, University of California Press.

Gilbert, D.M.,Sale, T.C., 2005. Sequential electrolytic oxidation and reduction of aqueous phase energetic compounds. Environmental Science and Technology 39, 9270-9277.

Gorontzy, T., Drzyzga, O., Kahl, M.W., Bruns-Nagel, D., Breitung, J., von Loew, E.,Blotevogel, K.H., 1994. Microbial degradation of explosives and related compounds. Critical Reviews in Microbiology 20, 265-284.

Gregory, K.B., Larese-Casanova, P., Parkin, G.F.,Scherer, M.M., 2004. Aiotic transformation of hexahydro-1,3,5-trinitro-1,3,5-triazine by Fe^{II} bound to magnetite. Environmental Science and Technology 38, 1408-1414.

Hawari, J., Halasz, A., Beaudet, S., Paquet, L., Ampleman, G.,Thiboutot, S., 2001. Biotransformation routes of octahydro-1,3,5,7-tetranitro-1,3,5,7-tetrazocine by municipal anaerobic sludge. Environmental Science and Technology 35, 70-75.

Hawari, J., Halasz, A., Groom, C., Deschamps, S., Paquet, L., Beaulieu, C.,Corriveau, A., 2002. Photodegradation of RDX in aqueous solution: a mechanistic probe for biodegradation with *Rhodococcus* sp. Environmental Science and Technology 36, 5117-5123.

Hawari, J., Halasz, A., Sheremata, T., Beaudet, S., Groom, C., Paquet, L., Rhofir, C., Ampleman, G.,Thiboutot, S., 2000. Characterization of metabolites during biodegradation of hexahydro-1,3,5-trinitro-1,3,5-triazine (RDX) with municipal anaerobic sludge. Applied and Environmental Microbiology 66, 2652-2657.

Heilmann, H.M., Wiesmann, U.,Stenstrom, M.K., 1996. Kinetics of the alkaline hydrolysis of high explosives RDX and HMX in aqueous solution and adsorbed to activated carbon. Environmental Science and Technology 30, 1485-1492.

Hess, T.F., Lewis, T.A., Crawford, R.L., Katamneni, S., Wells, J.H.,Watts, R.J., 1998. Combined photocatalytic and fungal treatment for the destruction of 2,4,6-trinitrotoluene (TNT). Water Research 32, 1481-1491.

Hundal, L.S., Singh, J., Bier, E.L., Shea, P.J., Comfort, S.D.,Powers, W.L., 1997. Removal of TNT and RDX from water and soil using iron metal. Environmental Pollution 97, 55-64.

Hwang, H.-M., Slaughter, L.F., Cook, S.M.,Cui, H., 2000. Photochemical and microbial degradation of 2,4,6-trinitrotoluene (TNT) in a freshwater environment. Bulletin of Environmental Contamination and Toxicology 65, 228-235.

Klausen, J., Tröber, S.P., Haderlein, S.B.,Schwarzenbach, R.P., 1995. Reduction of substituted nitrobenzenes by Fe(II) in aqueous mineral suspensions. Environmental Science and Technology 29, 2396-2404.

Kodintsev, I.M.,Trasatti, S., 1994. Electrocatalysis of H_2 evolution on $RuO_2 + IrO_2$ mixed oxide electrodes. Electrochimica Acta 39, 1803-1808.

Kötz, E.R.,Stucki, S., 1987. Ruthenium dioxide as a hydrogen-evolving cathode. Journal of Applied Electrochemistry 17, 1190-1197.

Kröger, M., Schumacher, M.E., Risse, H.,Fels, G., 2004. Biological reduction of TNT as part of a combined biological-chemical procedure for mineralization. Biodegradation 15, 241-248.

Malpass, G.R.P., Neves, R.S.,Motheo, A.J., 2006. A comparative study of commercial and laboratory-made Ti/$Ru_{0.3}Ti_{0.7}O_2$ DSA® electrodes: "In situ" and "ex situ" surface characterisation and organic oxidation activity. Electrochimica Acta 52, 936- 944.

McCormick, N.G., Cornell, J.H.,Kaplan, D.L., 1981. Biodegradation of hexahydro-1,3,5-trinitro-1,3,5-triazine. Applied and Environmental Microbiology 42, 817-823.

Monteil-Rivera, F., Paquet, L., Halasz, A., Montgomery, M.T.,Hawari, J., 2005. Reduction of octahydro-1,3,5,7-tetranitro-1,3,5,7-tetrazocine by zerovalent iron: Product distribution. Environmental Science and Technology 39, 9725-9731.

Morimitsu, M., Otogawa, R.,Matsunaga, M., 2000. Effects of cathodizing on the morphology and composition of IrO_2-Ta_2O_5/Ti anodes. Electrochimica Acta 46, 401-406.

Nishino, S.F., Spain, J.C., Lenke, H.,Knackmuss, H.-J., 1999. Mineralization of 2,4- and 2,6-dinitrotoluene in soil slurries. Environmental Science and Technology 33, 1060-1064.

Palaniswamy, D.K., Sorial, G.A.,Maloney, S.W., 2004. Electrochemical reduction of 2,4,6-trinitrotoluene. Environmental Engineering Science 21, 203-218.

Petersen, M.A., Sale, T.C.,Reardon, K.F., 2007. Electrolytic trichloroethene degradation using mixed metal oxide coated titanium mesh electrodes. Chemosphere, doi:10.1016/j.chemosphere.2006.11.056.

Ribeiro, J.,de Andrade, A.R., 2004. Characterization of RuO_2-Ta_2O_5 coated titanium electrode: Microstructure, morphology, and electrochemical investigation. Journal of the Electrochemical Society 151, D106-D112.

Rodgers, J.D.,Bunce, N.J., 2001. Electrochemical treatment of 2,4,6-trinitrotoluene and related compounds. Environmental Science and Technology 35, 406-410.

Singh, J., Comfort, S.D.,Shea, P.J., 1998. Remediation RDX-contaminated water and soil using zero-valent iron. Journal of Environmental Quality 27, 1240-1245.

Singh, J., Comfort, S.D.,Shea, P.J., 1999. Iron-mediated remediation of RDX-contaminated water and soil under controlled Eh/pH. Environmental Science and Technology 33, 1488-1494.

Spain, J.C., 1995. Biodegradation of nitroaromatic compounds. Annual Review of Microbiology 49, 523-555.

Spain, J.C., Hughes, J.B.,Knackmuss, H.-J., Eds. (**2000**). Biodegradation of Nitroaromatic Compounds and Explosives. Boca Raton, FL, Lewis Publishers.

Spanggord, R.J., Spain, J.C., Nishino, S.F.,Mortelmans, K.E., 1991. Biodegradation of 2,4-dinitrotoluene by a *Pseudomonas* sp. Applied and Environmental Microbiology 57, 3200-3205.

Spanggord, R.J., Yao, C.D.,Mill, T., 2000. Oxidation of aminodinitrotoluenes with ozone: Products and pathways. Environmental Science and Technology 34, 497-504.

Talmage, S.S., Opresko, D.M., Maxwel, C.J., Welsh, C.J.E., Cretella, F.M., Reno, P.H.,Daniel, F.B., 1999. Nitroaromatic munition compounds: Environmental

effects and screening values. Reviews in Environmental Contamination and Toxicology 161, 1-156.

Walker, J.E.,Kaplan, D.L., 1992. Biological degradation of explosives and chemical agents. Biodegradation 3, 369-385.

Wanaratna, P., Christodoulatos, C.,Sidhoum, M., 2006. Kinetics of RDX degradation by zero-valent iron (ZVI). Journal of Hazardous Materials 136, 68-74.

Wang, T.Y., Xu, L.K.,Chen, G.Z., 2001. Electrochemical properties and microstructure of Ir-Ta-Ti metal oxide coated titanium anodes. Acta Metallurgica Sinica 14, 457-462.

Wani, A.H., O'Neal, B.R., Gilbert, D.M., Gent, D.B.,Davis, J.L., 2006. Electrolytic transformation of ordinance related compounds (ORCs) in groundwater: Laboratory mass balance studies. Chemosphere 62, 689-698.

Wüst, W.F., Köber, R., Schlicker, O.,Dahmke, A., 1999. Combined zero- and first-order kinetic model of the degradation of TCE and *cis*-DCE with commercial iron. Environmental Science and Technology 33, 4304-4309.

Zanta, C.L.P.S., de Andrade, A.R.,Boodts, J.F.C., 1999. Solvent and support electrolyte effects on the catalytic activity of Ti/RuO_2 and Ti/IrO_2 electrodes: Oxidation of isosafrole as a probe model. Electrochimica Acta 44, 3333-3340.

Tables

Table 2–1 Psuedo-first order rate constants calculated from the single and multi-analyte batch experiments at -1100 mV and pH 6.5. The reported range is ± one standard error from the least squares fit of the concentration vs. time data.

reactant		primary	secondary
primary	secondary	k_{obs} (min^{-1})	k_{obs} (min^{-1})
RDX	-	0.02302 ± 0.0002	
	TNT	0.031 ± 0.003	0.032 ± 0.004
	HMX	0.024 ± 0.002	0.020 ± 0.001
TNT	-	0.023 ± 0.001	
	RDX	0.032 ± 0.004	0.031 ± 0.003
	2,4-DNT	0.027 ± 0.003	0.026 ± 0.003

Table 2–2 Ratios of atomic abundance calculated from EDS spectra of a fresh, aged anode (+), and aged cathode (-). The front face and mesh corner regions of the electrode surface are defined in Figure 5. The reported range is ± one standard deviation from an average of 15 to 30 spatially discrete EDS surveys captured from the sample.

	wide area			front face			mesh corner		
	fresh	aged (+)	aged (-)	fresh	aged (+)	aged (-)	fresh	aged (+)	aged (-)
Ti:O	0.69 ± 0.30	0.48 ± 0.04	0.56 ± 0.26	0.33 ± 0.06	1.08 ± 0.10	0.94 ± 0.15	0.65 ± 0.14	0.28 ± 0.05	0.32 ± 0.02
Ir:O	010 ± 0.04	0.09 ± 0.04	0.05 ± 0.02	0.08 ± 0.01	0.12 ± 0.04	0.06 ± 0.02	0.19 ± 0.09	0.06 ± 0.04	0.05 ± 0.01
Ir:Ti	0.15 ± 0.08	0.20 ± 0.08	0.09 ± 0.03	0.24 ± 0.07	0.11 ± 0.03	0.06 ± 0.02	0.31 ± 0.17	0.21 ± 0.15	0.14 ± 0.04

Figures

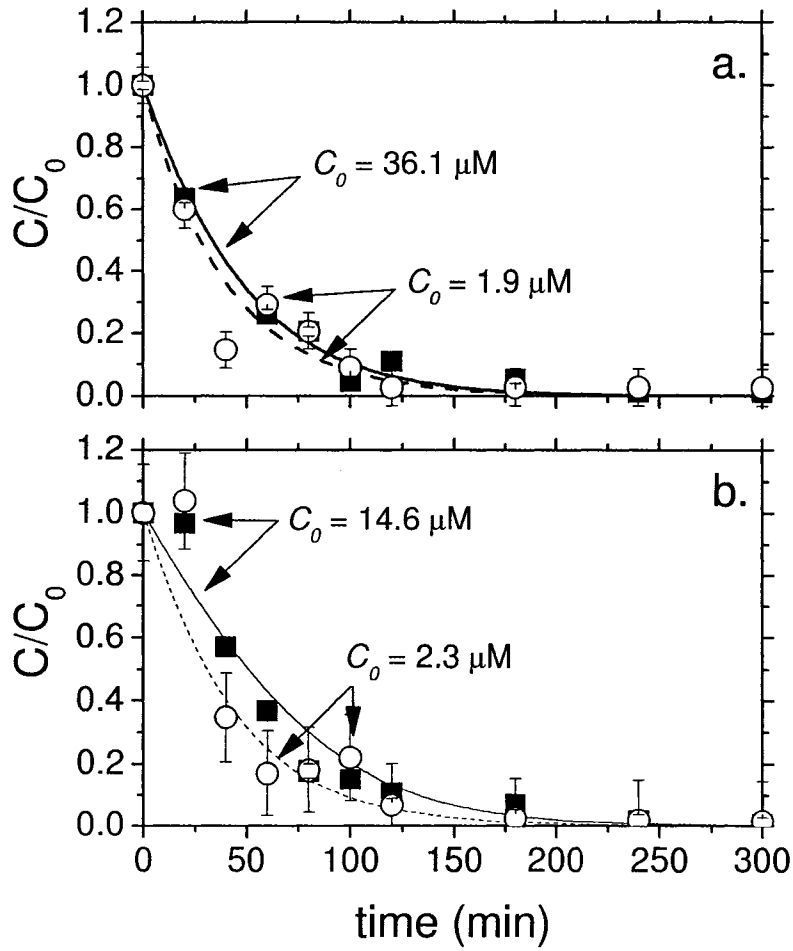

Figure 2–1 TNT (a) and RDX (b) normalized concentrations at a high C_o (TNT: 36.1 μM; RDX: 14.6 μM – closed boxes) and low C_0 (TNT: 1.9 μM; RDX: 2.3 μM – open circles) in the cathode chamber at -1100 mV and pH = 6.5. The LHHW rate law parameters were calculated from fitting the high (solid line) and low (dashed line) C_0 data simultaneously. Error bars represent ± one standard deviation based on the analytical method calibration curve.

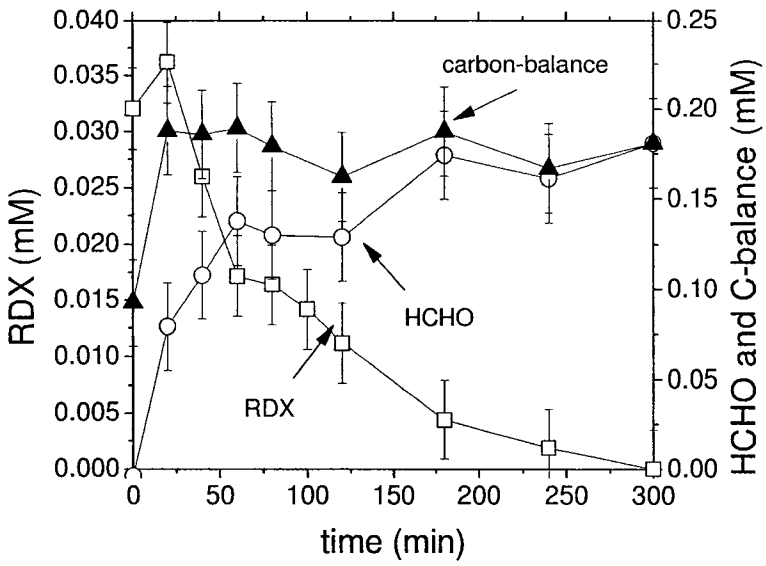

Figure 2–2 RDX degradation and formaldehyde formation in a batch electrochemical reactor. The cathode potential was -1200 mV and the electrolyte pH was 7. Symbols are connected for presentation purposes.

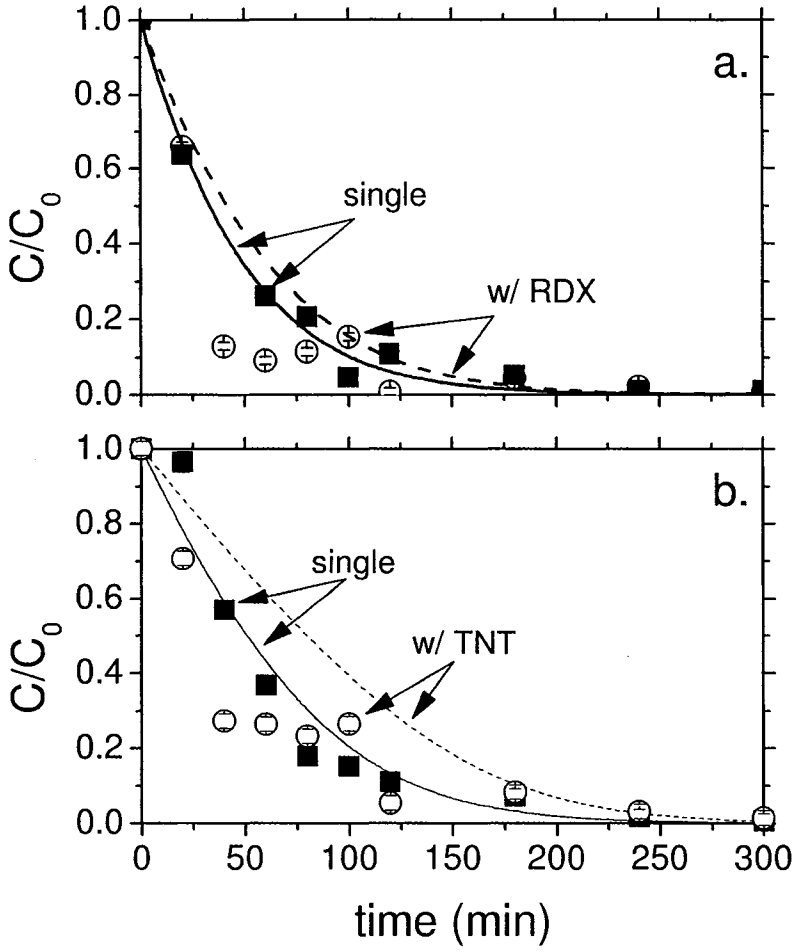

Figure 2–3 TNT (a) and RDX (b) normalized concentrations in separate (closed boxes) and combined (open circles) batch cathodic degradation experiments at -1100 mV and pH = 6.5. Normalized concentrations were predicted for the separate (solid line) and combined (dashed line) experiments using the rate law parameters calculated from the analysis presented in Figure 1.

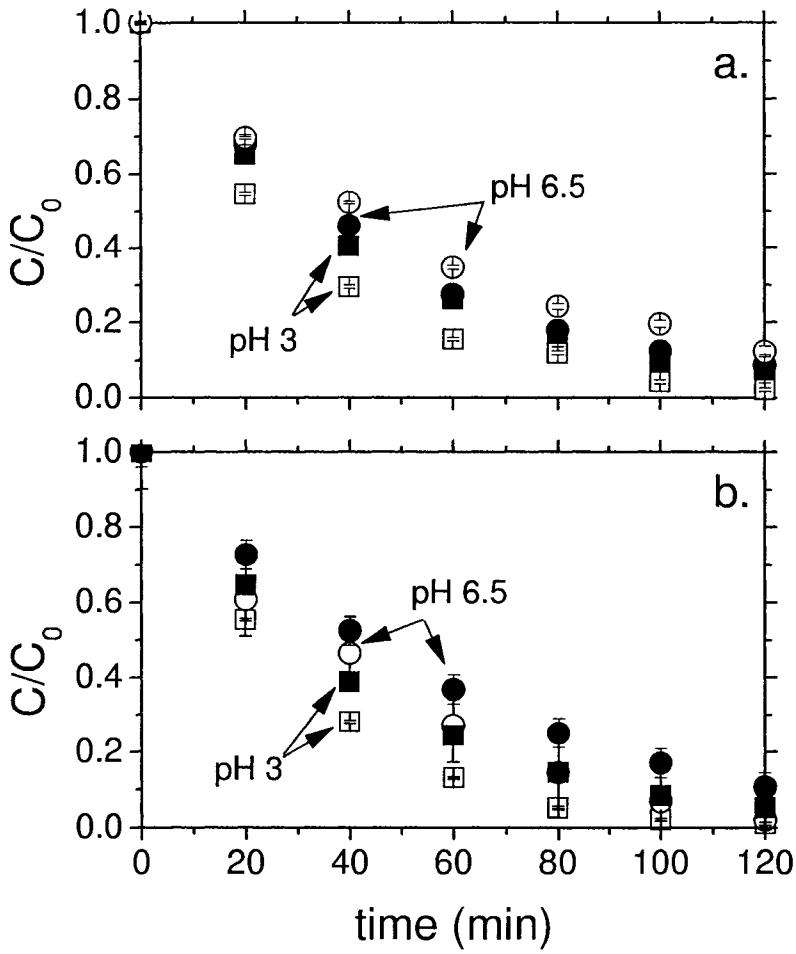

Figure 2–4 TNT (a) and RDX (b) normalized concentrations over time in batch degradation experiments at pH 6.5 (circles) and 3 (boxes) at cathode potentials of -1100 mV (open symbols) and -700 mV (closed symbols). Error bars represent ± one standard deviation based on the analytical method calibration curve.

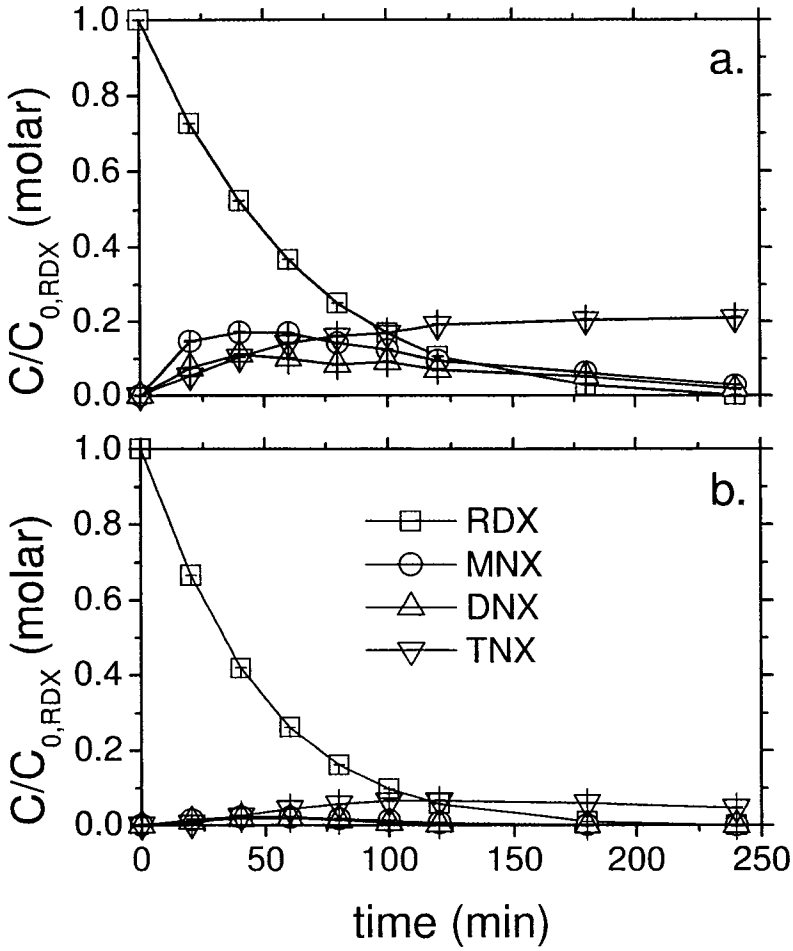

Figure 2–5 RDX and the nitroso-analog reduction by-products measured in the batch electrochemical reactor at -700 mV and pH 6.5 using the fresh (a) and aged (b) cathodes. Symbols are connected for presentation purposes. Error bars represent ± one standard deviation based on the analytical method calibration curve.

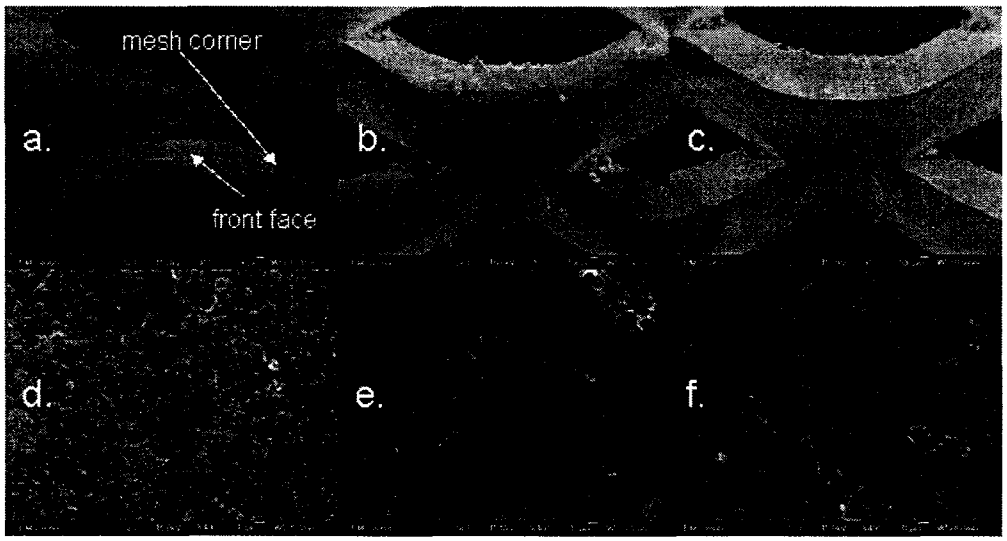

Figure 2–6 SEM images at distance of the fresh (a), aged anode (b), and aged cathode (c). Close up images in the front face region of the fresh (d), aged anode (e), and aged cathode (e).

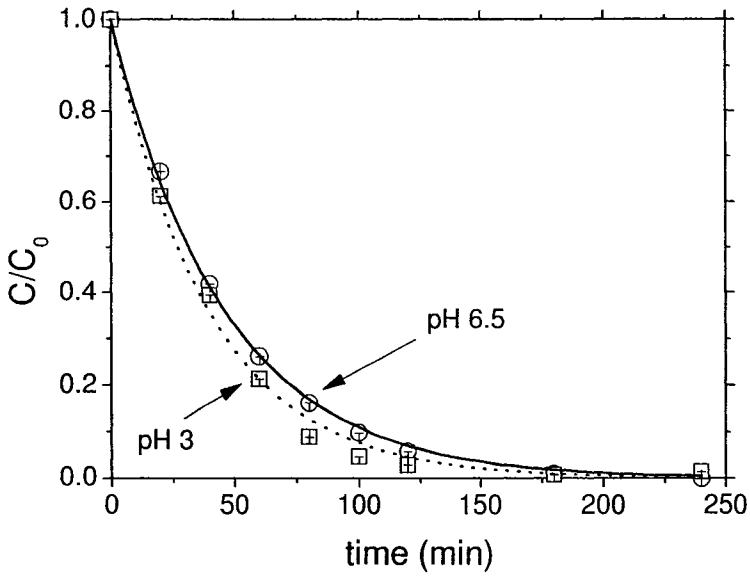

Figure 2–7 RDX reduction using the aged electrodes at -700 mV and pH 6.5 (circles) and 3 (squares). The concentration reduction was fit to a first-order rate law (solid line - pH 6.5; dashed line – pH 3) to determine the pseudo-first order rate constants. Error bars represent ± one standard deviation based on the analytical method calibration curve.

CHAPTER III:

THE INFLUENCE OF MESH GEOMETRY ON THE DISTRIBUTION OF REACTION RATES OVER A THREE-DIMENSIONAL ELECTRODE SURFACE

Abstract

Permeable reactive barriers have become a popular format to deploy in situ groundwater remediation technologies to control contaminant flux in an aquifer. A novel approach that we have explored utilizes electrodes as the reactive substrate in the system, resulting in the degradation of contaminants to environmentally benign compounds. The localized reaction conditions at the electrode surface directly impact the process sustainability and effectiveness by concentrating activity to particular regions of the surface. Although the distribution of these conditions may be important to system performance, experimental assays cannot provide sufficient resolution to ascertain their spatial distribution. Taking advantage of the long-range order of the electrode mesh geometry, we used a 3-D computational fluid dynamics model to characterize the current density distribution and transport environment near the cathode surface. Focusing on a single electrode of the cell, the results illustrated key regions of the surface where sharp gradients in the local reaction and transport conditions formed. Strategies to alleviate

these gradients by modifying the geometry were evaluated. These modifications deemphasized regions within the mesh aperture channels, which resulted in overall larger mass flux reduction rates. This research impacts our interpretation of system performance and is part of an ongoing effort to develop electrochemical-based remediation technologies.

3.1 Introduction

Designing technologies to manage recalcitrant chemical compounds released to groundwater aquifers from anthropogenic sources is a major engineering challenge. Approaches to mitigate those releases require that technologies are both economically and technologically sustainable for extended periods of time. In situ permeable reactive barriers (PRBs) have been a popular choice to control the migration of groundwater contaminants due to their economic and performance advantage over most currentapplications (e.g., pump and treat (Voudrias, 2001)). PRBs based on an electrochemical platform may be more effective than traditionally used reactive materials (both biotic and abiotic) for select situations. Performance efficacy and sustainability in these systems would largely be a function of the electrode physical and activity characteristics.

Recently, research into the use of permeable electrodes in a subsurface flow-through reactor has gained attention (Gilbert and Sale, 2005; Wani et al., 2006; Petersen et al., In Press). These systems have shown promise in their ability to degrade aqueous

phase chlorinated ethenes, heterocyclic nitramines, and nitroaromatics. The electrode material (both anode and cathode) used in these studies has been a dimensionally stable expanded titanium mesh, coated with titanium and iridium oxides. The expanded mesh electrode geometry is conducive for field applications for several reasons. Foremost, the mesh has approximately 50% void space that forms a highly permeable material in the direction of flow. Second, current is easily distributed to the entire electrode sheet, as opposed to the case of a granular electrode. Although these characteristics are favorable, questions still remain regarding the long-term efficacy and optimization of this material. Central to this is the current density distribution on the mesh-size length scale, and how that may impact system sustainability and performance.

Localization of the current density on specific regions of the surface may correlate to faster electrode aging in those regions. Since the activity of this electrode material is directly attributable to a thin (on the order of 1 to 10 μm) layer, spatially localized surface aging is a large concern. Electrode geometry is a major factor in determining how the reaction conditions (i.e., current density) are distributed over the mesh surface. Given that it is infeasible to elucidate the conditions experimentally on a small length scale, a computational approach was required.

Numerical models of the primary (uniform electrode potential) and/or secondary (uniform surface concentration) current density distribution over an electrode surface have been presented for simple parallel plate electrochemical cells (White et al., 1983; Nguyen et al., 1986; Smeltzer and Fedkiw, 1991; Coleman et al., 1995; Steffen and Rousar, 1995; Georgiadou, 1997, 2003). More complicated electrode geometries such as

parallel wires (Šimek and Roušar, 1988), louvered (Martens and Hertwig, 1995), and the porous electrodes of solid-oxide or polymer-electrolyte membrane fuel cells have been studied by computational methods. Using this approach, correlations between the detailed cell geometry and system performance can be understood from a qualitative or quantitative perspective. The expanded mesh electrodes have been used in the anodic production of O_2 and Cl_2 (Wendt and Kreysa, 1999), and as impressed current anodes for cathodic protection applications (Bennet et al., 1998). In those settings, the characteristic length of the reactive/transport system is generally on the scale of the electrode sheet dimensions based on literature characterizing the current density distribution of those systems (Wendt and Kreysa, 1999). The characteristic length scale of a groundwater system is typically much smaller than an industrial process since molecular diffusion is normally the governing transport process. Therefore, the current density distribution in an electrolytic PRB on the scale of the mesh size may be significant to the overall system performance (short and long-term).

The objective of the present research was to elucidate the distribution of reaction conditions over a mesh electrode surface. This was accomplished using a 3-D computational fluid dynamics (CFD) model. The distribution of reaction and transport conditions for a dissolved species in an aqueous supporting electrolyte around the complex surface was evaluated over a range of flowrates and electrode potentials. Electrode potentials were input into the model as surface reaction rate constants following a standard charge-transfer kinetic model (Newman and Thomas-Alyea, 2004).

Extending this analysis, new electrode geometries that emphasized features which may optimize the system performance were assessed.

3.2 Model description

3.2.1 Geometry

The baseline geometry used in the computational experiments was based on an expanded mesh electrode that we have used in previous studies (Gilbert and Sale, 2005; Wani et al., 2006; Petersen et al., In Press). The expanded mesh (Figure 3–1) dimensions are listed in Table 1 using geometric descriptors defined in Figure 3–1.

Two perturbations from the baseline geometry were used to investigate the effect of mesh dimensions on the current density distribution. The first alternate geometry (flat) enlarges the surface area projection in the plane normal to the direction of flow. The second alternate geometry (sharp) minimizes this same surface area projection. In the second alternative, the surface area parallel to flow within the mesh aperture is maximized. Dimensions for these geometries are listed in Table 3–1. The dimension of the mesh aperture was the same for all geometries to focus on the impact of modifying the geometry and exclude effects from an increased surface area density within the solution domain.

The 2 cm × 0.25 cm × 0.22 cm (x, y, z) solution domain used in the computational experiments was discretized using an unstructured tetrahedral mesh (Figure 3–2). The volume of the solution domain was reduced utilizing planes of symmetry and periodicity

where illustrated in Figure 3–2. Two different discretization node spacings were implemented, 0.2 mm (fine) and 0.4 mm (coarse). The differences between the coarse and fine discretized volumes were used to estimate the error imposed by the numerical approximation.

The model chemical system, described in the following section, was selected so that only reduction reactions would be considered. As a result, only the cathode was present in the solution domain. Assumptions appropriate for a dilute reactant in a concentrated unreactive supporting electrolyte allowed the requirement of a full cell within the model to be relaxed.

3.2.2 Transport Model

The flux of an infinitely dilute contaminant species, $\mathbf{N}_i$, in the aqueous phase through the system was defined as the Nernst-Planck flux (Newman and Thomas-Alyea, 2004)

$$\mathbf{N}_i = -D_i \nabla c_i - z_i u_i F c_i \nabla \psi + \mathbf{v} c_i \ , \qquad (3\text{–}1)$$

where D_i is the effective diffusion coefficient of species i within the mixture, c_i is the molar concentration of i in the aqueous phase, z_i is the charge of species i, u_i is the mobility of species i, F is Faraday's constant, ψ is the electrochemical potential, and $\mathbf{v}$ is the velocity vector. The ionic migration term in Equation 3–1 was disregarded given that the concentrations of most organic contaminants are very small (less than 100 μM for

chlorinated ethenes) in aqueous environments with normally large specific conductivities (e.g., 1 mS cm^{-1} (Snoeyink and Jenkins, 1980)), and the target organic species are uncharged ($z_i = 0$).

Utilizing Equation 3–1, the individual steady-state species conservation equation was

$$\frac{\partial c_i}{\partial t} = -\nabla \cdot \mathbf{N}_i + R_i \,, \tag{3–2}$$

where t is time and R_i is the homogeneous reaction rate of species i within the electrolyte. No homogeneous reactions were assumed take place in the aqueous phase, therefore the term was disregarded. Fluid velocities and were calculated using the Navier-Stokes equation. Body forces due to gravity or electromagnetic fields were not taken into account. The overall mass balance was implemented by the continuity equation for an incompressible fluid.

$$\nabla \cdot \mathbf{v} = 0 \tag{3–3}$$

3.2.3 Chemistry Model

The chemical system used in the computational model was previously studied in our laboratory. Hexahydro-1,3,5-trinitro-1,3,5-triazine (RDX) reduction in continuous-flow column reactors using Ti/MMO electrodes was evaluated to determine the viability

of the remediation system (Gilbert and Sale, 2005). RDX reaction rate and current density may be used interchangeably via Faraday's law

$$j_{RDX} = n_{et} F c_{RDX,s} k_{et} \ , \tag{3–4}$$

where j_{RDX} is the current density attributable to electron transfer to RDX, n_{et} is the number of electrons transferred in the reaction, $c_{RDX,s}$ is the reactant concentration at the electrode surface, and k_{et} is the forward reaction rate constant in the electron transfer reaction. Utilizing data from complimentary batch reactor experiments (Gilbert and Sale, 2006), RDX reduction rates were characterized in terms of the Butler-Volmer charge transfer model (Newman and Thomas-Alyea, 2004)

$$j_{RDX} = j_{RDX,0}\left[e^{-\alpha \frac{n_{et}F}{RT}(\psi - E^0)} - e^{(1-\alpha)\frac{n_{et}F}{RT}(\psi - E^0)} \right], \tag{3–5}$$

where $j_{RDX,0}$ is the exchange current density for RDX, α is the transfer coefficient, R is the universal gas constant, T is the absolute temperature, ψ is the electrode potential at the electrode surface, and E^0 is the standard reduction potential for the particular reaction. A surface reaction rate constant as a function of surface potential was derived (Appendix B.1) from the irreversible approximation to Equation 3–5 (Farrell et al., 2000)

$$k_{et} = k_0 \exp\left(-\alpha \frac{n_{et} F}{RT}\left(\psi - E^0\right)\right), \qquad (3\text{–}6)$$

where k_0 is the intrinsic rate constant, which incorporates the activation energy of the electron transfer reaction at the standard reduction potential, E^0 (Appendix B.1).

The parameters of the reaction kinetic model (Equation 3–6) were determined by non-linear regression of k_f versus ψ data set at $n_{et} = 2$ for the overall two-electron reduction of RDX to a nitroso analog. Although subsequent reduction of intermediates at the electrode surface occurs, current density attributable only to RDX reduction was incorporated into the model to emphasize the influence of mesh geometry. At 25 °C, k_0 and α were equal to 7×10^{-7} cm min^{-1} and 0.1, respectively (Appendix B.2). These parameters were used to calculate surface reaction rate constants as a function of ψ in the CFD model. CFD model results are presented with respect to both ψ and k_f.

3.2.4 Boundary Conditions

A constant normal velocity and species concentration was used as the inlet boundary condition. Species diffusion at the inlet was incorporated into the boundary conditions. The gradients for scalar and vector quantities normal to the outlet boundary was set to zero

$$\frac{\partial \mathbf{v}}{\partial n} = 0, \qquad (3\text{–}7a)$$

$$\frac{\partial c_i}{\partial n} = 0 \ , \qquad (3\text{–}7b)$$

where n is the direction normal to the boundary. Equations 3–7a and 3–7b was also used as the boundary conditions for both scalar and vector quantities at the symmetry boundaries.

At periodic boundaries, values for both scalar and vector quantities were translated to the mirrored periodic boundary

$$c_i(0) = c_i(L) \ , \qquad (3\text{–}8a)$$

$$\mathbf{v}(0) = \mathbf{v}(L) \ , \qquad (3\text{–}8b)$$

where L is the location of the mirrored surface. Commensurate with velocities being translated, the pressure gradient across the periodic boundaries was set to zero.

$$P(0) - P(L) = 0 \qquad (3\text{–}9)$$

The species concentration gradients normal to the electrode surface were zero for non-reactive species at the electrode surfaces (Equation 3–7b). The non-slip boundary conditions were also employed at the electrode surface. For reactive species, the irreversible form of Equation 3–6 was used to define the boundary condition at the electrode surface

$$N_{i,\perp} = \frac{s_i A}{nF} j_i \ , \qquad (3\text{–}10)$$

where $N_{i,\perp}$ is the normal flux of species i at the surface , s_i is the stoichiometric coefficient of species i in the reaction of interest, and A is the surface area. A uniform surface potential, ψ, was utilized to calculate the primary current density distribution. This resulted in a single reaction rate constant being defined for a given cathode potential.

3.2.5 Numerical Solution

The model was solved numerically by a finite volume method in the CFD software package Fluent version 6.2.16 (Ansys, Inc., Canonsburg, PA). The momentum, species, and energy equations were discretized using a first-order upwind scheme. Pressure and velocity were coupled by the SIMPLE method (Fluent, 2005). Iterations were calculated using the segregated-implicit solver. Solution convergence was achieved after the normalized residuals for continuity, velocity, and species concentration decreased by three orders of magnitude.

3.2.6 Simulation Conditions

A set of two system variables were examined in the computational experiments, influent velocity and potential (i.e., surface reaction rate constant). Influent velocities from 8.5×10^{-8} to 8.5×10^{-6} m s^{-1} were used as the uniform velocity inlet boundary

condition. Assuming an aquifer effective porosity of 0.3, these values correspond to groundwater volumetric fluxes of 2.5 cm d^{-1} to 250 cm d^{-1} into the electrode assembly. Cathode potentials were evaluated from -0.1 V to -1.4 V, which changed the surface reaction rate constant, $k_{surf,i}$, by 5 orders of magnitude. The influent contaminant concentration was set at 5 μM.

At the more negative limit of this potential range, the reduction of water to H_2 may occur in laboratory experiments depending on the value of the standard reduction potential for the species of interest. The onset of liquid phase convection from H_2 bubbles detaching and rising impacts the system on a length scale larger than that considered in this model. The bubble formation process was not accounted for in the model and was left as a future layer to implement.

3.3 Results

3.3.1 Baseline Geometry

The primary current density distribution over the cathode surface was calculated at the median influent velocity of 8.5×10^{-7} m s^{-1} and potential of -0.86 V ($k_{surf} = 0.016$ cm min^{-1}). Current density distributions on the upstream and downstream electrode faces are presented in Figure 3--3. The maximum current density was realized on the regions of the electrode surface furthest upstream in the domain, where the highest concentrations of the target species exist. On the downstream face, the minimum current densities were calculated that were almost half of the maximum values. Normal diffusion flux, $N_{i,\perp}$, for

the contaminant at the upstream and downstream electrode faces (Figure 3–4) is much more evenly distributed relative to current density. Areas of larger diffusion flux coinciding with large concentration gradients were predicted in the less accessible region of the mesh geometry.

The ratio of current and diffusion rates at the electrode surface (Da_{mod}) was calculated to identify regions that are reactant starved under the uniform electrode potential assumption.

$$Da_{mod} = \frac{j_{RDX} A n_{et} F}{N_{RDX}|_{\perp}} \qquad (3\text{–}11)$$

The result is a number of arbitrary dimensions similar in interpretation to the Damkohler number (Figure 3–5). Similar to Figure 3–4, regions of low Da_{mod} are predicted in the least accessible areas of the mesh geometry located in the highly concave corners of the mesh aperture. The remainder of the electrode surface exhibited a uniform Da_{mod} profile.

Velocity magnitude and contaminant concentration were compared between the coarse and fine discretizations at seventeen locations near the electrode surface. The velocity magnitude relative percent difference (RPD) between the two discretization sizes was 5.7(±3.1) percent over the entire range of simulation conditions. Contaminant concentration RPD was 0.7(±0.4) percent. Based on the relatively small RPD of the two variables, the coarser domain discretization and solver algorithm were considered acceptable for this study.

3.3.2 *Alternative Geometries*

The distribution of current density and diffusion flux at the electrode surfaces was also calculated for the two alternative geometries (Figures B–1 to B–6). In general, as the fraction of accessible electrode surface area increased (sharp → baseline → flat), the distributions for current density shifted towards higher values (Figure 3–6). Current density was focused at the leading edges of the sharp geometry, inducing transport from multiple dimensions similar to radial diffusion to a single point within a domain. This phenomena, coupled with fast reactant depletion in the less accessible regions lead to the larger fraction of surface exhibiting depressed current densities. Correspondingly, since large reactant regions were not formed at the flat electrode surface, RDX diffusion flux was more uniform at that geometry compared to the simulations using the sharp and baseline configurations.

3.3.3 *Global System Behavior*

The conversion of RDX to its reduction products were calculated from the inlet and outlet boundaries of the modeling domain for each geometry as a function of liquid flowrate and potential (Figure 3–7a-c). To remove any bias associated with the total amount of surface area in the solution domain, the rate of RDX mass flux reduction was normalized to the total electrode surface area (Figure 3–7d-f). Both conversion and mass flux reduction rate leveled off as potential decreased and limitations due to mass transport become the rate-controlling mechanism.

Surface area normalized mass flux reduction rates of the alternative electrodes were plotted relative to the baseline geometry at the same conditions (Figure 3–8) to quantify the impact of geometry modification. The normalized rates with the flattened geometry were generally greater than those of the baseline geometry. In the same way, simulations with the sharp geometry, which exhibited the most nonuniform Da_{mod} distribution, predicted normalized mass flux reduction rates smaller those using the baseline geometry. The differences predicted were more than 25% in cases at high velocities and increasingly negative potentials.

3.4 Discussion

3.4.1 Comparison with experiments

Model predictions were compared to results from flow-through column experiments operated at a single flowrate (0.5 ml min^{-1}) and two different cathode potentials (-0.83 and -1.05 V) (Gilbert and Sale, 2005). Gas evolution in the experiments was minimal at these conditions, making them an appropriate validation set for the CFD model. RDX conversion through the experimental column was 0.75 and 0.99 at cathode potentials of -0.83 V and -1.05 V, respectively. Model predictions of 0.75 and 0.95 for the corresponding operating conditions were sufficient to justify using the CFD model to explore system performance at conditions which deviate from validation point.

Conditions that vary on the length scale of Figure 3–5 could not be empirically determined in this system. To validate the simulation results at a qualitative level,

scanning electron micrograph images of mesh electrodes aged in a sodium perchlorate electrolyte were examined for surface morphology changes indicative of charge transfer processes occurring (Figure B–7). The original cracked-mud morphology of the electrode surface became smoother in the same areas that have the highest predicted current density on the baseline geometry. The less accessible regions of the electrode surface retained the "cracked-mud" morphology of the original surface film, suggesting that these areas did not exhibit a large current density. This coincides with the CFD model predictions illustrated in Figure 3–5, and validates the underlying primary current density assumption.

3.4.2 Geometry influence on surface conditions

Mesh geometry impacted the current density and diffusion flux distribution in several manners. Sharpening the electrode geometry (flat → baseline → sharp) exposed a smaller fraction of the electrode surface to the high concentration upstream conditions relative to the baseline or sharp geometries. As a result, the depletion of the target contaminant concentration was directed towards the corner regions, and the current density distributions widened, indicating a higher variability in surface conditions (Figure 3–6).

Species depletion was greater near the corners due to the large surface area density in those regions. Concentration gradients not normal to the electrode surface form and direct reactants towards the depleted regions. This can limit the transport of reactants to the electrode surface at locations proximal to the corners, especially at

increasingly negative potentials (large surface reaction rates). As a consequence of the conditions near the mesh corners, the fraction of the total surface area exhibiting the highest reaction rates increased as the geometry flattened. For example, the fraction of electrode surface with a current density greater than 0.4 A m^{-2} increased from 0.004 to 0.013 to 0.091 for the sharp, baseline, and flat geometries, respectively (Figure 3–6).

Other transport mechanisms of the system interact with the mesh geometry. Hydrodynamics around the mesh were in the creeping flow regime (Reynolds Number $\approx 10^{-3}$ at the aperture geometric center using the aperture hydraulic radius for the characteristic length). Under these conditions, stagnant regions were not predicted to form near the front or back face of the mesh. The lack of stagnant zones near the electrode allowed fluid near the electrode to constantly be refreshed with higher concentration fluid from upstream in the domain, and support the large extent of high reaction rates on the electrode front and back faces.

These processes that controlled microscopic current density distribution were manifested macroscopically in terms of a larger mass-flux reduction rate at the flat geometry compared to the baseline and sharp geometries. As the electrode dimension in the direction of flow increased beyond that of the sharp geometry, mass flux into the mesh aperture walls would likely dominate overall transport to the electrode surface. This situation would be similar in form to the Graetz problem for mass transfer (Newman and Thomas-Alyea, 2004). Under this scenario the primary current density assumption would need to be re-evaluated since a tubular cathode may present significant shielding from the anode that leads to a nonuniform electrode potential distribution.

3.5 Conclusion

CFD techniques have been applied to a flow-through mesh electrode system to elucidate distributions in reaction and transport processes on the length scale of the mesh aperture. Based on a primary current density assumption, the uniformity of the transport/reaction process distribution over the electrode surface was dependent on the electrode geometry. The distributions were most sensitive to the fraction of surface area located in more inaccessible regions of the geometry, principally in the tight corners of the mesh aperture. By flattening the electrode surface on the surface that faces the counter electrode, the primary current density distribution was predicted to be more uniform. Overall, this resulted in higher predicted mass-flux reduction rates through the domain.

This work is based on an idealized conceptualization of the physical and chemical system. Building on this foundation, additional transport and reaction processes (e.g., mechanisms occurring over larger length scales) may be incorporated into the overall model architecture where appropriate. Regardless of the simplicity at this phase, these results provide a direction for assessing process optimization and identifying physical locations on the mesh that could limit the long-term effectiveness of field implementations.

3.6 References

Bennet, J.E., Pohto, G.R.,Mitchell, T.A., 1998. Cathodic protection system for a steel-reinforced concrete structure. Patent. US. 5759361

Coleman, D.H., White, R.E.,Hobbs, D.T., 1995. A Parallel-Plate Electrochemical Reactor Model for the Destruction of Nitrate and Nitrite in Alkaline Waste Solutions. Journal of the Electrochemical Society 142, 1152-1161.

Farrell, J., Melitas, N., Kason, M.,Li, T., 2000. Electrochemical and column investigation of iron-mediated reductive dechlorination of trichloroethylene and perchloroethylene. Environmental Science and Technology 34, 2549-2556.

Fluent, 2005. Fluent 6.2 User's Guide. Fluent Inc.

Georgiadou, M., 1997. Finite-Difference Simulation of Multi-Ion Electrochemical Systems Governed by Diffusion, Migration, and Convection. Journal of the Electrochemical Society 144, 2732-2739.

Georgiadou, M., 2003. Modeling Current Density Distribution in Electrochemical Systems. Electrochimica Acta 48.

Gilbert, D.,Sale, T., 2006. Final report: Sequential electrolytic degradation of energetic compounds in groundwater. SERDP Project Number CU-1234.

Gilbert, D.M.,Sale, T.C., 2005. Sequential Electrolytic Oxidation and Reduction of Aqueous Phase Energetic Compounds. Environmental Science and Technology 39, 9270-9277.

Martens, L.,Hertwig, K., 1995. Modelling of Current and Potential Distributionos in Louvered and Extended Metal Electrodes. Electrochimica Acta 40, 387-391.

Newman, J.,Thomas-Alyea, K.E., 2004. Electrochemical Systems. John Wiley & Sons, Inc, Hoboken, NJ.

Nguyen, T.V., Walton, C.W., White, R.E.,Van Zee, J., 1986. Parallel-Plate Electrochemical Reactor Model. Journal of the Electrochemical Society 133, 81-87.

Petersen, M.A., Sale, T.C.,Reardon, K.F., In Press. Electrolytic Trichloroethene Degradation using MIxed Metal Oxide Coated Titanium Mesh Electrodes. Chemosphere, doi:10.1016/j.chemosphere.2006.11.056.

Šimek, M.,Roušar, I., 1988. Calculation of the Current Density Distribution in an Amalgam Electrolyser by the finite Element Method. Journal of Applied Electrochemistry 18, 96-103.

Smeltzer, J.C.,Fedkiw, P.S., 1991. Current Distribution in a Parallel-Plate Reactor: A Comparison of Steady and Sinusoidal Cell-Voltage Control. Journal of the Electrochemical Society 138, 3665-3673.

Snoeyink, V.L.,Jenkins, D., 1980. Water Chemistry. John Wiley and Sons, Inc., New York.

Steffen, B.,Rousar, I., 1995. Numerical Methods for Electrochemical Modelling-I. Electrochimica Acta 40, 379-386.

Voudrias, E.A., 2001. Pump-and-treat remediation of groundwater contaminated by hazardous waste: Can it really be achieved? Global Network for Environmental Science and Technology: The International Journal 3, 1-10.

Wani, A.H., O'Neal, B.R., Gilbert, D.M., Gent, D.B.,Davis, J.L., 2006. Electrolytic Transformation of Ordinance Related Compounds (ORCs) in Groundwater: Laboratory Mass Balance Studies. Chemosphere 62, 689-698.

Wendt, H.,Kreysa, G., 1999. Electrochemical Engineering. Springer, Berlin.

White, R.E., Bain, M.,Raible, M., 1983. Parallel Plate Electrochemical Reactor Model. Journal of the Electrochemical Society 130, 1037-1042.

Tables

Table 3–1 Electrode mesh geometry dimensions.

	d_1 (mm)	d_2 (mm)	LD (mm)	SD (mm)
Baseline	1.4	0.63	3.2	1.1
Flat	1.68	0.214	3.2	1.1
Sharp	0.55	0.96	3.2	1.1

Figures

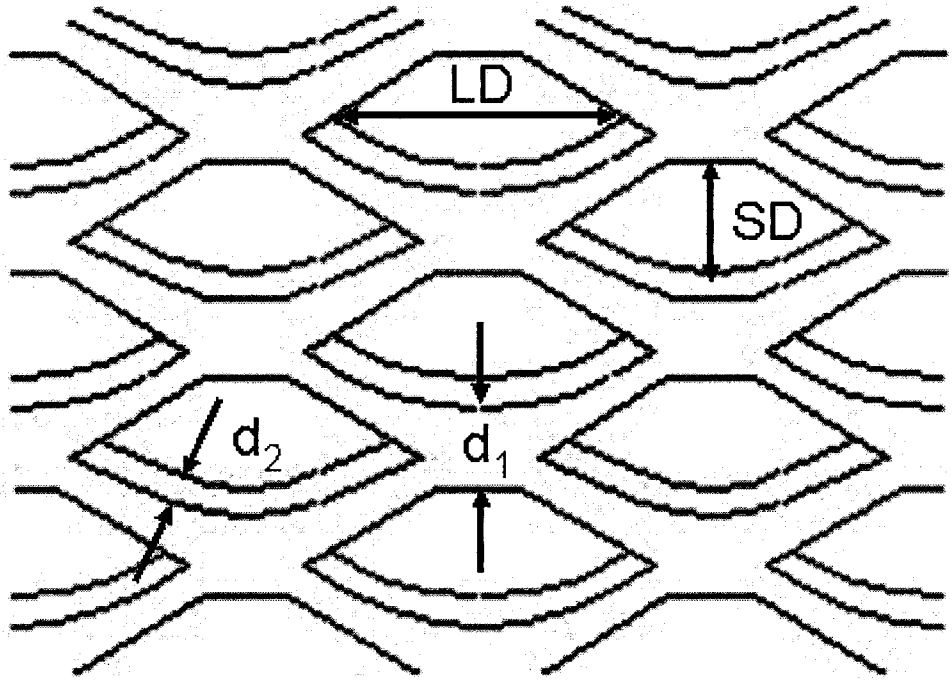

Figure 3–1 A schematic of the mesh electrode geometry. Two of the dimensions, d_1 and d_2, were altered in the numerical experiments. The dimension d_1 describes the distance between mesh apertures along the line denoting the SD dimension. The dimension d_2 describes the depth of the electrode aperture.

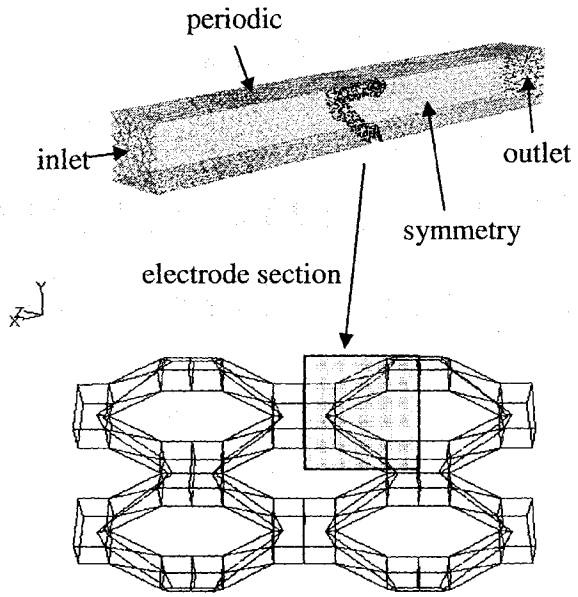

Figure 3–2 Physical domain of the CFD model. The volume of the solution domain was minimized by taking advantage of symmetry planes and periodic boundary conditions.

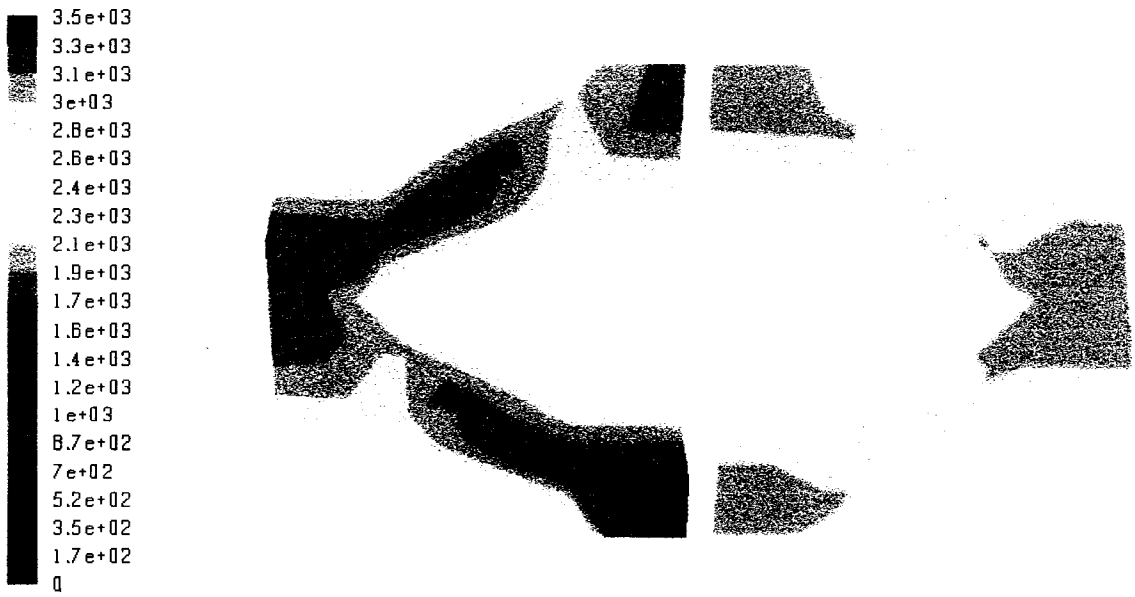

Figure 3–3 Current density (mA m^{-2}) on the upstream (left) and downstream (right) faces of the electrode.

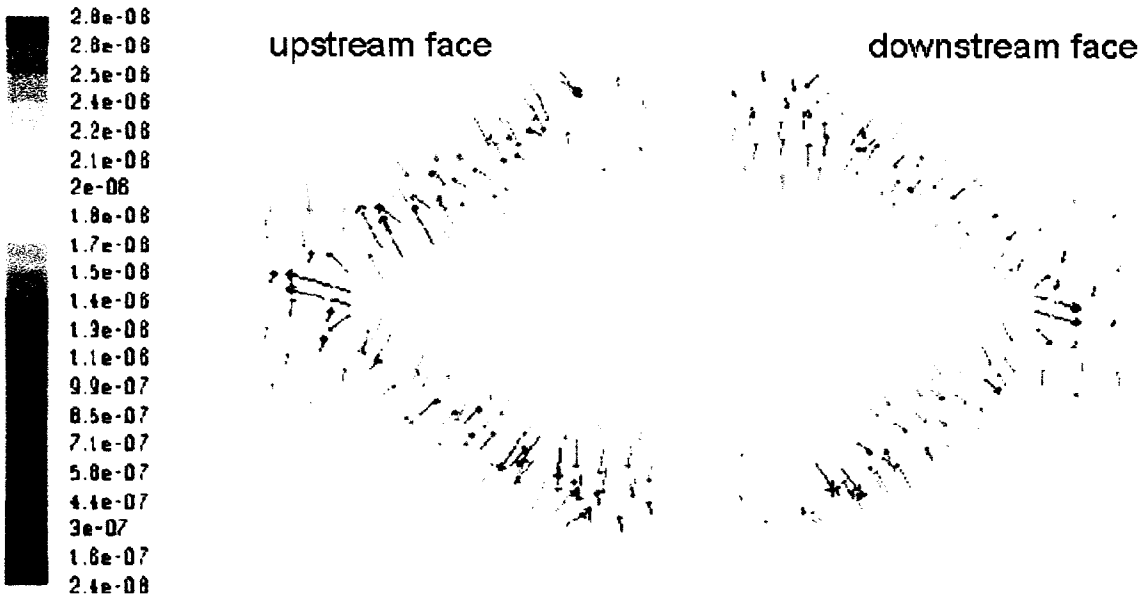

Figure 3–4 Vectors of RDX diffusion flux (kgmol m^{-2} s^{-1}) at the upstream (left) and downstream (right) faces of the electrode. Vector length corresponds to the flux magnitude.

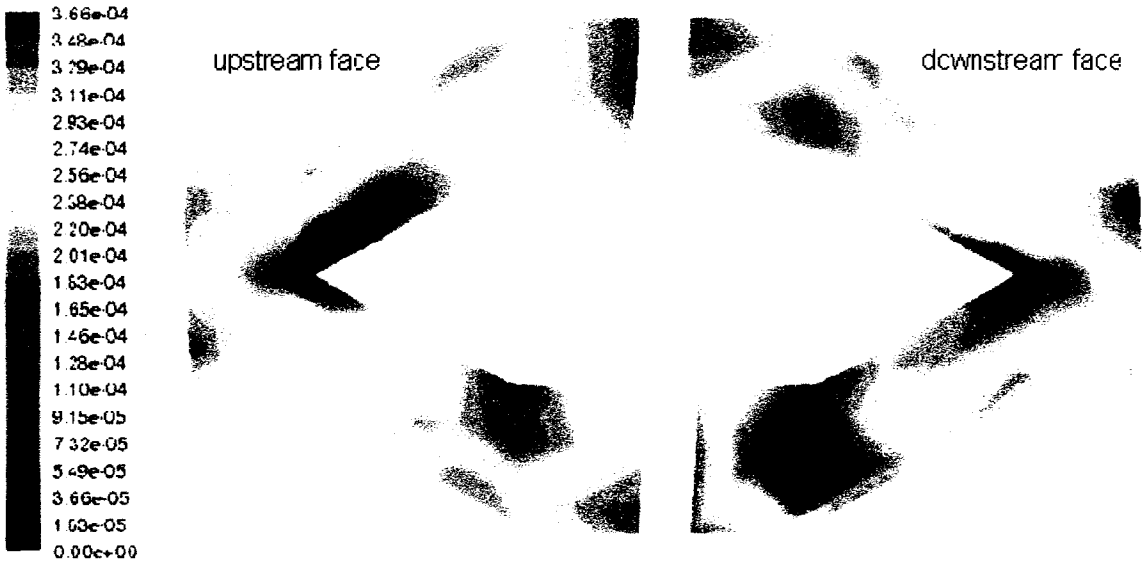

Figure 3–5 Contours of Da_{mod} (A.U.) at the upstream (left) and downstream (right) faces of the electrode.

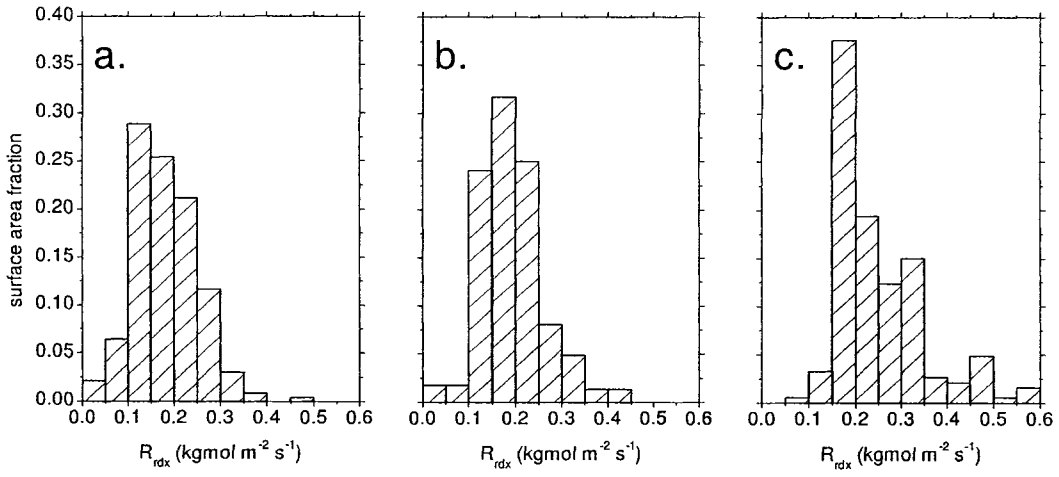

Figure 3–6 RDX reaction rate distributions at the electrode surface for the sharp (a), baseline (b), and flat (c) geometries.

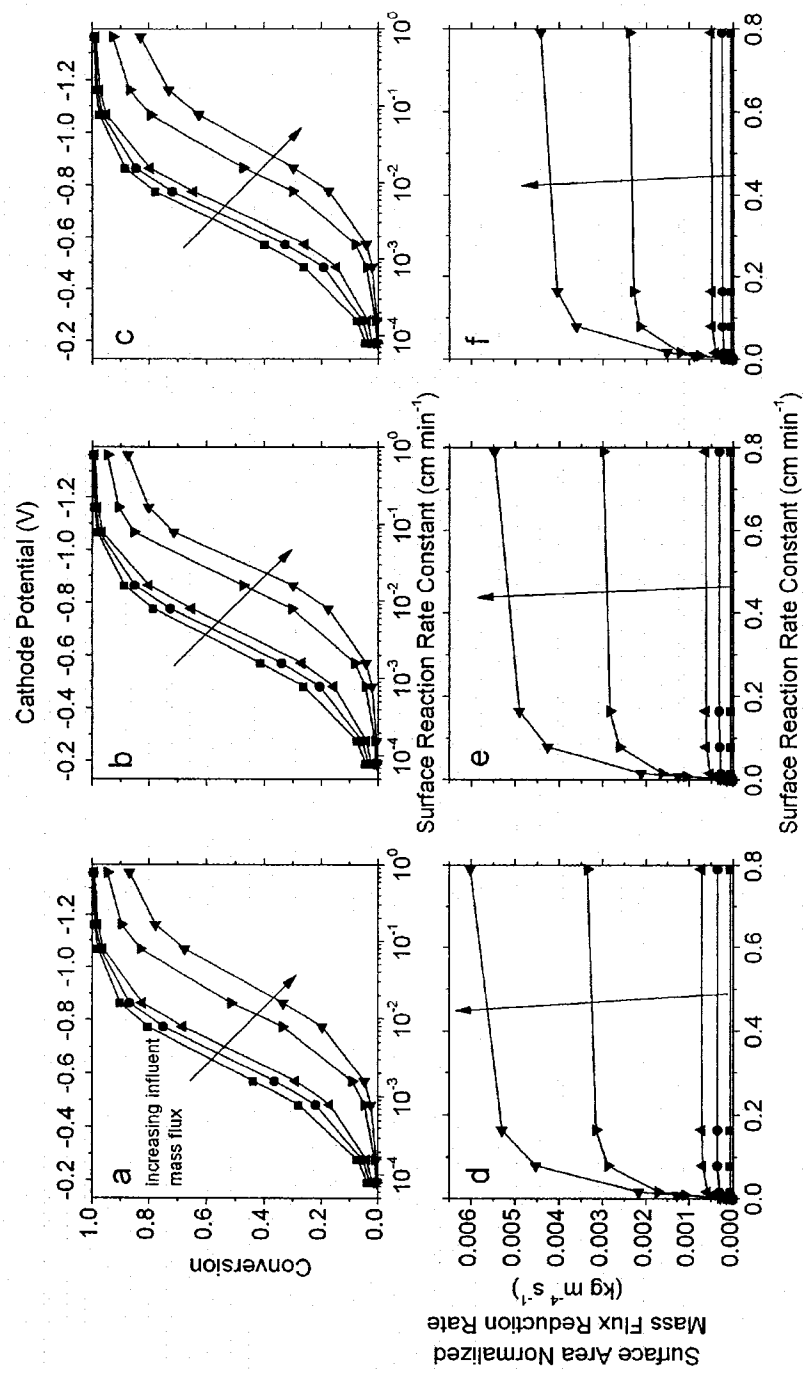

Figure 3–7 Conversion (a – c) and surface area normalized RDX flux reduction rate (d – f) at the flat (a and d), baseline (b and e), and sharp (c and f) geometries.

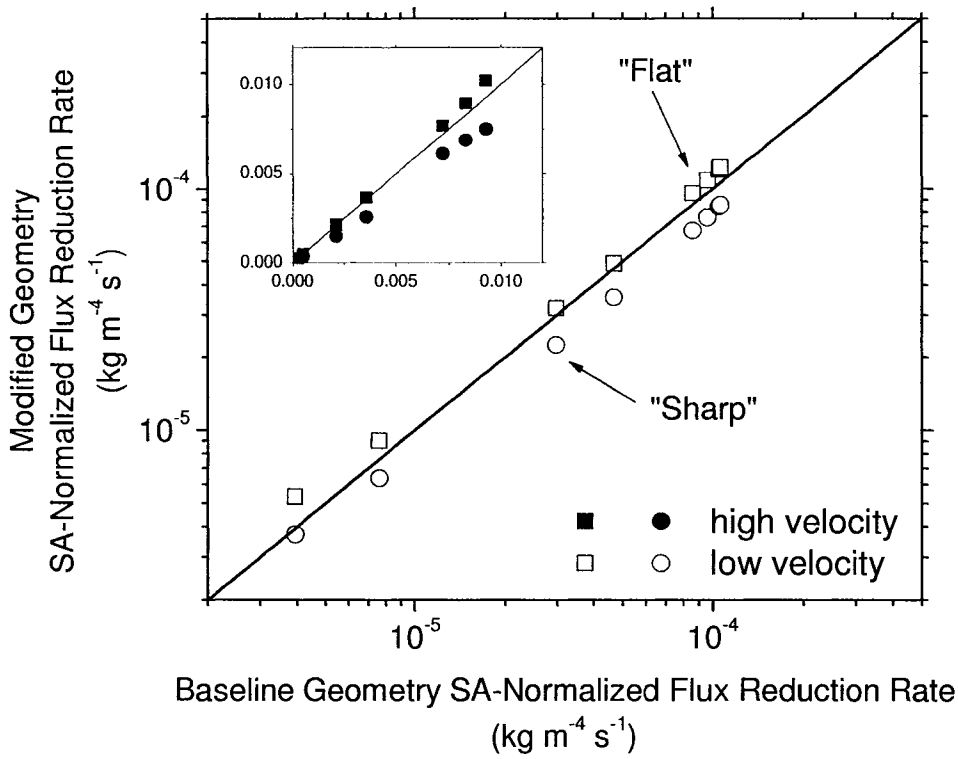

Figure 3–8 Ratio of surface area normalized RDX flux reduction rates of the sharp:baseline and flat:baseline geometry at the highest and lowest inlet velocities evaluated.

CHAPTER IV:

EFFECT OF GAS EVOLUTION ON MIXING AND CONVERSION IN A FLOW-THROUGH ELECTROCHEMICAL REACTOR

Abstract

Models of groundwater remediation system performance are useful in the design and diagnosis of in situ applications for groundwater remediation. Permeable reactive barriers (PRBs) that use planar mesh electrodes for the reactive substrate sandwiched between an inert porous material (e⁻barriers) may provide a greater degree of applicability (independence from field conditions) and operating flexibility (easily manipulated reaction rates) than current technologies. In e⁻barriers, water electrolysis and associated gas generation occurs concomitantly with contaminant degradation. Due to the large rate of gas generation relative to convection through the reactor, gas evolution has the potential to impact system performance. Using empirically derived relationships for reactant transport and gas-evolution induced mixing, a general e⁻barrier reactor model was developed. Comparison of model predictions with experiments using ferricyanide as a representative contaminant demonstrated that incorporating gas generation into the model was necessary for accurate performance predictions over a range of representative operating conditions. Further insights were obtained by introducing dimensionless

variables (Peclet and Damköhler numbers) that could be related for given groundwater flow and gas production rates. This model provides a basis for the design of e⁻barriers and a framework for further research on these systems.

4.1 Introduction

Permeable reactive barriers (PRBs) have become a popular technology for controlling the migration of groundwater contamination away from source zones. Traditionally, PRBs have been constructed with a permeable reactive medium (e.g., granular zero-valent iron (Gillham and O'Hannesin, 1994; Matheson and Tratnyek, 1994)) placed in a trench to intercept a plume of groundwater contamination. The permeable medium allows the natural hydraulic gradient to transport contaminants into the system, where they react to form environmentally benign compounds. Recently, research focused on electrolytic PRBs, e⁻barriers (Gilbert and Sale, 2005; Wani et al., 2006; Petersen et al., 2007), has evaluated this new technology as an option for plume migration control. e⁻Barriers offer some distinct advantages over more traditional in situ remediation technologies. In particular, the ability to modify subsurface reaction conditions by controlling electrode potentials provides a large degree of operating flexibility. The advantages of these systems make them compelling to further explore.

Process models that accurately predict how remediation systems behave under a variety of operating conditions are important in both the design and monitoring phases. Previous modeling efforts for PRB systems with granular media have used plug-flow assumptions (Starr and Cherry, 1994; Yabusaki et al., 2001), or numerical models

(Hatfield et al., 1996; Rabideau et al., 2005) and qualitative observations (Fryar and Schwartz, 1998; Kamolpornwijit et al., 2003; Painter, 2004; Liang et al., 2005) that account for dispersion and nonuniform flow fields within the system. However, the vast difference in physical configuration between e⁻barriers and other PRB media is a significant shift in the conceptual model of hydrodynamic and mass transfer environment within a subsurface implementation.

Under most of the conditions and contaminants we have evaluated, the reaction rates required to achieve significant removal of contaminants are attained in conjunction with water electrolysis. The resulting gas generation at the electrode surfaces creates a complex hydrodynamic and mass transport environment. A central hypothesis of this research is that the effects of gas generation must be taken into account in an e⁻barrier process model in order to correctly describe performance under operating conditions relevant to a subsurface implementation. With an appropriate model, experimentally measurable parameters (e.g., electrode potential, current density, reactant load, etc.) may be used to predict reactant conversion and selectivity.

The objective of this research was to develop a macroscopic process model of the e⁻barrier system. The effects of gas generation were incorporated into a basic one-dimensional convection/dispersion reactor model. Model parameters were adapted to account for gas generation using both relationships derived as part of this research, and previously published developments for gas-generating electrodes. The one-electron reduction of ferricyanide ($Fe(CN)_6^{3-}$) to ferrocyanide ($Fe(CN)_6^{4-}$) was used as the model chemical system in a laboratory flow-through column reactor. Reactive tracer tests under mass transfer controlled conditions, with and without hydrogen gas generation at the

cathode, were employed to measure the model parameters relating to local mixing and mass transfer rate. These parameter values were then used in model predictions of conversion and current efficiency that were compared to steady-state experiments.

4.2 Model Development

4.2.1 Basic Reactor Model

The discretely layered electrode assembly (Figure 4–1 inset) was approximated as a continuum, while still retaining important system features relevant to overall performance were retained. A one-dimensional species balance around the reaction system for the arbitrary dilute reactant A, which undergoes the first-order reaction A→B is

$$\frac{dC_A}{dt} + u\frac{dC_A}{dx} = D\frac{d^2C_A}{dx^2} - kC_A \ , \qquad (4\text{–}1)$$

where t is time, u is the mass-average velocity in the x direction, C_A is the spatially variable concentration of species A, x is the distance from the system inlet, D is the dispersion coefficient, and k is the reaction rate constant. Conversion may be calculated by integrating the steady-state form of Equation 4–1 over the length (L) of the electrode assembly in the direction of flow using the closed-vessel (i.e., Danckwerts) boundary conditions to produce

$$\chi_A = 1 - \frac{4a\exp\left(\frac{1}{2}\mathrm{Pe}_m\right)}{(1+a)^2\exp\left(\frac{a}{2}\mathrm{Pe}_m\right) - (1-a)^2\exp\left(-\frac{a}{2}\mathrm{Pe}_m\right)}, \qquad (4\text{–}2)$$

$$a = \sqrt{1 + 4k\tau(\mathrm{Pe}_m)^{-1}}$$

where χ_A is the conversion of A over the length (L) of the reactor, Pe_m (= uL/D) is a Peclet number for mixing, and τ is the residence time through the system (Danckwerts, 1953). The basic reactor model in Equations 4–1 and 4–2 were adapted through the model parameters D and k to account for electrolytic gas generation.

Gas generation and its effect on fluid mixing and mass transfer in electrochemical reactors has been examined in both static (Sedahmed and Shemilt, 1984; Sedahmed, 1987; Shah and Jorne, 1989; Vogt, 1989) and continuous flow processes (Janssen, 1987; Shah and Jorne, 1989; Bisang, 1993; Wu and Rangaiah, 1993; Wu et al., 1993). Although groundwater treatment in an e⁻barrier is a continuous process, the groundwater velocity is typically very small and bulk fluid convection may play only a small role in mass transfer and the extent of mixing. Therefore, theoretical and empirical relationships developed for static systems were explored in addition to those reported for flow systems to modify model parameters.

The rate of gas generation was calculated assuming that only two reactions occurred at the cathode: the reduction of the reactant and the reduction of the solvent (water). The gas evolution rate may then be calculated as a function of current via Faraday's law

$$Q_g = \frac{I}{A_E}(1-\phi_A)\frac{RT}{n_S FP}\ , \qquad (4\text{–}3)$$

where Q_g is the surface area normalized volumetric gas evolution rate, I is the current, A_E is the electrode surface area, ϕ_A is the current efficiency for the reactant, R is the universal gas constant, T is the absolute temperature, n_S is the number of electrons transferred in the solvent reduction reaction, F is Faraday's constant, and P is the pressure in the gas phase. Pressure was assumed to be close to 1 atm and subject to the ideal gas law. The term $(1-\phi_A)$ in Equation 4–3 was assumed to be approximately one in the case of solvent decomposition, since solvent is present in great excess compared to other constituents. This assumption allowed Q_g to be calculated without prior knowledge of the current efficiency.

4.2.2 Effect of Gas Evolution on Dispersion

Gas evolution in e⁻barriers is visible as turbulent conditions within the bulk fluid phase near the electrodes. The extent of mixing was treated within the e⁻barrier model through the dispersion coefficient, D. The theoretical limits of D are those corresponding to plug flow ($D \rightarrow 0$) and perfect mixing ($D \rightarrow \infty$) (Levenspiel, 1999). For an e⁻barrier in gas-evolving conditions, the extent of mixing will be between these theoretical limits, and will depend on the local groundwater velocity and gas evolution rate. Dispersion coefficients used in the model were measured directly from tracer experiments, described in the proceeding section. A single-phase continuum model for dispersion under similar

experimental conditions could not be located within the literature. Therefore a multi-variable regression model was generated from the data and utilized in this analysis.

4.2.3 Effect of Gas Generation on Mass Transfer

The mass transfer of a reaction species from a bulk fluid to an electrode surface has been shown to be impacted by the mechanics of bubble formation, attachment, and ascension. Sedahmed and Shemilt (1984) developed an empirical model for mass transfer coefficient to hydrogen-evolving mesh electrodes in a quiescent electrolyte. That model was modified to describe the mass transfer coefficient for gas generation-induced flow as

$$k_{mt,g} = a\left(Q_g\right)^b , \qquad (4\text{–}4)$$

where $k_{mt,g}$ is the mass transfer coefficient under gas-evolving conditions, and a and b are fitting parameters. The value of b, determined by Sedahmed and Shemilt (1984) to be 0.19, was valid for planar electrodes oriented horizontally or vertically.

The local velocity field around a reacting surface also influences the diffusion profile. The simultaneous contributions of bulk fluid velocity and gas generation on enhancing the mass flux of reactant to the electrode surface are treated by addition of their associated mass fluxes (Wendt and Kreysa, 1999). The overall mass transfer coefficient can then be calculated as the vectorial sum of the two contributing processes

$$k_{mt} = \sqrt{k_{mt,g}^2 + k_{mt,c}^2} \quad , \tag{4–5}$$

where $k_{mt,c}$ is the mass transfer coefficient that is due purely to the convective flow field, which was determined experimentally. The pseudo-volumetric consumption rate constant (k) in Equation 4–1 is related to k_{mt} by

$$k = k_{mt} \frac{A_E}{V_R} \quad , \tag{4–6}$$

where V_R is the reactor volume.

4.2.4 Dimensionless Governing Equation

To examine the broader implications of the gas-generation model framework, Equation 4–1 was non-dimensionalized by introducing a dimensionless length ($\bar{x} = x/L$) and concentration ($\bar{c} = C_A/C_{A,0}$) into Equation 4–1

$$\frac{d^2\bar{c}}{d\bar{x}^2} = \mathrm{Pe_m} \frac{d\bar{c}}{d\bar{x}} + \mathrm{Da_m}\bar{c} \quad , \tag{4–7}$$

where $\mathrm{Da_m}$ is a mixing Damköhler number equal to kL^2/D and $\mathrm{Pe_m}$ was defined in §4.2.1. Recognizing that $k\tau = \mathrm{Da_m}(\mathrm{Pe_m})^{-1}$, Equation 4–2 was recast in terms of $\mathrm{Da_m}$ and $\mathrm{Pe_m}$ to calculate χ in terms of the two dimensionless variables. Considering how $\mathrm{Da_m}$ and $\mathrm{Pe_m}$

are a function of Q and Q_g provides a basis to analyze system performance in terms of the relative processes described by the dimensionless groups.

4.2.5 Current Efficiency

Current efficiency and conversion are coupled by the relative reaction rates for each species in the system. *A priori* determination of current efficiency is important to estimate the power cost at various operating conditions. Current efficiency was defined as the ratio of partial current density (i.e., one particular reaction rate) of a single species to the total current density (i.e., sum of all reaction rates) (Sterten and Solli, 1996).

Considering a system with only two reactions — electron transfer of a dilute species and solvent decomposition on the electrode leading to gas evolution — current efficiency may be written as

$$\phi_A = \frac{j_A}{j_A + j_S}, \tag{4–8}$$

where j_A is the current density attributable to the reaction of species A and j_S is the current density attributable to solvent decomposition. Two assumptions can be made to cast j_A and j_S in terms of parameters that are experimentally controlled. First, the rate of solvent decomposition was assumed to be linearly dependent on electrode potential. The consequence was j_S may be calculated by the linear approximation of the Tafel equation

$$j_S = -j_{0,S}\frac{n_S F}{RT}\left(\psi_C - E_S^0\right), \tag{4–9}$$

where $j_{0,S}$ is the exchange current density of the solvent, ψ_C is the cathode potential relative to the standard hydrogen electrode (SHE), and E_S^0 is the standard reduction potential of the $H_2O/H_2,OH^-$ couple relative to SHE (Bard and Faulkner, 2001).

The second assumption for the current efficiency model was that the reaction rate of the dilute species was controlled by mass transfer to the electrode surface. This assumption may be justified in cases were the standard redox potential of the species is much smaller in magnitude than the solvent decomposition potential. Consequently, when solvent decomposition is energetically favorable at a specific electrode potential, the electron transfer kinetics of the dilute species are presumedlarge enough that mass transfer controls its overall reaction rate. When these two assumptions were applied, Equation 8 may be rewritten as

$$\phi_A = \frac{n_A F k_{mt} C_A^{bulk} / A_E}{n_A F k_{mt} C_A^{bulk} / A_E + j_{0,S} n_S F \left(E_S^0 - \psi_C\right) / RT}, \qquad (4\text{–}10)$$

where n_A is the amount of electrons transferred in the reaction of species A and C_A^{bulk} is the concentration of species A in the bulk phase.

4.3 Materials and Methods

4.3.1 Materials

Potassium ferricyanide (Fisher, ACS grade), potassium ferrocyanide trihydrate (Acros, ACS grade), anhydrous potassium phosphate dibasic (Fisher, ACS grade), potassium phosphate monobasic (Fisher, enzyme grade), N-phenylanthranilic acid (Acros, 98% purity), and cerium(IV) sulfate tetrahydrate (Acros, 99+% purity) were purchased and used without further purification. Concentrated hydrochloric acid (Mallinckrodt) and pelletized sodium hydroxide (Fisher, ACS grade) were used to make diluted acid and base solutions. All experimental and analytical method solutions were created using deionized water.

4.3.2 Tracer

Parameter measurements and system performance were evaluated in transient and steady-state tracer tests. Ionic species such as bromide and chloride were not suitable tracers since they would likely be oxidized at the anode. Instead, potassium ferricyanide was chosen as the tracer. The ferricyanide ion and the reduced species ferrocyanide form a well described electrochemical redox couple with applications in electrochemical and biological sensors (Gros and Comtat, 2004; Li et al., 2005; Ostatná et al., 2005). The one-electron reduction of $Fe(CN)_6^{3-}$ to $Fe(CN)_6^{4-}$ has a standard reduction potential of 0.36 V vs. SHE, more than one volt more positive than the reduction potential of the $H_2O/H_2,OH^-$ couple (-0.83 V vs. SHE). Therefore, at a H_2-evolving cathode (ψ_c < -0.83

V vs. SHE), ferricyanide will be reduced at a rate that can be assumed to be limited by mass transfer to the electrode.

4.3.3 Equipment Description

Experiments conducted to determine system parameters and validate the process model were carried out using a laboratory-scale e⁻barrier reactor constructed within a 20-cm long by 5-cm ID Plexiglass column (Figure 4–1). The electrode assembly (Figure 4–1, inset) was constructed with an expanded titanium mesh electrode, coated with a mixed metal oxide (Elgard 150 Anode Ribbon Mesh, Corrpro Companies Inc) and had an approximate volume of 39 cm^3. The remainder of the column was packed with clean quartz-feldspar sand as a representative soil. The surface area of a single electrode was ca. 50 cm^2. Layers of Geonet and Geotextile (Tenax, Baltimore, MD), two inert, nonconductive, high-density polyethylene materials, were used to separate the electrodes, provide open space for gas bubbles to freely ascend, and keep sand from infiltrating the assembly. A Nytex screen (Wildco, Buffalo NY) was placed between the electrodes to separate the cathode section from the gas evolution effects of the anode section. Power was applied to the electrodes using a GW Laboratory DC Power Supply (model GPS-3030D) in a constant current mode. Electrode potentials were measured relative to Ag/AgCl reference electrodes (World Precision Instruments Inc., Sarasota, FL) placed ca. 0.5 cm from the electrode surface. Electrode potentials were recorded on 1-min intervals with LabView 7.0 Express (National Instruments, Austin, TX) using a National Instruments PCI-6024E data acquisition device. Gas was vented through a port at the top of the electrode assembly attached to a Tedlar bag (SKC Inc., Eighty Four, PA) with a

Tygon hose. The feedstock and effluent solutions were stored in 1-L Erlenmeyer flasks. The solution was pumped through the column using an Ismatec (Switzerland) Reglo analog compact multi-channel variable speed pump and all connections were made with Viton and Teflon tubing (VWR, Vernon Hills, IL).

4.3.4 Transient Experiments

Prior to tests with gas-evolving electrodes, no-power control breakthrough tests were performed to determine dispersion through the system in the absence of gas generation, and to verify that there were no preferential flow paths through the column packing. The dispersion coefficient calculated from the ferricyanide concentration breakthrough as a result of a 0 to 5 mM step increase in influent concentration was 0.005 $cm^2\ min^{-1}$. The resulting breakthrough curve was absent of peaks or a long tail, indicating that preferential flow paths were not formed and that the column was well packed.

The extent of mixing within the electrode assembly as a function of gas evolution rate and liquid flowrate was evaluated using step increase tracer tests. Breakthrough curves as a result of a step increase in ferricyanide concentration from 0 mM were measured for volumetric flowrates (0.1, 0.5, and 1.5 mL min^{-1}) and three applied currents (0.05, 0.1, and 0.2 A). The influent tracer concentration was 5 mM. The supporting electrolyte for all experiments was an aqueous 0.1 M KH_2PO_4/Na_2HPO_4 buffer solution (pH 7). Column effluent samples were acquired at 10- to 60-min intervals, depending on the flowrate, and stored in 2-mL glass vials at room temperature (ca. 22 °C) in the dark.

The dispersion coefficient at different gas generation rates may be estimated using conservative tracer methods. Starting with Equation 4–1 for a non-reactive species the response in effluent concentration to a step input of an inert tracer from zero to $C_{T,0}$, introduced at the reactor inlet (Danckwerts, 1953), is

$$C_T(x,t) = \frac{C_{T,0}}{2}\operatorname{erfc}\left(\frac{x-ut}{\sqrt{4Dt}}\right). \qquad (4\text{–}11)$$

Equation 4–11 is valid at large Pe_m (> 100) for both open and closed boundary conditions. Setting $x = L$ allows transient concentration data from a step tracer experiment to be fit to Equation 4–11 using D and u as the regression variables.

To reconcile the fact that ferricyanide was converted through the system, it was recognized that the ferrocyanide production rate was equal to the rate of ferricyanide consumption. Consequently, a governing equation for the tracer in terms of the combined ferricyanide and ferrocyanide molar concentration was utilized. This development assuming that neither species was preferentially sequestered at the electrode, assembly components, or the porous matrix. This was verified by batch adsorption experiments performed prior to the study. The breakthrough curve of total $Fe(CN)_6^{3-}$ and $Fe(CN)_6^{4-}$ molar concentration was fit to Equation 4–11 to determine D as a function of experimental conditions. Since different current densities produced different gas void fractions within the system, the mean residence time ($C_T/C_{T,0} = 0.5$) fluctuated as a function of experimental conditions. To improve the data regression fit, u

was also used as a fitting parameter. Regression was performed in Mathcad 12.0 with the Levenburg-Marquardt nonlinear regression method.

4.3.5 Steady-State Experiments

System performance, expressed as ferricyanide conversion and current efficiency, was evaluated in steady-state column experiments. The flowrate and current conditions were the same as those used in the transient experiments. The steady-state conversion (χ) and current efficiency (ϕ) for ferricyanide were calculated for each void volume after effluent concentrations were constant. This usually occurred after two to three void volumes were pumped through the column. The reported experimental conversion and current efficiency were averages of the three to four χ and ϕ calculations under steady-state conditions.

Additional steady-state experiments were performed in the absence of gas generation to estimate the convective mass transfer coefficient ($k_{mt,c}$) as a function of the liquid flowrate. The cathode potential was set from -0.4 to -0.5 V vs. SHE, approximately one volt more negative than the $Fe(CN)_6^{3-}/Fe(CN)_6^{4-}$ standard reduction potential, but not sufficiently negative to produce H_2 gas (< -0.8 V vs. SHE). Since no gas was generated, k_{mt} simplifies to $k_{mt,c}$, and k_{mt} was determined using the experimentally determined steady-state conversion with Equations 4–2 and 4–6. The value for D was taken from the no-current control transient experiments (0.005 cm^2 min^{-1}).

4.3.6 Analytical Methods

Ferricyanide concentrations were determined by visible light absorbance at 470 nm using a Perkin-Elmer model 124 double-beam spectrophotometer. Concentrations were calculated by comparing the absorbance to standard solutions (0 to 7.5 mM) of $Fe(CN)_6^{3-}$ in the 0.1 M pH 7 phosphate buffer solution. The ferricyanide detection limit of the spectrophotometric method was 0.05 mM. Ferrocyanide concentrations were determined by redox titration with cerium(IV) sulfate to an E_h of 0.905 V vs. SHE using N-phenylanthranilic acid as an end-point indicator. The ferrocyanide detection limit using the redox titration was 0.1 mM. The lack of ferrocyanide absorbance interference and ferricyanide titration interference was verified prior to conducting tracer experiments.

4.4 Results and Discussion

4.4.1 Impact of Operating Conditions on Dispersion

The response to the step increase in $Fe(CN)_6^{3-}$ influent concentration was adequately described using Equation 4–11 for the entire range of conditions analyzed in the transient, gas-evolving tracer experiments (Figure 4–2). In some cases, the value of Pe_m was smaller than 100, beyond the generally accepted limit of applicability for Equation 4–11 (Levenspiel, 1999). An alternative method, using the derivative of the step response curve and analyzing the resulting function as an impulse type tracer experiment, was used to calculate D. The second approach resulted in values within one standard deviation of the original values; therefore, the values from the original computational method were used in the subsequent analyses.

The mixing conditions within the reactor were a function of both the current (i.e., gas evolution rate by Equation 4–3) and the nominal volumetric flowrate through the system (Table 4–1). The mean residence times ($t_{0.5}$) decreased, as expected, with increasing flowrates, but were variable with respect to changes in I (Table 4–1). This variability may have been due to the stochastic nature of the bubble-induced mixing mechanics or changes in pump tubing elasticity over time. At the highest Q_g, approximately 0.03 $cm^3\ cm^{-2}\ min^{-1}$, the values of D began to converge, similar to the results of Wu et al. (1993). This suggested that gas evolution controlled the hydrodynamic conditions under these operating conditions. Conversely, at the lower Q_g values, convective flow through the system controlled the hydrodynamic conditions within the electrode assembly. This was indicated by the larger range of D values at the lower Q_g over the range of nominal flowrates used, although the large variability in experimental data complicates this analysis.

4.4.2 Impact of Operating Conditions on Mass Transfer

Ferricyanide reduction under mass transfer controlled conditions in the absence of gas evolution was evaluated at the nominal flowrates of 0.1, 0.5, and 1.5 mL min^{-1} to determine $k_{mt,c}$. The convective mass transfer coefficient increased, from $3.5 \times 10^{-5} \rightarrow 7.6 \times 10^{-5} \rightarrow 1.26 \times 10^{-4}$ cm s^{-1}, with increasing nominal flowrate following a power law model ($k_{mt,c} \propto Q^z$) to the 0.3 power. This was close to the theoretical value of 0.33 for Sherwood number correlations for $k_{mt,c}$ with the Reynolds number for a submerged object in the creeping flow regime (Bird et al., 2002).

Surface area normalized gas evolution rates as a function of applied current were calculated using Equation 4–3 (Table 4–1). These normalized rates were used to calculate $k_{mt,g}$ using Equation 4–4 ($a = 3.25 \times 10^{-4}$ cm sec^{-1}, $b = 0.19$ from Sedahmed and Shemilt (1984)), and are presented in Figure 4–3A as a function of applied current. The overall mass transfer coefficient, k_{mt}, was calculated by Equation 4–5 for each experimental condition evaluated (Figure 4–3B). *A priori* calculated k_{mt} values began to plateau and converge as Q_g (or I) was increased.

4.4.3 Experimental and Predicted System Performance

System performance, expressed as ferricyanide conversion, was calculated from the steady-state experimental results and compared to predictions using Equation 4–2. Two sets of calculations were performed. The first set incorporated contributions from gas generation into D and k. Dispersion coefficients determined from the reactive tracer experiments were divided by 2 to account for the tracer passing through two gas-generating electrode chambers and substituted into Equation 4–2 for each discrete condition evaluated. The second set of calculations disregarded the impact of gas evolution on D and k ($D = 0.005$ cm^2 min^{-1}, k derived from Table 4–1 as a function of Q). These were performed to further illustrate the contribution of gas evolution effects on system performance. Assuming that each section behaved independently of the other, the dispersion coefficients are additive (Levenspiel, 1999). Equal dispersion between sections was a conservative estimate of the distribution based on the equal section residence times.

The experimental results generally agreed with predictions when the effects of gas generation were incorporated into the system model (Figure 4–4). Calculations that did not incorporate gas generation consistently underestimated conversion relative to the experiment results (Figure 4–4). It was expected that the best agreement between experimental results and gas-incorporated model calculations would occur at the largest gas evolution rate ($I = 0.2$ A), when gas generation exhibited the greatest influence on D and k_{mt}. The close agreement was not observed at 0.2 A, and experimental results were consistently lower than the expected conversion, although experimental variability was highest at this condition.

A probable cause for the lower than expected reactant conversion at high applied currents was the formation of a secondary reaction product, most likely the mixed-valent compound Prussian blue (Ogura et al., 1999). Blue deposits were found on the electrode surface and assembly materials after experiments run at 0.2 A. A combination of cycling the electrode polarities and flushing the electrode assembly through the column ports near the assembly appeared to remove the majority of deposits.

At the lowest liquid flowrate, where D was relatively small and system performance was expected to be analogous to a PFR, model predictions that incorporated gas generation at low Q_g ($I = 0.05$ A) compared well to the experimental results relative to the basic model (Figure 4–5). The experimental conversion exhibited a local maximum over the current range evaluated. The physical basis for the local maximum was speculated to be based on the relative contribution of gas generation towards mixing and mass transfer. Moderate gas generation rates may strike a balance between these two mechanisms that affect conversion oppositely (i.e., increased mixing decreases

conversion and increased mass transfer increases conversion). This concept is explored in §4.4.5 utilizing dimensional analysis.

Although the agreement was poor between experiment and model at $Q_g = 0.03$ cm^3 cm^{-2} min^{-1}, the overall results illustrate the necessity to incorporate gas generation into the model framework. Integrating gas generation imparts flexibility into the model that allows the variable mixing and mass transfer effects to be captured. Convergence between experimental results and model predictions may not necessarily validate the parameter modifications. However, it does provide the motivation to further investigate the reaction rate-controlling processes.

4.4.4 Comparison of Experimental and Predicted Current Efficiency

Current efficiency of $Fe(CN)_6^{3-}$ reduction (ϕ) calculated from Equation 4–10 and experimentally determined ϕ decreased with decreasing electrode potentials (Figure 4–6). Equation 4–5 overestimated ϕ by 0.15 to 0.25 at cathode potentials near E_s^0. Competing reactants such as dissolved O_2 and additional water reactions (e.g., reduction of water to hydroxyl radicals at metal oxide surfaces) may have contributed to the overall current at more positive potentials, decreasing $Fe(CN)_6^{3-}$ reduction efficiency. At more negative potentials, the rate of alternative water reduction pathways would be suppressed by the larger driving force of H_2O reduction directed towards H_2 evolution.

The form of Equation 4–10 dictates that current efficiency for a mass-transfer controlled reaction will decay as $|\psi_c|$ increases by $(1+|\psi_c|)^{-1}$. Therefore, ϕ will generally decrease when efforts are made to increase the rate of reduction by lowering the cathode

potential. This trend impacts the economic sustainability of an implementation since low efficiency processes would consume more power to treat the same contaminant flux as those of higher efficiency systems. Due to the small aqueous solubility of most organic groundwater contaminants, dissolved concentrations are often low (sub mM). Therefore, the electron cost for 100% conversion is very small under most circumstances. Consequently, the energy input cost at $\phi < 1$ may still be competitive with other PRB technologies (Sale et al., 2005).

4.4.5 Dimensional Analysis

The processes characterized by Pe_m are the relative rates of convective transport through the system to mixing transport within the electrode assembly. Da_m describes the relative rates of mass transfer controlled reaction to the mixing transport in the assembly. Both dimensionless groups are a function of u and Q_g (via k and D). Therefore, all of the processes characterized by Pe_m and Da_m are coupled, constricting the range of possible system operating conditions.

A localized weighted polynomial regression (*loess* localized regression function in Mathcad 12.0) was used to calculate D over the experimental variable ranges (u and Q_g). The empirical model was utilized with a given range of Da_m values centered on 1 to calculate corresponding values of Pe_m for specific Q and Q_g (Figure 4–7). As Q decreased, lines of constant Q_g separated and decreased for the same Q_g, indicating an increased impact of gas evolution on transport processes within the system. This would suggest that a larger extent of mixing dictates the operating conditions, possibly limiting

χ. Reactant conversion under this framework was evaluated to investigate the competing effects of gas evolution influenced mixing and mass transfer.

Values of χ were calculated for the sets of (Da_m, Pe_m) pairs at constant Q and Q_g using Equation 4–2 (Table 4–2). The spread between lines of constant Q_g in Figure 4–7 were replicated in the χ calculations. Conversion was maximized at the smallest Q and largest Q_g. These conditions correspond to (Da_m, Pe_m) pairs in the upper right quadrants of Figures 4–7A through C. In this region of the operating domain, the dominating mechanisms described by the dimensional analysis are the mass-transfer controlled reaction rate and convective transport through the assembly. Therefore, the relative impact of gas generation is greater towards enhancing mass transfer to the electrode surface than inducing mixing within the assembly.

The continuum assumption within the electrode assembly was revisited to address model accuracy. This assumption considers reactions to proceed uniformly within the reactor volume. The discrepancy between the assumed system and actual spatially nonuniform conditions in heterogeneous reactors has been treated by others using a catalyst-phase contact time distribution (Shinnar et al., 1972; Tayakout-Fayolle et al., 2005). This has been used to explain χ overestimation in heterogeneous reactors when a classical residence time distribution (RTD) was first applied. The present system differs from those considered in Tayakout-Fayolle et al. (2005) since reactions proceeded only on the electrode surface, and not in a separate catalyst phase (e.g., porous catalyst pellet). The probability of reactant contact with the electrode depends on the overall RTD. Although deconvoluting this relationship through experimental methods is a challenge, this concept was utilized to qualitatively evaluate the model prediction accuracy.

Examining Figure 4–4, the largest model-experimental discrepancies (average difference = 0.19) were at $Q = 0.1$ mL min^{-1}. At this flowrate, mixing tended to be the dominate transport mechanism according to the lower Pe_m values. Consequently, the continuum assumption in the well-mixed system would breakdown since reactants are less available for diffusion to the electrode when concentrations are more evenly distributed over space. As plug-flow characteristics become prevalent, the continuum assumption appears to remain valid. This was confirmed by the good agreement between model and experiment at the higher flowrate (average difference = 0.07; two conditions were statistically identical at the 95% confidence level).

4.5 Conclusion

Performance of a novel electrolytic PRB system was analyzed using a model that accounted for impact of gas generation on both transport and reaction mechanisms. Mixing within the electrode assembly was measured in terms of D with respect to flowrate through the system and gas generation rate. Although discrepancies existed between experimentally determined and predicted conversions, trends with respect to changes in operating conditions were suitably captured. Subsequent generalization of the results as a function of the dimensionless variables, Da_m and Pe_m, will permit more detailed analysis of both laboratory and field-based e⁻barrier systems through similitude based studies. The challenges of applying the model to large-scaled systems include determining the correct scaling methodology, accounting for nonuniformities imposed by aquifer heterogeneities, and the impact of more complex chemical systems that may not

be rate limited by purely mass transfer. In addition, the spatial stratification of chemical reactions within the systems, and its impact on conversion under well-mixed conditions, should be addressed due to the possible impact at flowrates relevant to field applications.

4.6 References

Bard, A.J.,Faulkner, L.R., 2001. Electrochemical Methods. John Wiley & Sons, Inc., New York, NY.

Bird, R.B., Stewart, W.E.,Lightfoot, E.N., 2002. Transport Phenomena. John Wiley & Sons, Inc., New York, NY.

Bisang, J.M., 1993. Effect of Mass Transfer on the Current Distribution in Monopolar and Bipolar Electrochemical Reactors with a Gas-Evolving Electrode. Journal of Applied Electrochemistry 23, 966-974.

Danckwerts, P.V., 1953. Continuous Flow Systems. Chemical Engineering Science 2, 1-18.

Fryar, A.E.,Schwartz, F.W., 1998. Hydraulic-Conductivity Reduction, Reation-Front Propagation, and Preferential Flow within a Model Reactive Barrier. Journal of Contaminant Hydrology 32, 333-351.

Gilbert, D.M.,Sale, T.C., 2005. Sequential Electrolytic Oxidation and Reduction of Aqueous Phase Energetic Compounds. Environmental Science and Technology 39, 9270-9277.

Gillham, R.W.,O'Hannesin, S., 1994. Enhanced Degradation of Halogenated Aliphatics by Zero-Valent Iron. Ground Water 32, 958-967.

Gros, P.,Comtat, M., 2004. A Bioelectrochemical Polypyrrole-Containing $Fe(CN)_6^{3-}$ Interface for the Design of a NAD-Dependent Reagentless Biosensor. Biosensors and Bioelectronics 20, 204-210.

Hatfield, K., Burris, D.R.,Wolfe, N.L., 1996. Analytical Model for Heterogeneous Reactions in Mixed Porous Media. Journal of Environmental Engineering.

Janssen, L.J.J., 1987. Mass Transfer at Gas-Evolving Vertical Electrodes. Journal of Applied Electrochemistry 17, 1177-1189.

Kamolpornwijit, W., Liang, L., West, O.R., Moline, G.R.,Sullivan, A.B., 2003. Preferential Flow Path Development and its Influence on Long-Term PRB Performance: Column Study. Journal of Contaminant Hydrology 66, 161-178.

Levenspiel, O., 1999. Chemical Reaction Engineering. John Wiley & Sons, New York, NY.

Li, G., Ma, N.Z.,Wang, Y., 2005. A New Handheld Biosensor for Monitoring Blood Ketones. Sensors and Actuators B 109, 285-290.

Liang, L., Moline, G.R., Kamolpornwijit, W.,West, O.R., 2005. Influence of Hydrogeochemical Processes on Zero-Valent Iron Reactive Barrier Performance: A Field Investigation. Journal of Contaminant Hydrology 78, 291-312.

Matheson, L.J.,Tratnyek, P.G., 1994. Reductive Dehalogenation of Chlorinated Methanes by Iron Metal. Environmental Science and Technology 28, 2045-2053.

Ogura, K., Nakayama, M.,Nakaoka, K., 1999. Electrochamical Quartz Crystal Microbalance and In Situ Infrared Spectroscopic Studies on the Redox Reaction of Prussian Blue. Journal of Electroanalytical Chemistry 474, 101-106.

Ostatná, V., Dolinnaya, N., Andreev, S., Oretskaya, T., Wang, J.,Hianik, T., 2005. The Detection of DNA Deamination by Electrocatalysis at DNA-Modified Electrodes. Bioelectrochemistry 67, 205-210.

Painter, B.D.M., 2004. Reactive Barriers: Hydraulic Performance and Design Enhancements. Ground Water 42, 609-617.

Petersen, M.A., Sale, T.C.,Reardon, K.F., 2007. Electrolytic trichloroethene degradation using mixed metal oxide coated titanium mesh electrodes. Chemosphere, doi:10.1016/j.chemosphere.2006.11.056.

Rabideau, A.J., Suribhatla, R.,Craig, J.R., 2005. Analytical Models for the Design of Iron-Based Permeable Reactive Barriers. Journal of Environmental Engineering 131, 1589-1597.

Sale, T., Petersen, M.,Gilbert, D., 2005. Final Report: Electrically Induced Redox Barriers for Treatment of Groundwater (CU-0112). ESTCP Project Number Project Number CU-0112.

Sedahmed, G.H., 1987. Mass Transfer at Packed-Bed, Gas-Evolving Electrodes. Journal of Applied Electrochemistry 17, 746-752.

Sedahmed, G.H.,Shemilt, L.W., 1984. Mass Transfer Characteristics of Electrochemical Reactors Employing Gas Evolving Mesh Electrodes. Journal of Applied Electrochemistry 14, 1.

Shah, A.,Jorne, J., 1989. Mass Transfer under Bubble-Induced Convection in a Vertical Electrochemical Cell. Journal of the Electrochemical Society 136, 144-153.

Shah, A.,Jorne, J., 1989. Mass Transfer under Combined Gas Evolution and Forced Convection. Journal of the Electrochemical Society 136, 153-158.

Shinnar, R., Naor, P.,Katz, S., 1972. Interpretation and Evaluation of Multiple Tracer Experiments. Chemical Engineering Science 27, 1627-1642.

Starr, R.C.,Cherry, J.A., 1994. In Situ Remediation of Contaminated Ground Water: The Funnel-and-Gate System. Ground Water 32, 465-476.

Sterten, Å.,Solli, P.A., 1996. An Electrochemical Current Efficiency Model for Aluminium Electrolysis Cells. Journal of Applied Electrochemistry 26, 187-193.

Tayakout-Fayolle, M., Othman, S.,Jallut, C., 2005. A New Technique for the Determination of Contact Time Distribution (CTD) from Tracers Experiments in Heterogeneous Systems. Chemical Engineering Science 60, 4623-4633.

Vogt, H., 1989. Mechanisms of Mass Transfer of Dissolved Gas from a Gas-Evolving Electrode and their Effect on Mass Transfer Coefficient and Concentration Overpotential. Journal of Applied Electrochemistry 19, 713-719.

Wani, A.H., O'Neal, B.R., Gilbert, D.M., Gent, D.B.,Davis, J.L., 2006. Electrolytic transformation of ordinance related compounds (ORCs) in groundwater: Laboratory mass nalance studies. Chemosphere 62, 689-698.

Wendt, H.,Kreysa, G., 1999. Electrochemical Engineering. Springer, Berlin.

Wu, W.S.,Rangaiah, G.P., 1993. Effect of Gas Evolution on Mass Transfer in an Electrochemical Reactor. Journal of Applied Electrochemistry 23, 1139-1146.

Wu, W.S., Rangaiah, G.P.,Fleischmann, M., 1993. Effect of Gas Evolution on Dispersion in an Electrochemical Reactor. Journal of Applied Electrochemistry 23, 113-119.

Yabusaki, S., Cantrell, K., Sass, B.,Steefel, C., 2001. Multicomponent Reactive Transport in an In Situ Zero-Valent Iron Cell. Environmental Science and Technology 35, 1493-1503.

Tables

Table 4–1 Mean residence time and dispersion coefficient as a function of flowrate and applied current or gas evolution rate.

	I = 0.05 A		I = 0.1 A		I = 0.2 A	
	Q_g = 0.007 cm^3 cm^{-2} min^{-1}		Q_g = 0.015 cm^3 cm^{-2} min^{-1}		Q_g = 0.030 cm^3 cm^{-2} min^{-1}	
Q (mL min^{-1})	$t_{0.5}$ (min)	D (cm^2 min^{-1})	$t_{0.5}$ (min)	D (cm^2 min^{-1})	$t_{0.5}$ (min)	D (cm^2 min^{-1})
0.1	1286	0.021 ± 0.005	1638	0.0061 ± 0.0009	1425	0.014 ± 0.002
0.5	293	0.032 ± 0.003	330	0.049 ± 0.008	376	0.101 ± 0.014
1.5	110	0.231 ± 0.041	103	0.256 ± 0.058	88	0.164 ± 0.059

Table 4–2 Predicted conversion as a function of Da_m and Pe_m pairs at constant liquid flowrate and gas generation rate.

Q		Q_g (cm^3 cm^{-2} min^{-1})	0.007		Q_g (cm^3 cm^{-2} min^{-1})	0.016		Q_g (cm^3 cm^{-2} min^{-1})	0.022		Q_g (cm^3 cm^{-2} min^{-1})	0.03	
(mL min^{-1})	Da_m		Pe_m	c		Pe_m	c		Pe_m	c		Pe_m	c
0.1	0.1		0.56	0.15		0.23	0.31		0.17	0.37		0.13	0.44
	0.5		1.25	0.30		0.52	0.51		0.39	0.58		0.29	0.65
	1		1.76	0.39		0.73	0.61		0.55	0.68		0.41	0.74
	5		3.94	0.65		1.63	0.84		1.22	0.88		0.92	0.91
	10		5.57	0.77		2.31	0.92		1.73	0.94		1.30	0.96
0.5	0.1		0.63	0.14		0.52	0.16		0.47	0.18		0.43	0.19
	0.5		1.41	0.27		1.16	0.31		1.05	0.34		0.96	0.36
	1		1.99	0.36		1.64	0.41		1.48	0.43		1.35	0.45
	5		4.45	0.62		3.66	0.67		3.31	0.70		3.02	0.72
	10		6.30	0.74		5.18	0.79		4.69	0.81		4.27	0.83
1.5	0.1		0.82	0.11		0.77	0.12		0.78	0.12		0.84	0.11
	0.5		1.83	0.22		1.71	0.24		1.74	0.23		1.89	0.22
	1		2.58	0.30		2.42	0.31		2.45	0.31		2.67	0.29
	5		5.78	0.54		5.42	0.56		5.49	0.56		5.97	0.53
	10		8.17	0.67		7.66	0.68		7.76	0.68		8.44	0.66

Figures

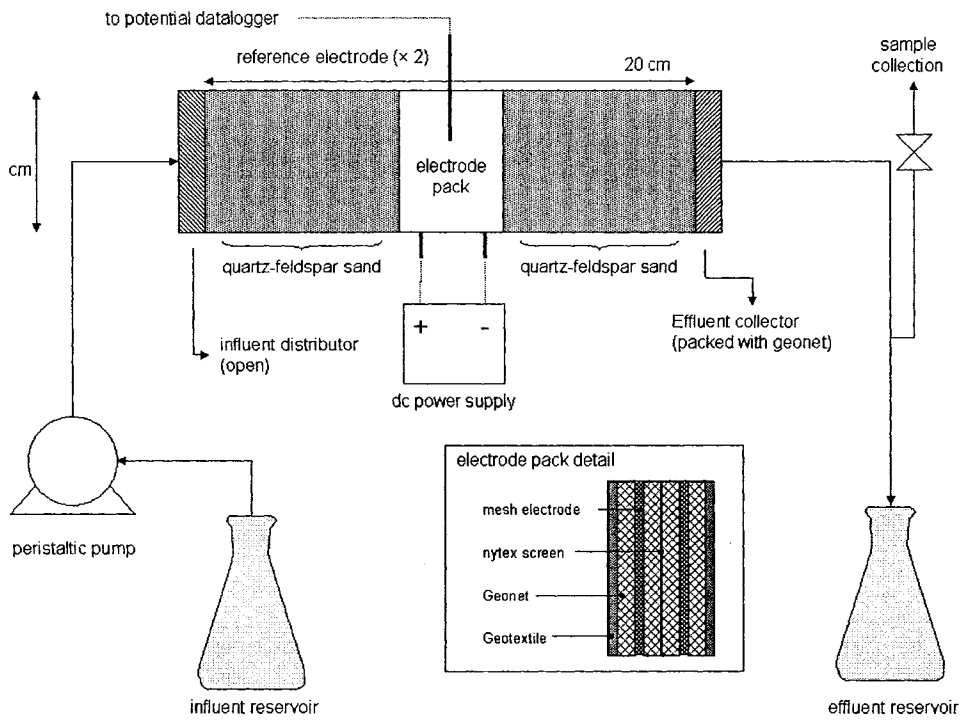

Figure 4–1 Schematic of the e⁻barrier experimental system.

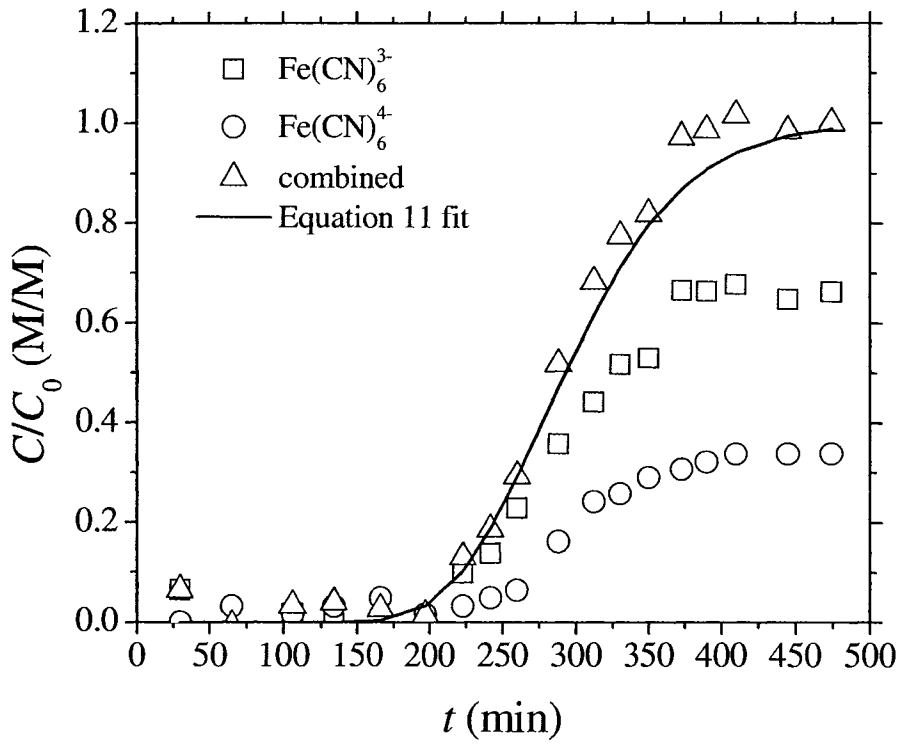

Figure 4–2 Multicomponenent breakthough curve at Q = 0.5 mL min^{-1} and I = 0.1 A. Solid line is the regression fit of Eqn 4 to the total molarity data.

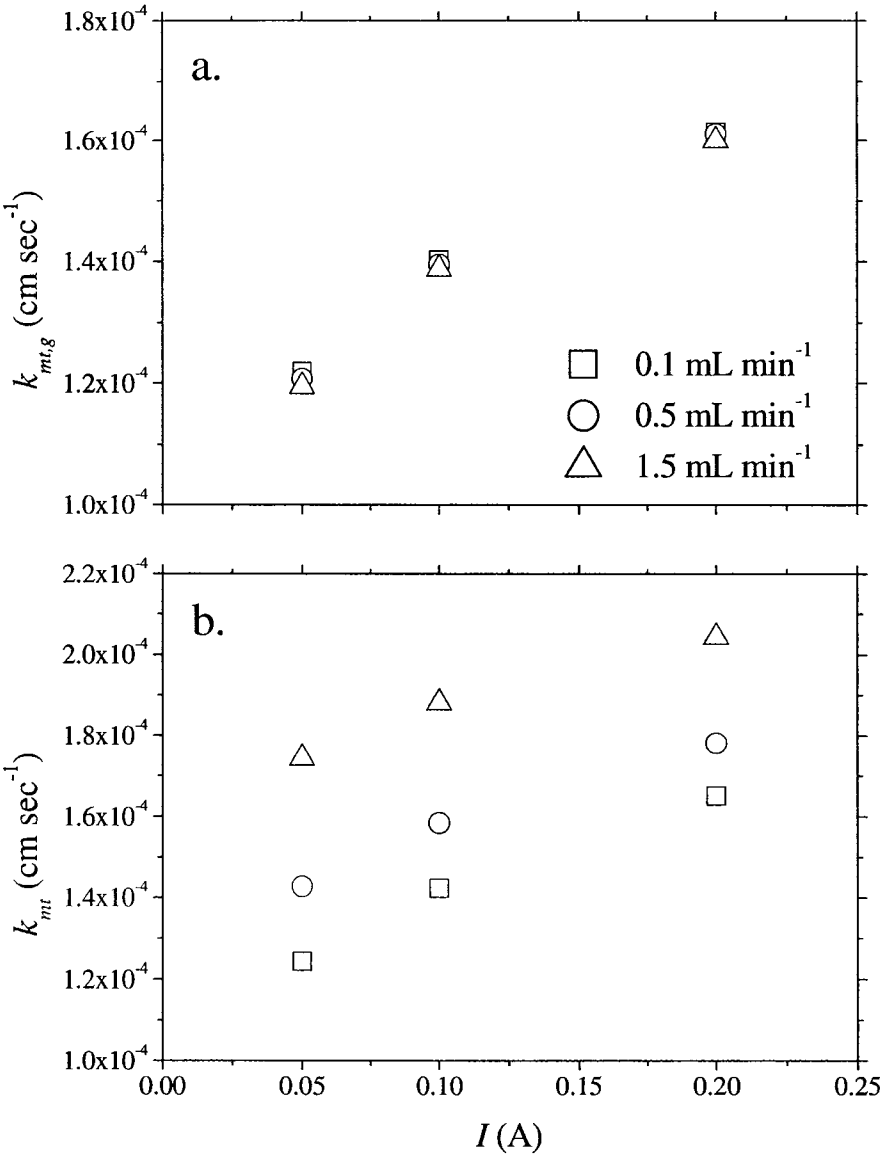

Figure 4–3 Mass-transfer coefficient due to (a) pure gas evolution, and (b) mass-transfer coefficient with convection and gas evolution contribution.

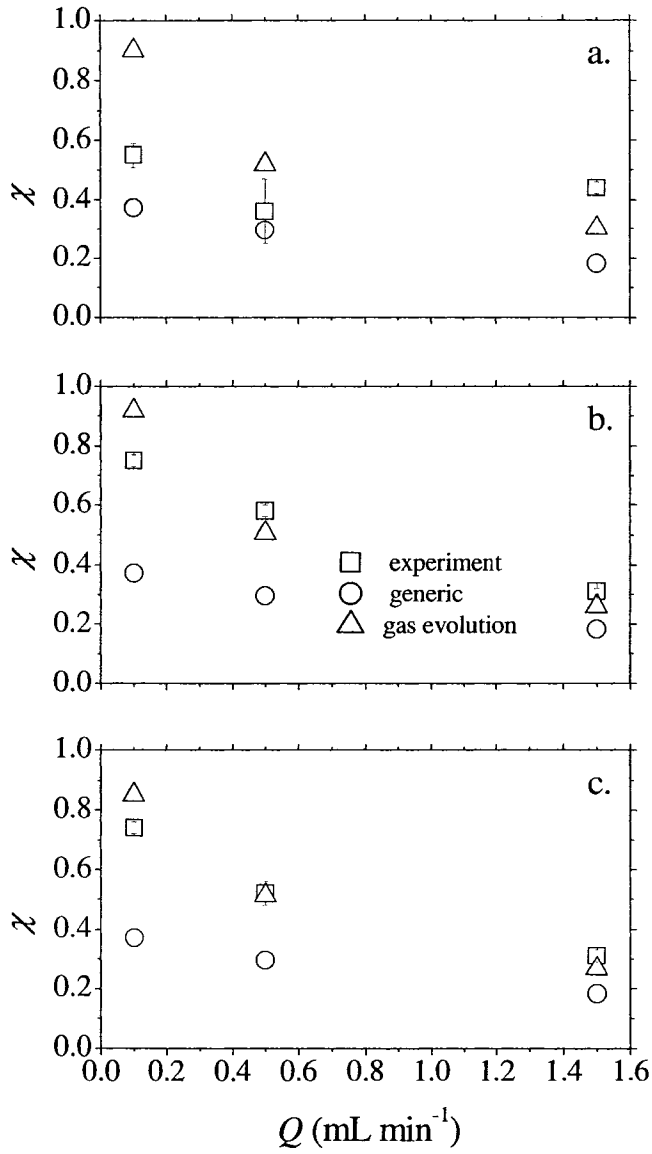

Figure 4–4 Conversion as a function of liquid flowrate (Q) at (a) I = 0.2 A, (b) I = 0.1 A, and (c) I = 0.05 A. Experimental data error bars represent one standard deviation of the average conversion.

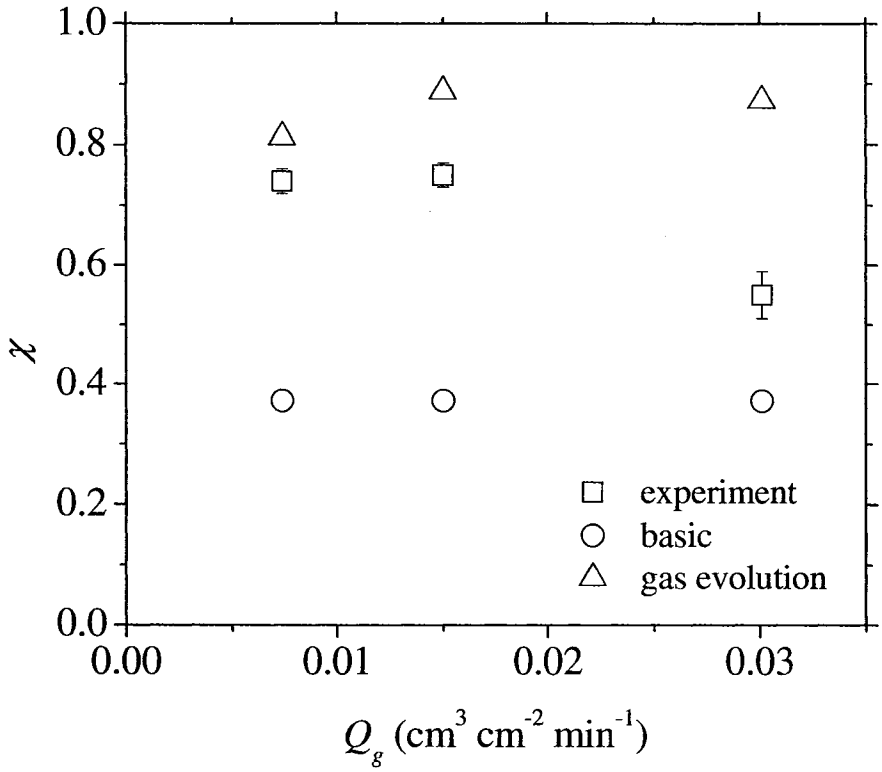

Figure 4–5 Predicted and measured conversion at three surface area normalized gas generation rates for $Q = 0.1$ mL min^{-1}. Experimental data error bars represent one standard deviation of the average conversion.

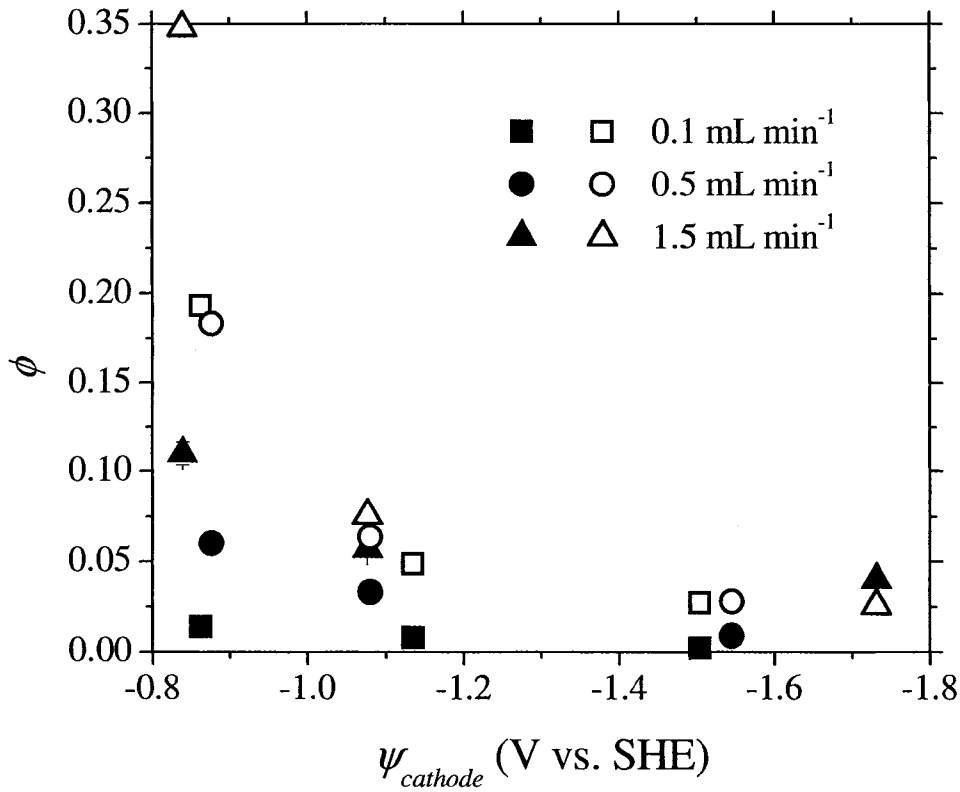

Figure 4–6 Measured (closed symbols) and predicted (open symbols) current efficiency as a function of flowrate and cathode potential. Experimental data error bars represent one standard deviation of the average conversion.

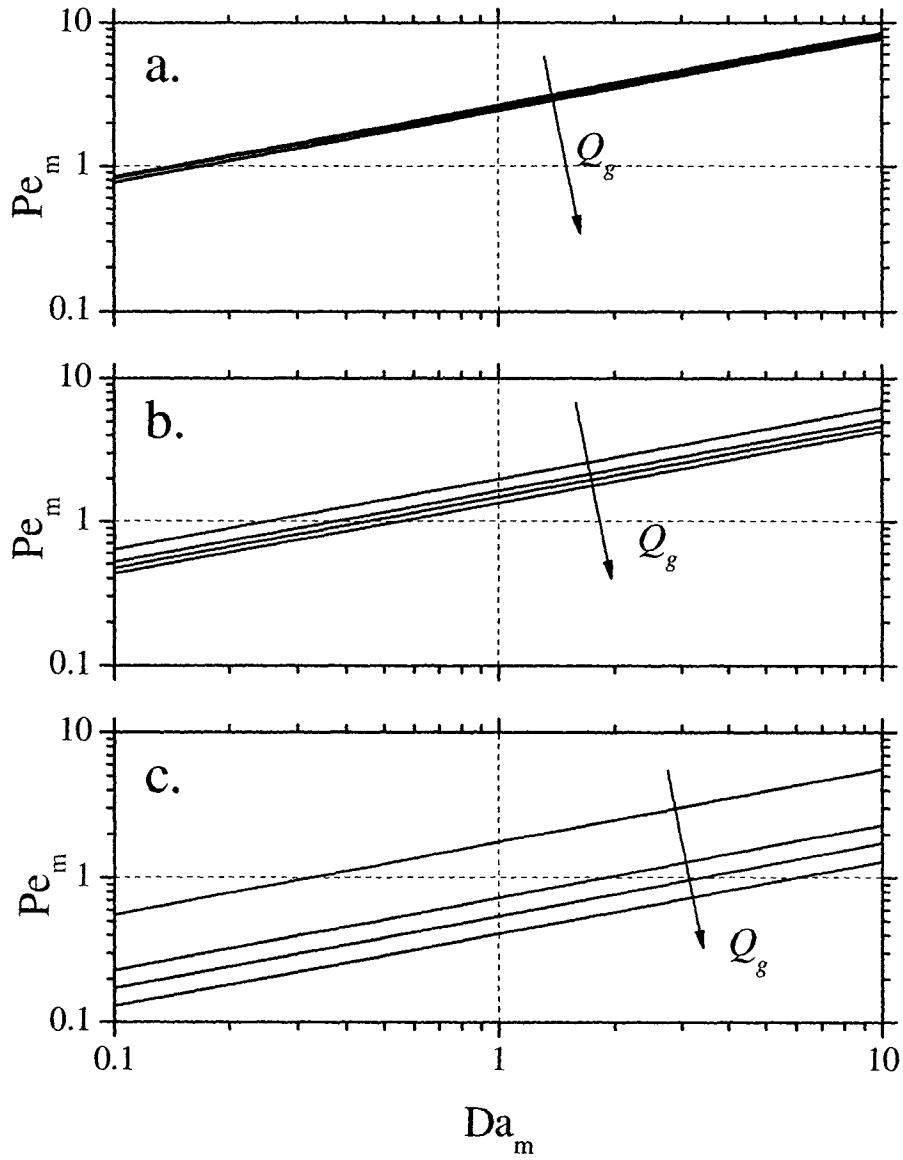

Figure 4–7 Lines of constant gas generation from decreasing to increasing rates in the direction of the arrow. Damkohler and corresponding Peclet numbers were calculated for Q_g = 0.007, 0.016, 0.022, and 0.03 $cm^3\ cm^{-2}\ min^{-1}$. Dimensionless numbers were calculated at three volumetric flowrates (a) 1.5 mL min^{-1}, (b) 0.5 mL min^{-1}, and (c) 0.1 mL min^{-1}.

CHAPTER V:

CONCLUSIONS AND RELEVANCE TO FUTURE WORK

The overarching goal of this research was to elucidate the underlying mechanisms of an electrochemical-based plume control technology utilizing mixed metal oxide coated titanium mesh electrodes (Ti/MMO) arranged in a permeable reactive barrier (PRB) format. The studies presented in this dissertation cover processes occurring over three different characteristic length scales. The results of those studies have established a foundation for analyzing reaction and transport mechanisms that directly impact how field implementations are designed and optimized.

5.1 Study Conclusions

The significant conclusions from each study are:

Chapter II:Impact of Electrode Surface Morphology on the Electrochemical Reduction Kinetics of Nitroaromatics and Heterocyclic Nitramines

Mixtures

- Reduction of the ring-nitro moieties on heterocyclic nitramines and nitroaromatics proceeds through an elctrocatalytic hydrogenation pathway.

- The electrocatalytic hydrogenation mechanism follows Eley-Rideal reaction kinetics over the range of initial concentration to surface area ratios investigated, indicating that inter-species competition for reaction sites is not an important process to consider.
- The large amount of cracks and fissures in the rough electrode surface leaves a majority of active sites unavailable to large organic species. Smoother aged electrode surfaces, although somewhat depleted in iridium content, expose a greater fraction of the active sites to the large organic molecules relative to a fresh Ti/MMO surface.

Chapter III: ***The influence of electrode geometry on the distribution of reaction conditions over a three-dimensional mesh electrode surface***

- The spatial distribution of transport and reaction process over the mesh electrode surface was dependent on the electrode geometry.
- The most important surface characteristic that controlled distribution is the fraction of surface area located in less accessible regions of the mesh, principally the tight corners of the mesh aperture.
- Flattening the front electrode surface to force a more uniform distribution of reaction and transport conditions increased the overall mass-flux reduction rate and would prevent localized degradation on the convex regions of the electrode surface.

- Under mass-transfer controlled reaction conditions, gas evolution enhances mass-transport to the electrode surface by establishing vertical velocity components within the electrode assembly.
- Dispersion (mixing) within the electrode assembly is a significant process at lower flowrate through the assembly.
- Contaminant mass-transport and mixing within the assembly are coupled through the gas evolution rate, resulting in a restricted range of operating conditions. The operating conditions are thus a function of the relative rates of mixing, convection, and reaction processes.
- The restricted conditions control which ideal reactor configuration is approached (CSTR or PFR) and ultimately the expected contaminant conversion though a series of reactors.

5.2 Implications to Full-Scale Systems

The objectives of the individual studies were focused on a particular aspect or process within the overall system. Taking advantage of the disparate length-scales that each study was conducted on, mechanisms that occur on a large length-scale control the distribution of small length-scale mechanisms over the system domain. To place this interpretation into a context that is relevant to a full-scale system, results from complementary laboratory and field studies were reinterpreted leveraging this

perspective. Where direct correlations between the laboratory and full-scale systems were not feasible, the implications were reasonably extrapolated from the consideration of the present study.

The sequence of electrodes that a contaminant is exposed to in flow-through systems is a pivotal design decision. In a carbonate-dominated groundwater system, where precipitation of carbonate solids is a concern at high pH, groundwater geochemistry is a major factor in this decision. The general perception is that to effectively degrade partially or fully oxidized organic contaminants, an reduction-oxidation sequence of conditions should be applied (Vogel et al., 1987). However, Gilbert and Sale (2005) observed more completed RDX degradation and faster TNT kinetics using an oxidation-reduction sequence of electrodes in flow-through electrolytic reactors compared to a reduction-oxidation sequence. Results of Chapter II directly support these findings and provide a fundamental explanation for the observations in the flow-through reactor experiments. Furthermore, this substantiates deploying the technology in an oxidation-reduction electrode sequence.

Electrode surface decomposition may be the most important factor in determining the viable lifetime of an electrolytic PRB. The eventual depletion of the electrocatalytic elements in the cathode surface coating would result in a relatively nonconductive surface. Nonconductive layers would cause the power density requirement to increase in order to maintain system performance at a desired level. Results from Chapters II and III suggests that surface evolution processes are likely concentrated on the convex upstream edges of the mesh surface. Although relatively short-term aging may enhance reaction rates, the surfaces of electrodes after extended service lives likely change in a way that

has a deleterious impact on degradation kinetics (Kodintsev and Trasatti, 1994). Cathodes recovered from an 18-mo field study in a chlorinated ethene contaminated aquifer (Ballaban, 2003) were iridium-depleted beyond the level measured in Chapter II. Concepts and models developed in this research will serve as useful tools for more pragmatic predictions and prevention of electrode decomposition.

Mixing and homogenization of non-uniform influent conditions as a function of gas-evolution and the large hydraulic conductivity in the electrode assembly have multiple implications on full-scale systems:

- CSTR-type behavior under the conditions described in Chapter IV requires a specific design strategy when combining multiple systems in series (Fogler, 1992).
- Reactant conversion in a CSTR system as a function of mixing quality will be limited relative to PFR system (Fogler, 1992).
- Redistributing the contaminant load from non-uniform upstream conditions alters the influent flux of reactants to the electrodes.
- Inducing upward fluid velocities implies that an important factor for scaling the system to full-scale implementations is the electrode height, a drastically different scaling-length than electrode assembly thickness in the direction of groundwater flow.

Some of the implications of this work to full-scale system design and deployment are questions that require further research to properly address. Their elucidation will

assist promoting the system towards full-scale use, and integration into the existing remediation technology toolset.

5.3 Path Forward

Projecting a constructive path forward encompasses both research needs directly related to system development, and aspects of more fundamental questions that are gaps in the current environmental technology knowledge base. By addressing these gaps, knowledge generated may be utilized by other niche technologies or applications. This may create a more synergistic climate for developing remediation solutions. To accomplish this effectively, research needs have been segregated into three categories; active substrates, deployment platform, and operating context (Figure 5-1).

Active substrates incorporate the physicochemical underpinnings of a given technology (e.g., catalyst or enzyme to promote a specific reaction or process). *Deployment platforms* entail how an active substrate is delivered to the problem (e.g., immobilized in a PRB or mobilized via injecting an oxidant). The environment in which an application is deployed is the *operating context* (e.g., site heterogeneity and capturing relevant performance metrics). A systems perspective of a technology may be synthesized as concepts from these three categories are merged at the point of implementation. A specific research question from each of these categories has been identified and described below. Each of these questions put forward the possibility to conduct high-impact, multidisciplinary research.

5.3.1 Active Substrate

Transition metal oxide coated electrodes have proven to be very effective cathodes for the reduction of organic contaminants. Certain attributes have made them suitable for in situ application; most notably their reasonably good stability under both anodic and cathodic polarization. As discussed previously, service lifetime is a critical property that determines the economic viability of utilizing these materials. Extending service lifetime should be a primary research thrust. Identifying the important mechanisms for metal oxide stability under a given set of conditions may be achieved via a "bottom-up" theoretical approach, or a "top-down" experimental approach. The "top-down" approach can be directed by identifying the relevant physical properties that lead to oxide stability while being cathodically polarized. Synergistic relationships may then be established for binary or multiple-component oxide mixtures. For example, non-cathodically-active metal oxides may be paired with more active species for the purposes of 1) non-active species provide an oxide-rich environment to enhance the metastability of active species (Burke and Naser, 2005), 2) non-active metal oxides may form a high surface area stable surface to immobilize the active species (Kodintsev and Trasatti, 1994), and 3) active metal oxide act as preferential centers of electron-transfer, preventing the non-active metal oxides from being reduced or degraded.

5.3.2 Deployment Platform

The deployment platform for the Ti/MMO active substrate in the present research was a mesh-electrode gas-evolving permeable reactive barrier. Rigorous scale-up methodologies for this platform need to be developed. Vertical transport in the electrode

assembly may be the important characteristic length to base a scaling methodology on. This dimension will likely be the most variable between implementations compared to the electrode assembly thickness. Velocity, bubble void fraction, and current density distributions in vertical gas-evolving cells have been experimentally (Elsner and Coeuret, 1985; Shah and Jorne, 1989) and mathematically (Dahlkild, 2001; Mat and Aldas, 2005; Philippe et al., 2005) characterized. These studies were conducted using closed boundary conditions (i.e., batch reactor). The relatively open boundaries of the electrode assembly in an electrolytic PRB represent a paradigm shift in the spatial domain considered in these characterization studies, which is further complicated when overlaying convective transport through the system.

Extending this theme, as was hypothesized in Chapter III new formats or configurations for deployment platforms of active substrates may have a large impact on overall process performance. Research directed at format (i.e., geometry, active substrate immobilization chemistry, etc.) and configuration (i.e., flow orientation, granular versus monolithic support, etc.) for immobilized substrate platforms (e.g., (Shimotori et al., 2006)), and specificity of mobilized substrates (e.g., (Saleh et al., 2007)) are beginning to gain attention. The ability to interchange active substrate with different deployment platforms rapidly expands the toolset available to remediation decision makers.

5.3.3 Operating Context

Characteristics of contaminated sites can impose a distinct set of conditions on a system during a remediation implementation. Temporal and spatial variations are normally present in groundwater flow, geochemistry, and contaminant flux. These

variations have the potential to be detrimental to system performance by exceeding the design criteria or depriving a biotic system from required substrates. Research into implementation methods and tools to alleviate the impacts of environmental variations, using electrolytic PRBs as the model technology, can be performed following multiple pathways. For example, reactor control schemes may be integrated into electrolytic-based implementations to handle transient influent conditions. Electrode cell potential is a clear choice for the manipulated variable in a prototypical control loop. However, the choice for measured and control variables are much less clear, both in terms of which variables are the best indicators for performance, and what is the proper method or tool to measure the process variables. Developing real-time, in situ sensors is an ongoing research topic (Campbell et al., 2006). Integration of these technologies into an overall implementation strategy presents a unique opportunity to deconvolute and process the complexity of contaminated groundwater systems.

5.4 References

Ballaban, M.N., 2003. Electrolytic Reactors (e-barrier) for In Situ Treatment of Chlorinated Compounds in Groundwater: Borden Field Experiment. University of Waterloo. MSc In Earth Sciences. Waterloo, Ont., Canada.

Burke, L.D.,Naser, N.S., 2005. Metastability and electrocatalytic activity of ruthenium dioxide cathodes used in water electrolysis cells. Journal of Applied Electrochemistry 35, 931-938.

Campbell, D.W., Müller, C.,Reardon, K.F., 2006. Development of a fiber optic enzymatic biosensor for 1,2-dichloroethane. Biotechnology Letters 28, 883-887.

Dahlkild, A.A., 2001. Modelling the two-phase flow and current distribution along a vertical gas-evolving electrode. Journal of Fluid Mechanics 428, 249-272.

Elsner, C.,Coeuret, F., 1985. Potential distribution along gas evolving electrodes. Journal of Applied Electrochemistry 15, 567-574.

Fogler, H.S., 1992. Elements of Chemical Reaction Engineering. Prentice Hall PTR, Englewood Cliffs, NJ.

Gilbert, D.M.,Sale, T.C., 2005. Sequential electrolytic oxidation and reduction of aqueous phase energetic compounds. Environmental Science and Technology 39, 9270-9277.

Kodintsev, I.M.,Trasatti, S., 1994. Electrocatalysis of H_2 evolution on RuO_2 + IrO_2 mixed oxide electrodes. Electrochimica Acta 39, 1803-1808.

Mat, M.D.,Aldas, K., 2005. Application of a two-phase flow model for natural convection in an electrochemical cell. International Journal of Hydrogen Energy 30, 411-420.

Philippe, M., Jérôme, H., Sebastien, B.,Gérard, P., 2005. Modelling and calculation of the current density distribution evolution at vertical gas-evolving electrodes. Electrochimica Acta 51, 1140-1156.

Saleh, N., Sirk, K., Liu, Y., Phenrat, T., Dufour, B., Matyjaszewski, K., Tilton, R.D.,Lowry, G.V., 2007. Surface modifications enhance nanoiron transport and NAPL targeting in saturated porous media. Environmental Engineering Science 24, 45-57.

Shah, A.,Jorne, J., 1989. Mass transfer under bubble-induced convection in a vertical electrochemical cell. Journal of the Electrochemical Society 136.

Shimotori, T., Cussler, E.L.,Arnold, W.A., 2006. High-density polyethylene membrane containing Fe^0 as a contaminant barrier. Journal of Environmental Engineering 132, 803-809.

Vogel, T.M., Criddle, C.S.,McCarty, P.L., 1987. Transformations of halogenated aliphatic compounds. Environmental Science and Technology 21, 722-736.

Figures

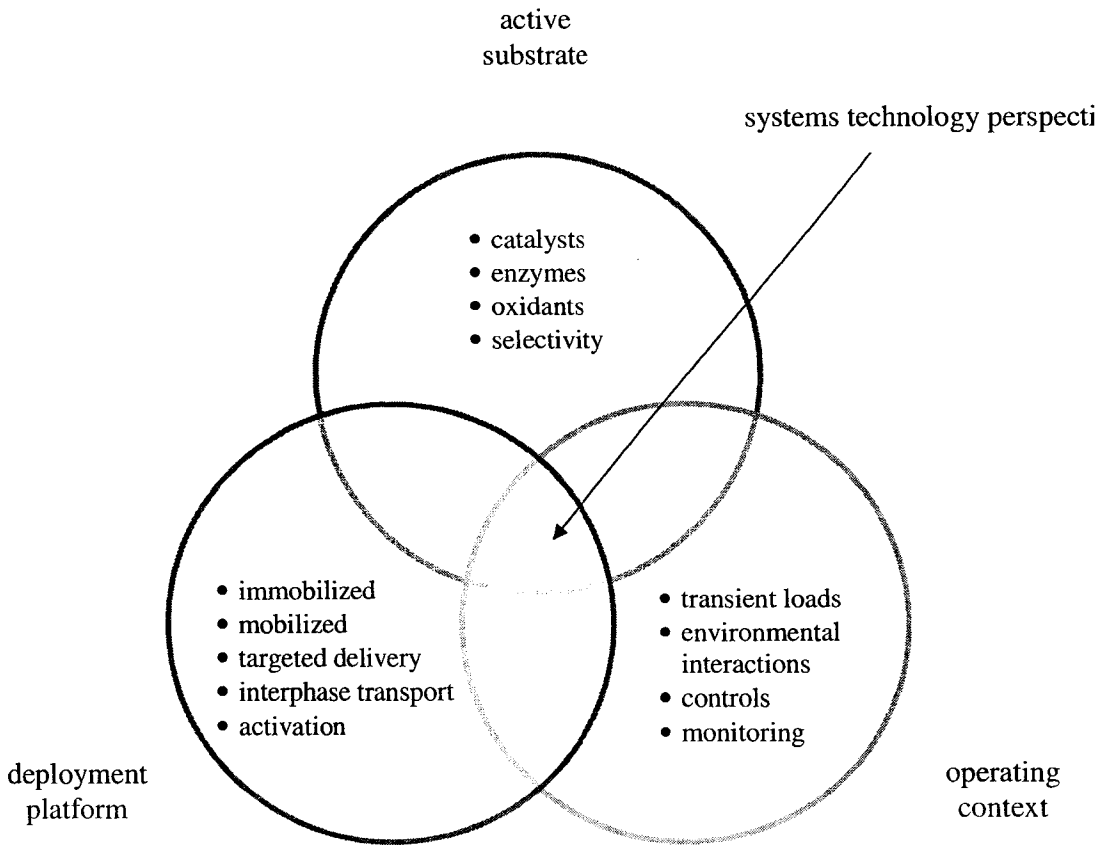

Figure 5-1 Architecture of the systems perspective for remediation technology development.

APPENDIX A

Supplement to Chapter II

A.1 Supplemental Figures

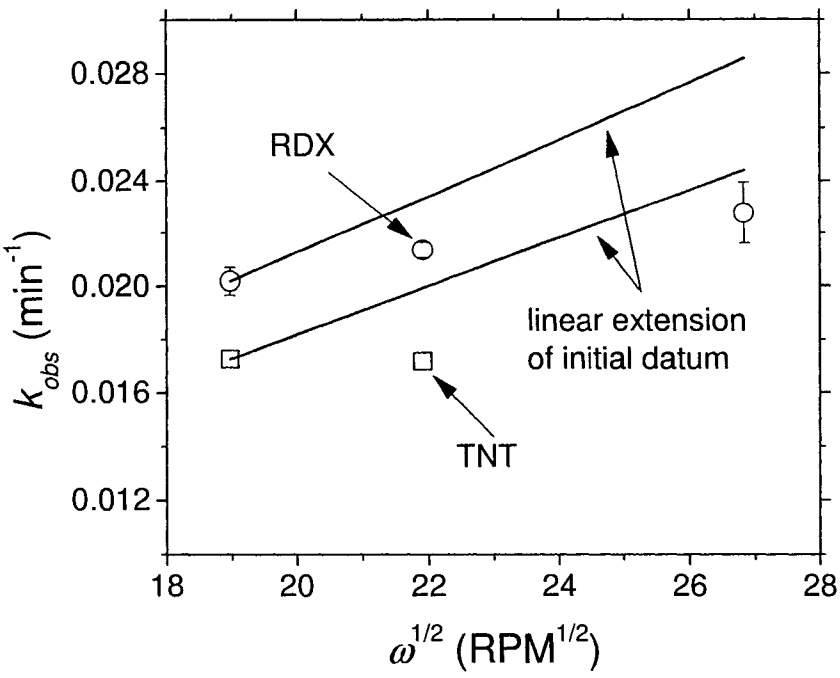

Figure A–1 Pseudo-first order rate constants as a function of the square root of the stir-bar rotation rate in the batch reactor. Solid lines extending from the first datum represent the expected relationship for a reaction constant controlled solely by mass-transfer to the electrode surface. Error bars represent ± one standard error of the rate constant estimation.

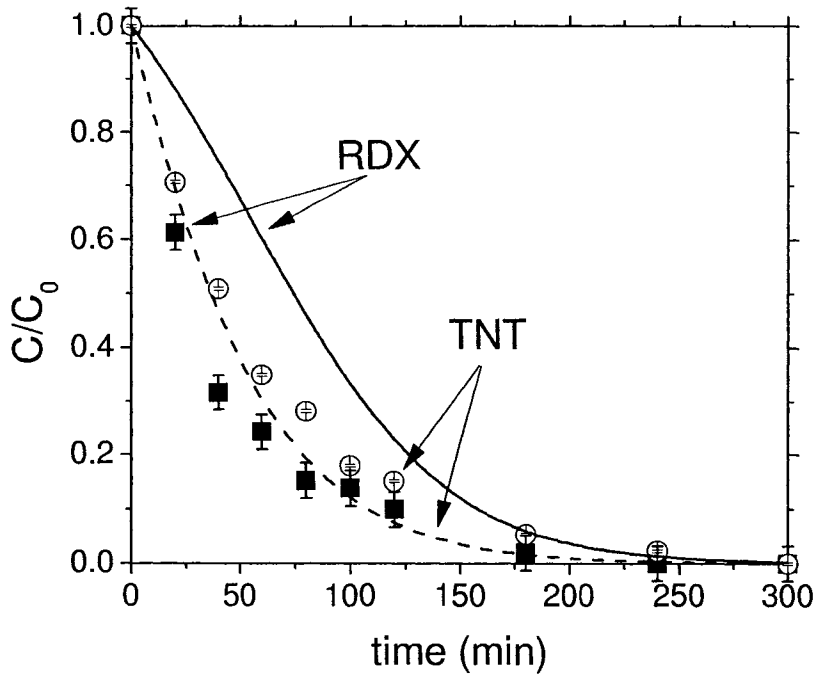

Figure A–2 Normalized concentrations of RDX and TNT in a combined degradation experiment operated at a constant cathode potential of -1100 mV and pH of 6.5. The initial concentrations of RDX and TNT were 1 and 40 μM. Error bars represent ± one standard deviation based on the analytical method calibration curve.

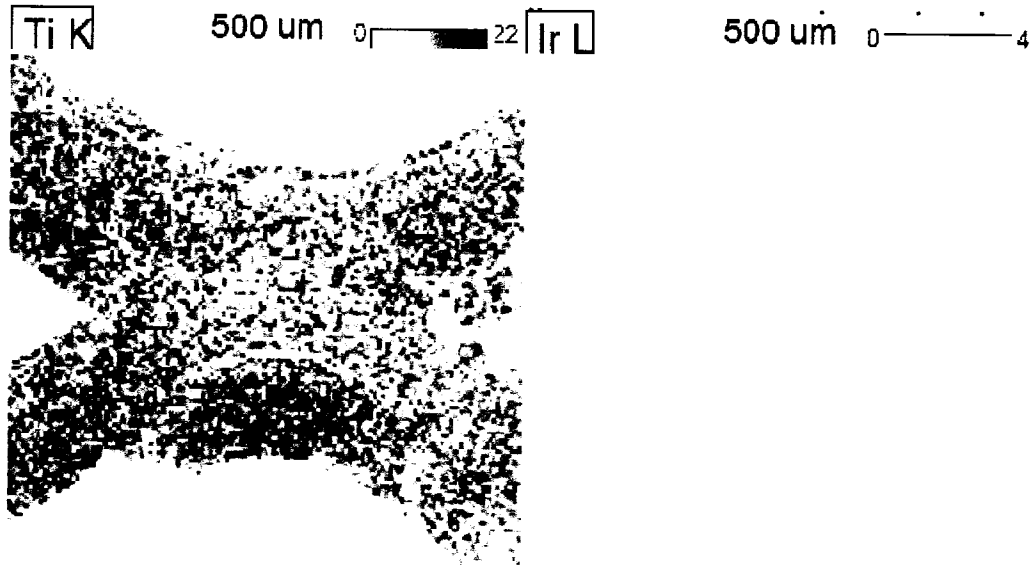

Figure A–3 EDS map of Ti and Ir peak intensity on the fresh electrode. Image magnification was 33X.

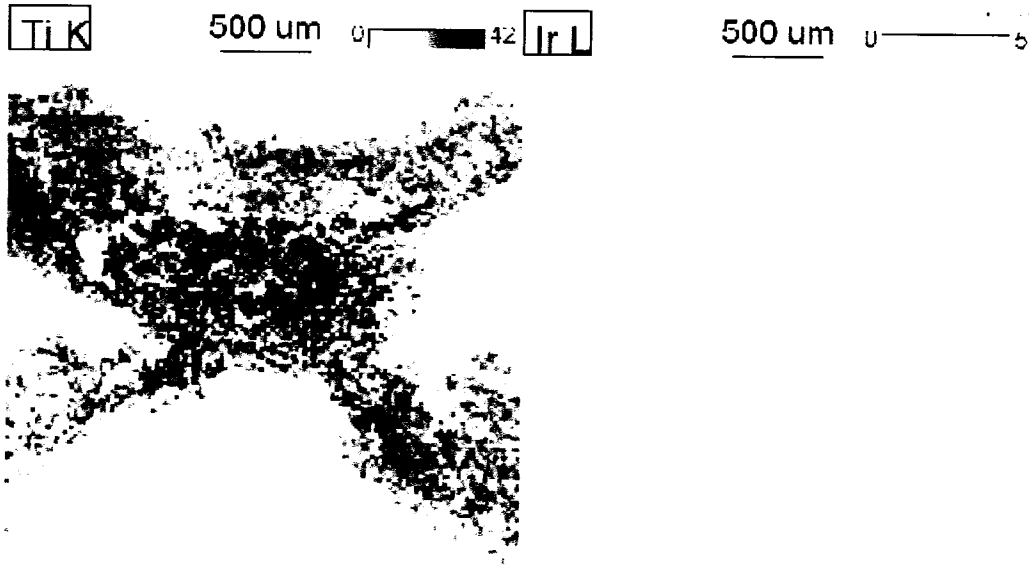

Figure A–4 EDS map of Ti and Ir peak intensity on the aged anode. Image magnification was 33X.

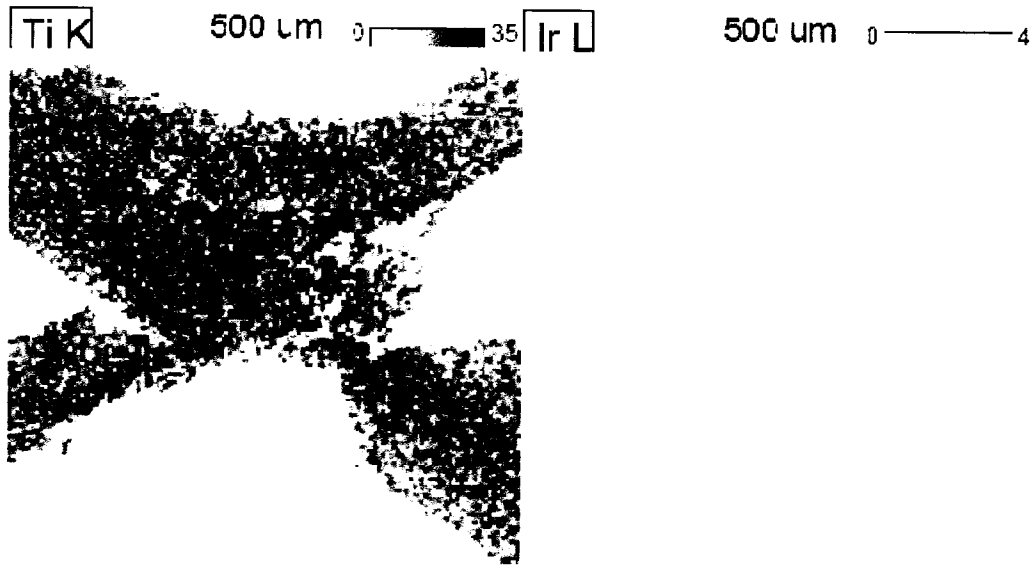

Figure A–5 EDS map of Ti ad Ir peak intensity on the aged cathode. Image magnification was 33X.

A.2 Analytical Calibration Curves

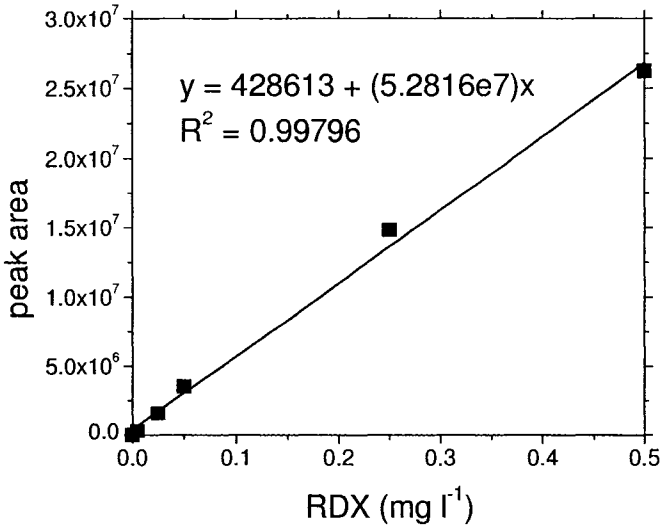

Figure A–6 Typical MS calibration curve for RDX.

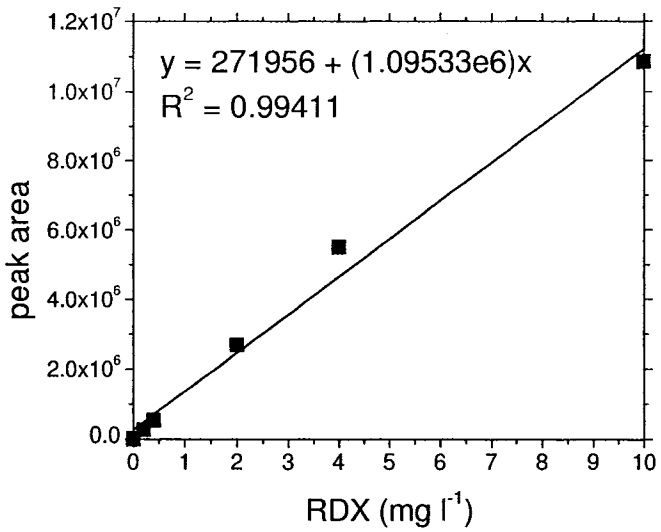

Figure A–7 Typical UV calibration curve for RDX.

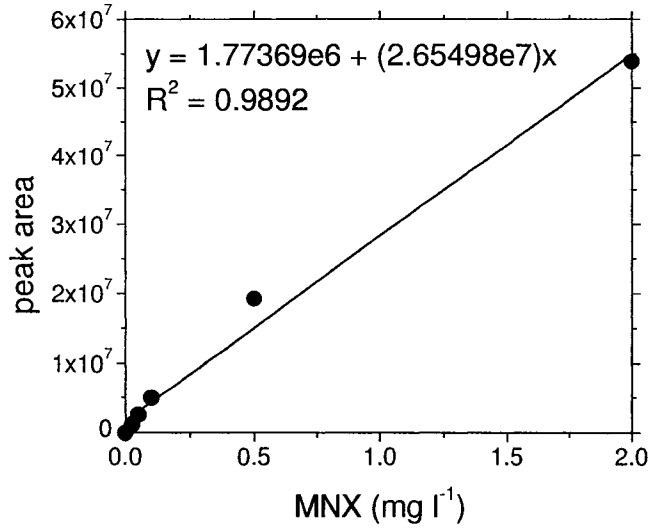

Figure A–8 Typical MS calibration curve for MNX.

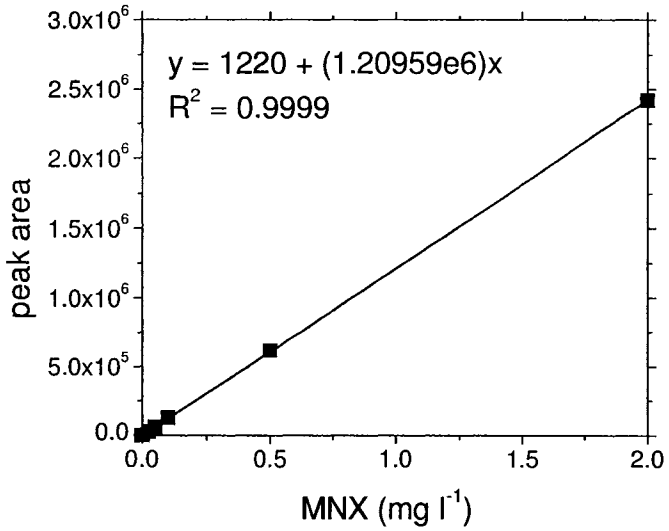

Figure A–9 Typical UV calibration curve for MNX.

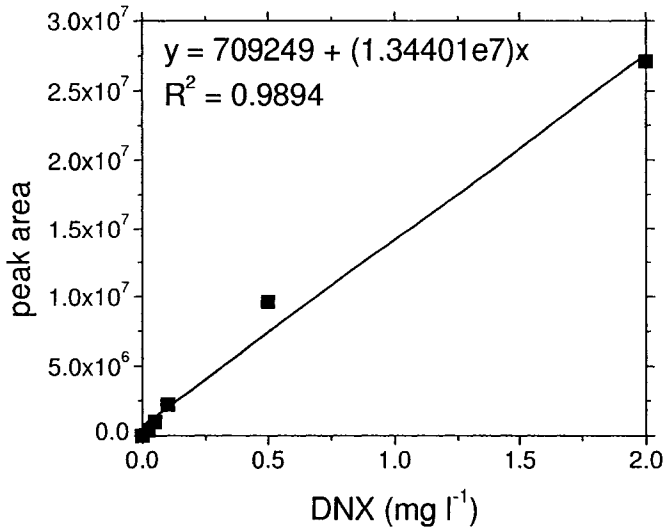

Figure A–10 Typical MS calibration curve for DNX.

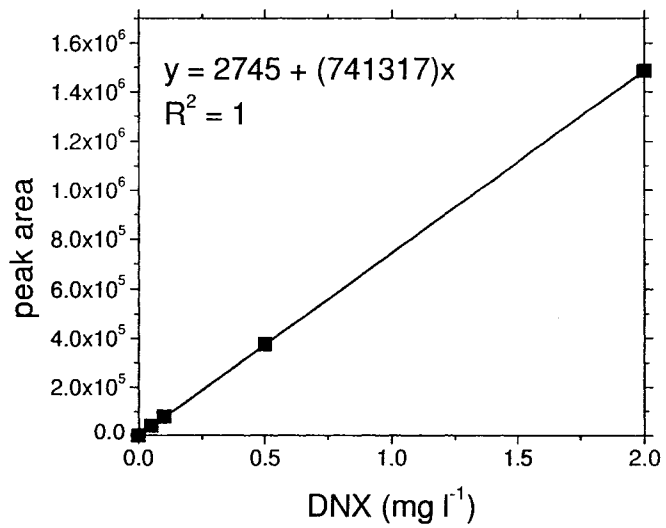

Figure A–11 Typical UV calibration curve for DNX.

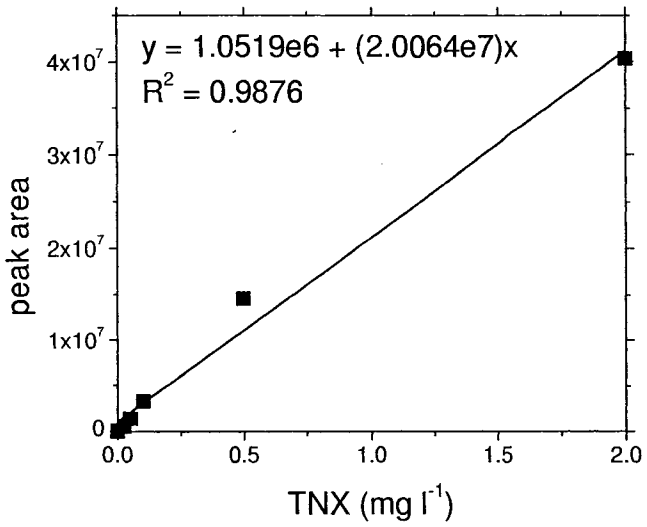

Figure A–12 Typical MS calibration curve for TNX.

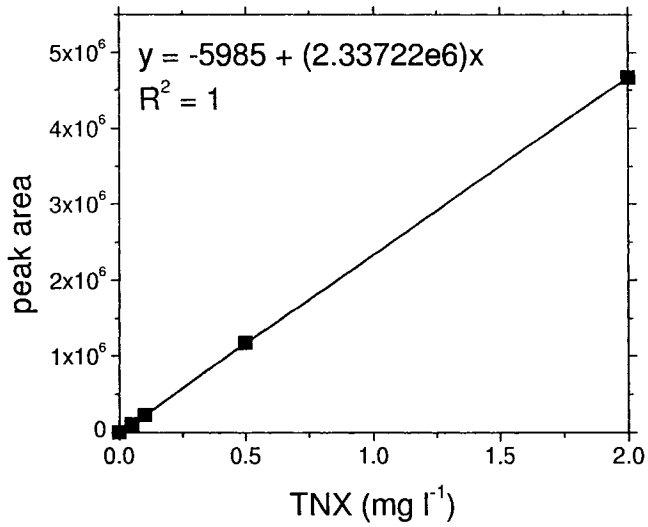

Figure A–13 Typical UV calibration curve for TNX.

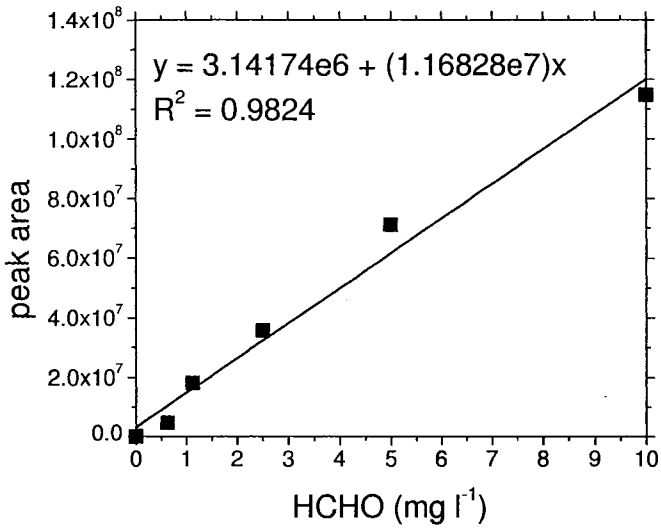

Figure A–14 Typical UV calibration curve for formaldehyde.

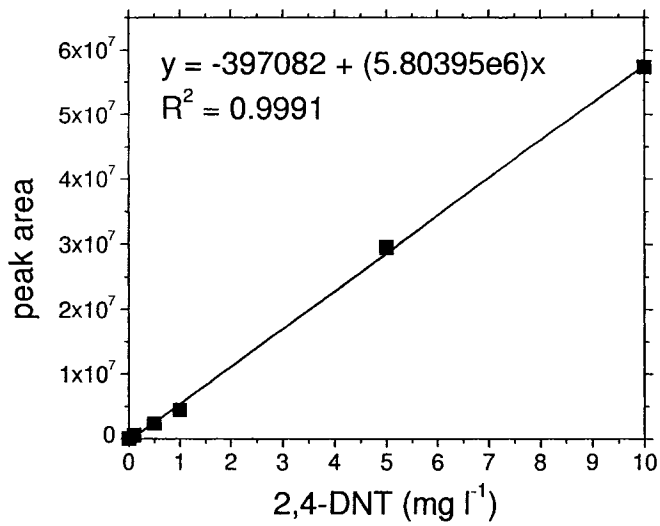

Figure A–15 Typical UV calibration curve for 2,4-DNT

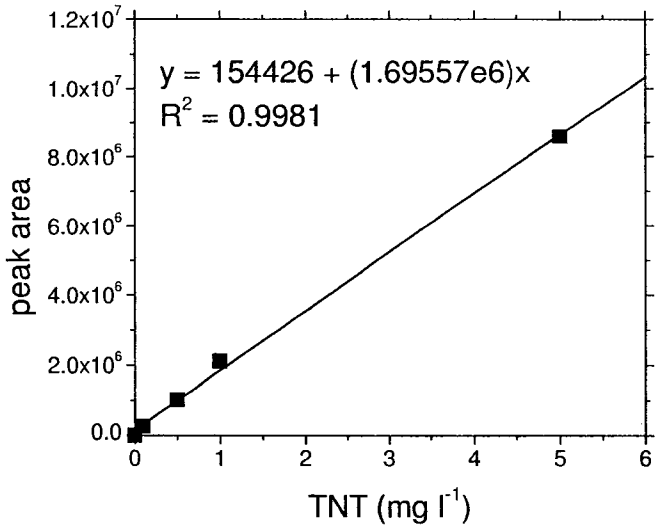

Figure A–16 Typical MS calibration curve for TNT.

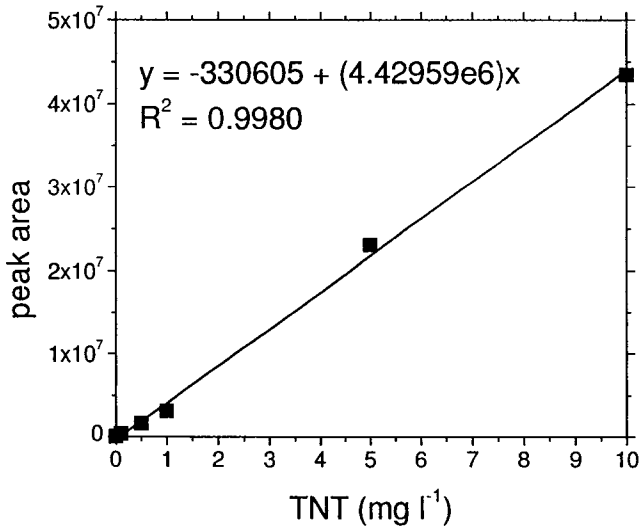

Figure A–17 Typical UV calibration curve for TNT.

A.3 Mechanistic Analysis of Reaction Kinetics

A.3.1 Langmuir-Hinshelwood Hougen-Watson

General rate law for multiple reactants (R1 and R2) undergoing rate-limiting electron transfer at a single surface reaction site (σ) to form multiple products (P1 and P2) via an adsorbed complex.

$$R1 + \sigma \leftrightarrow R1\sigma \quad \text{(A1)}$$

$$R2 + \sigma \leftrightarrow R2\sigma \quad \text{(A2)}$$

$$R1\sigma \xrightarrow{e^-} P1\sigma \quad \text{(A3)}$$

$$R2\sigma \xrightarrow{e^-} P2\sigma \quad \text{(A4)}$$

$$P1\sigma \leftrightarrow P1 + \sigma \quad \text{(A5)}$$

$$P2\sigma \leftrightarrow P2 + \sigma \quad \text{(A6)}$$

The adsorption and desorption isotherms may be described by a Langmuir isotherm. Rate constants may be assigned to the adsorption-desorption process of R1.

$$R1 + \sigma \underset{k_{d,R1}}{\overset{k_{a,R1}}{\leftrightarrow}} R1\sigma$$

At equilibrium, an equilibrium constant and rate law may be defined as:

$$K_{ads,R1} = \frac{k_{a,R1}}{k_{d,R1}} \quad \text{(A7)}$$

$$C_{R1} k_{a,R1} \Theta_v = k_{d,R1} \Theta_{R1} \quad \text{(A8)}$$

where C_{R1} is the concentration of R1, Θ_v is the vacant site fraction, and Θ_{R1} is the fraction of sites occupied by R1. Similar adsorption isotherms may be written for A2 when considering non-preferential adsorption to the arbitrary vacant site. In the case of

preferential adsorption, species-specific vacant sites would replace the arbitrary vacant site fraction in Equation A8. Following the same procedure desorption isotherms may be constructed based on Reactions A5 and A6.

The population balance for all sites may be used as a conservation equation

$$\Theta_v + \sum_i \Theta_i = 1 \qquad \text{(A9)}$$

for i species that form an adsorbed surface complex. Using A9 to eliminate Θ_v from A8, the Langmuir isotherm may be written as

$$\Theta_{R1} = C_{R1} \frac{K_{ads,R1}}{1 + K_{ads,R1} C_{R1}} \qquad \text{(A10)}$$

In the case of multiple species adsorbing to the same active site, the denominator of A10 is extended to include the impact of competition for the surface sites.

$$\Theta_{R1} = C_{R1} \frac{K_{ads,R1}}{1 + K_{ads,R1} C_{R1} + \sum_{i \neq R1} K_{ads,i} C_i} \qquad \text{(A11)}$$

For an irreversible electron transfer to R1 in Reaction A3, with a rate constant $k_{ET,A3}$ from the solid substrate to the adsorbed complex, the rate law may be written as

$$R_{A3} = k_{ET,A3} \Theta_{R1} \qquad \text{(A12)}$$

which may be further simplified by substituting for Θ_{R1} using A10.

$$R_{A3} = C_{R1} \frac{k_{ET,A3} K_{ads,R1}}{1 + K_{ads,R1} C_{R1}} \qquad \text{(A13)}$$

Following the development for A11, when multiple adsorbing species are present, A13 is further modified to account for site competition.

$$R_{A3} = C_{R1} \frac{k_{ET,A3} K_{ads,R1}}{1 + K_{ads,R1} C_{R1} + \sum_{i \neq R1} K_{ads,i} C_i} \quad \text{(A14)}$$

Examination of A14 shows that under the LHHW rate law assumptions, the reaction rate of a species is expected to be inhibited when in the presence of a additional reactants that compete for the same active surface site.

A.3.2 Eley-Rideal

General rate law for multiple reactants (R1 and R2) undergoing electron transfer at a single surface reaction site (σ) to form multiple products (P1 and P2) via an adsorbed mediator species (H).

$$H + \sigma \xleftrightarrow{e^-} H\sigma \quad \text{(A15)}$$

$$R1 + H\sigma \rightarrow P1 + H + \sigma \quad \text{(A16)}$$

$$R2 + H\sigma \rightarrow P2 + H + \sigma \quad \text{(A17)}$$

An adsorption isotherm for the mediator species may be derived following the development of A10.

$$\Theta_H = C_H \frac{K_{ads,H}}{1 + K_{ads,H} C_H} \quad \text{(A18)}$$

The irreversible rate law for R1 may be written as

$$R_{A16} = C_{R1} k_{A16} \Theta_H \quad \text{(A19)}$$

where k_{A16} is the rate constant for the irreversible reaction A16. Substituting for the mediator surface coverage fraction using A18, the rate law may be reformulated as

$$R_{A16} = C_{R1} k_{A16} \frac{C_H K_{ads,H}}{1 + C_H K_{ads,H}} \qquad \text{(A20)}$$

According to this mechanistic interpretation, the consumption rate of R1 is not dependent on the concentration of any other reactant. Therefore, for a constant mediator concentration, the resulting reaction kinetics resembles a first-order reaction system and rate inhibition is not expected when multiple reactants are present.

APPENDIX B

Supplement to Chapter III

B.1 Butler-Volmer Charge Transfer Reaction Kinetics

For an arbitrary electron transfer reaction from an oxidized species, O, to a reduced species, R

$$O + e^- \underset{k_b}{\overset{k_f}{\leftrightarrow}} R \ , \tag{B1}$$

the forward and backward rate constants, k_f and k_b, respectively, can be described by an Arrhenius equation.

$$k_f = A_f \exp\left(-\Delta G_{0f}^{\mp}/RT\right) \tag{B2}$$

$$k_b = A_b \exp\left(-\Delta G_{0b}^{\mp}/RT\right) \tag{B3}$$

The forward and backward rate constant is a function of the activation energy barrier for the reactant and product to proceed towards an activated complex ($\Delta G_{0f}^{\mp}$ and $\Delta G_{0b}^{\mp}$, respectively) at standard conditions. At equilibrium, the forward and backward reaction rates equate and the concentration of the species at the electrode surface are described by the Nernst equation

$$E = E^0 + \frac{RT}{nF}\ln\left(\frac{C_O^*}{C_R^*}\right), \tag{B4}$$

where C^* are the bulk concentrations of the reaction participants.

When the electrode potential is changed from the standard reduction potential (E^0) to a new potential (E), the activation barriers for the reactant and product in Reaction B1 are changed according to

$$\Delta G_f^{\mp} = \Delta G_{0f}^{\mp} - \left(-\alpha F\left(E - E^0\right)\right) \tag{B5}$$

$$\Delta G_b^{\mp} = \Delta G_{0b}^{\mp} - \left((1-\alpha)F\left(E - E^0\right)\right), \tag{B6}$$

where α is the transfer coefficient with a value between 0 and 1. Substituting these expressions for the activation energy into Equations B2 and B3 for the forward and backward rate constants are

$$k_f = A_f \exp\left(-\Delta G_f^{\mp}/RT\right) = A_f \exp\left(-\Delta G_{0f}^{\mp}/RT\right)\exp\left(-\alpha nF\left(E-E^0\right)/RT\right) \tag{B7}$$

$$k_b = A_b \exp\left(-\Delta G_b^{\mp}/RT\right) = A_b \exp\left(-\Delta G_{0b}^{\mp}/RT\right)\exp\left((1-\alpha)nF\left(E-E^0\right)/RT\right). \tag{B8}$$

This results in expression for the rate constants with a potential independent section (e.g., $A_f \exp\left(-\Delta G_{0f}^{\mp}/RT\right)$) and a potential dependent section (e.g., $\exp\left(-\alpha nF\left(E-E^0\right)/RT\right)$).

Considering the system at equilibrium where, according to Equation B4, $C_O^* = C_R^*$, the surface and bulk concentrations are equal, and the forward and backward reaction rates are equal, the forward and backward rate constants are also equal. This leads to the definition of the standard rate constant (k_0) for the reaction system.

$$\begin{aligned} R_f &= R_b \\ k_f C_O^* &= k_b C_R^* \\ k_f &= k_b = k_0 \end{aligned} \tag{B9}$$

The standard rate constant incorporates the activation barrier to electron transfer at standard conditions (i.e., temperature, pressure, potential).

$$k_0 = A_f \exp\left(-\Delta G_{0f}^{\mp}/RT\right) = A_b \exp\left(-\Delta G_{0b}^{\mp}/RT\right) \tag{B10}$$

Combining the forward and backward reaction rates leads to the overall reaction rate expression.

$$R = \frac{i}{nFA} = k_0\left[C_O^{surf}\exp\left(\frac{-\alpha nF}{RT}\left(E-E^0\right)\right) - C_R^{surf}\exp\left(\frac{(1-\alpha)nF}{RT}\left(E-E^0\right)\right)\right] \tag{B11}$$

At equilibrium where the current is equal to 0, the bulk and surface concentrations are equal. However, the potential (E_{eq}) is not necessarily equal to the standard reduction potential. The forward and backward reaction rate under this condition is the exchange current.

$$i_0 = nFAk_0C_O^* \exp\left(\frac{-\alpha nF}{RT}\left(E_{eq} - E^0\right)\right) = nFAk_0C_R^* \exp\left(\frac{(1-\alpha)nF}{RT}\left(E_{eq} - E^0\right)\right) \quad \text{(B12)}$$

Equation B12 may be simplified using Equation B4 to the -α power to eliminate the exponential term

$$i_0 = nFAk_0C_O^{(1-\alpha)}C_R^{\alpha} \ . \quad \text{(B13)}$$

Substituting Equation B13 back into B11 leads to the Butler-Volmer current overpotential equation

$$i = i_0\left[\frac{C_O^{surf}}{C_O^*}\exp\left(\frac{-\alpha nF}{RT}\eta\right) - \frac{C_R^{surf}}{C_R^*}\exp\left(\frac{(1-\alpha)nF}{RT}\eta\right)\right], \quad \text{(B14)}$$

where the overpotential $\eta = E - E_{eq}$.

When E is close to E^0, the concentration of the reactants and products are approximately equal, which simplifies Equation B13 to

$$i_0 = nFAk_0C, \quad \text{(B15)}$$

where C is equal to the concentration of the reactant or product.

When the reaction is irreversible, the backwards reaction may be neglected. Taking into account B15 as an approximation for i_0, Equation B14 may be reduced to an expression for a potential dependent forward reaction rate.

$$R = \frac{i}{nFA} = C^{surf}k_0 \exp\left(\frac{-\alpha nF}{RT}\left(E - E_{eq}\right)\right) \quad \text{(B16)}$$

Experimental measurements of pseudo first-order rate constants may then be correlated to an electrode potential dependent reaction rate constant.

$$R = k_f C^{surf} = C^{surf} k_0 \exp\left(\frac{-\alpha n F}{RT}\left(E - E_{eq}\right)\right)$$
$$k_f = k_0 \exp\left(\frac{-\alpha n F}{RT}\left(E - E_{eq}\right)\right) \qquad \text{(B17)}$$

B.2 RDX Electron-Transfer Reaction Kinetic Model

Import raw data from RDX reduction experiment in a batch electrochemical reactor
time of each sample/measurement (min)

time :=

input array of cathode potential readings (mV vs. SHE). each column corresponds to a new applied cell potential (2, 3, 4, 5, & 10 V).

potential :=

input array of normalized RDX concentrations in the cathode chamber. each column corresponds to a new applied cell potential (2, 3, 4, 5, & 10 V).

concentration :=

Problem constants

$n := 2$ number of electrons transferred in the reaction

$F := 96485$ Faraday's constant ($C\ mol^{-1}$)

$R := 8.314$ Universal gas constant ($J\ mol^{-1}\ K^{-1}$)

$T := 293$ Absolute system temperature (K)

$$characteristicLength := \frac{1L}{8cm \cdot 8cm \cdot 2.5}$$ ratio of reactor volume to electrode surface area (cm)

$characteristicLength = 6.25\ cm$

Raw data presentation

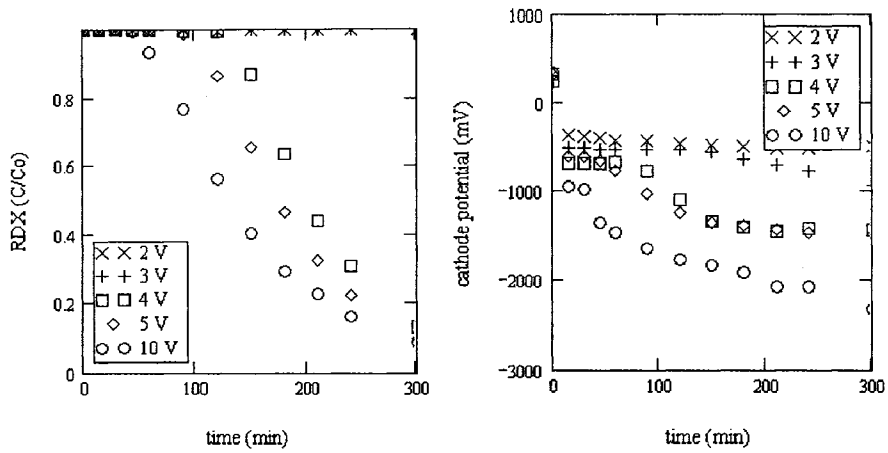

Analysis framework

Under the assumption of a strictly cathode potential depenent reduction rate of RDX, the following algorithm was used to characterize the results of these experiments into a single electron-transfer kinetic model (Butler-Volmer).

1. calculate the time series of first-order rate constants
2. correllate the first-order rate constants with the instantaneous cathode potential
3. perform multiple non-linear regression using the rate and potential as the inputs to calculate the Butler-Volmer kinetic parameters

The kObserved() Subroutine that calculates pseudo-first order rate constants over the duration of the constant cell potential bulk electrolysis experiments. Each rate constant is correllated with a particular time dependent electrode potential.

$$\begin{aligned}&\text{kObserved}(\text{timeSeries},\text{concSeries}) := \left|\begin{array}{l}\text{timeLength} \leftarrow \text{last}(\text{timeSeries})\\ \text{for } i \in 1..\text{timeLength}\\ \quad \left|\begin{array}{l} U_i \leftarrow \dfrac{\ln\left(\dfrac{\text{concSeries}_{i-1}}{\text{concSeries}_i}\right)}{\text{timeSeries}_i - \text{timeSeries}_{i-1}}\\ i \leftarrow i+1\end{array}\right.\\ \text{return } U\end{array}\right.\end{aligned}$$

The tafelModel() subroutine correllates the electrode potential and rate constant time series and calculates the Tafel parameters (k^0 and α) for each potential step - time interval. The input arrays are truncated based on the following criteria. First, the rate constant must be greater than zero. Second, the electrode potential must be larger in absolute magnitude than the standard potnetial of the reaction of interest. The output array has five elements (k^0 (characteristicLength/min),

α (unitless), relative standard deviation of k^0, relative standard deviation of α, and the R^2 coefficient for the fit to the truncated potential-rate constant data.

tafelModel(potentialSeries, kObsSeries, lengthFactor, standardPotential) :=

$j \leftarrow 0$

for $i \in 0..\text{last}(\text{kObsSeries})$

  if $\text{kObsSeries}_i > 0 \wedge \text{potentialSeries}_i < \text{standardPotenti}$

    $\text{kHolder}_j \leftarrow \text{kObsSeries}_i$

    $\text{pHolder}_j \leftarrow \text{potentialSeries}_i - \text{standardPotential}$

    $j \leftarrow j + 1$

  $i \leftarrow i + 1$

$X \leftarrow \text{pHolder}$

$Y \leftarrow \ln(\text{kHolder} \cdot \text{lengthFactor})$

$U \leftarrow \text{line}(X, Y)$

$W_0 \leftarrow \exp(U_0)$

$W_1 \leftarrow U_1 \cdot \left(\frac{-R \cdot T}{n \cdot F}\right) \cdot 1000$

$i \leftarrow 0..\text{last}(X)$

$\text{sumX} \leftarrow \sum_i X_i$

$\text{sumX2} \leftarrow \sum_i (X_i)^2$

$\text{avgX} \leftarrow \frac{\text{sumX}}{\text{length}(X)}$

$S_{xx} \leftarrow \text{sumX2} - \frac{\text{sumX}^2}{\text{length}(X)}$

$j \leftarrow 0..\text{last}(Y)$

$\text{sumDY} \leftarrow \sum_j \left[Y_j - (U_0 + U_1 \cdot X_j)\right]^2$

$s_y \leftarrow \sqrt{\frac{\text{sumDY}}{\text{length}(Y) - 2}}$

$W_2 \leftarrow \left| \frac{\sqrt{s_y} \cdot \sqrt{\frac{1}{\text{length}(X)} + \frac{\text{avgX}^2}{S_{xx}}}}{U_0} \right| \cdot 100$

$W_3 \leftarrow \left| \frac{\sqrt{s_y} \cdot \sqrt{\frac{1}{S_{xx}}}}{U_1} \right| \cdot 100$

$W_4 \leftarrow \text{corr}(X, Y)^2$

return W

Data analysis - extract the raw data for analysis

$E_{appl} = 10\ V$

$potential\_4 := submatrix(potential^{\langle 4 \rangle}, 0, 7, 0, 0)$ potential data

$concentration\_4 := submatrix(concentration^{\langle 4 \rangle}, 0, 7, 0, 0)$ concentration data

$time\_4 := submatrix(time, 0, 7, 0, 0)$ time data

$k_{10} := kObserved(time\_4, concentration\_4)$

$$constants_{10} := tafelModel\left(potential\_4, k_{10}, \frac{characteristicLength}{cm}, 0\right)$$

transient heterogenous rate constant

Butler-Volmer constants

$$k_{10} \cdot \frac{1}{min} \cdot characteristicLength = \begin{pmatrix} 0 \\ 0 \\ 0 \\ 2.187 \times 10^{-3} \\ 0.027 \\ 0.04 \\ 0.065 \\ 0.069 \end{pmatrix} \frac{cm}{min} \qquad constants_{10} = \begin{pmatrix} 1.54 \times 10^{-6} \\ 0.076 \\ 26.331 \\ 36.037 \\ 0.762 \end{pmatrix}$$

$E_{appl} = 5\ V$

$k_5 := kObserved(time, concentration^{\langle 3 \rangle})$

$$constants_5 := tafelModel\left(potential^{\langle 3 \rangle}, k_5, \frac{characteristicLength}{cm}, 0\right)$$

$k_5 \cdot \frac{1}{min} \cdot characteristicLength =$

	0
0	0
1	0
2	0
3	$1.917 \cdot 10^{-3}$
4	$-1.917 \cdot 10^{-3}$
5	$3.089 \cdot 10^{-3}$
6	0.028
7	0.057
8	0.072
9	0.076
10	0.08
11	0.083

$\frac{cm}{min}$

$$constants_5 = \begin{pmatrix} 3.966 \times 10^{-5} \\ 0.066 \\ 11.53 \\ 17.465 \\ 0.921 \end{pmatrix}$$

$E_{appl} = 4\ V$

$k_4 := kObserved(time, concentration^{\langle 2 \rangle})$

$$constants_4 := tafelModel\left(potential^{\langle 2 \rangle}, k_4, \frac{characteristicLength}{cm}, 0\right)$$

$k_4 \cdot \frac{1}{min} \cdot characteristicLength =$

	0
0	0
1	$8.28 \cdot 10^{-4}$
2	$4.464 \cdot 10^{-4}$
3	$-4.127 \cdot 10^{-5}$
4	$-1.233 \cdot 10^{-3}$
5	$1.197 \cdot 10^{-3}$
6	$4.589 \cdot 10^{-4}$
7	0.028
8	0.065
9	0.076
10	0.075
11	0.087

$\frac{cm}{min}$

$$constants_4 = \begin{pmatrix} 4.411 \times 10^{-6} \\ 0.083 \\ 10.338 \\ 16.292 \\ 0.837 \end{pmatrix}$$

Summary

E_{appl} (V)	k^0 (cm/min)	alpha	% std dev k^0	%std dev a	R^2	
10	1.54E-06	0.08	26.3	36.0	0.76	
5	3.97E-05	0.07	11.5	17.5	0.92	
4	4.41E-06	0.08	10.3	16.3	0.84	

$\left(\text{constants}_{10}{}^{T} \quad \text{constants}_{5}{}^{T} \quad \text{constants}_{4}{}^{T}\right)$

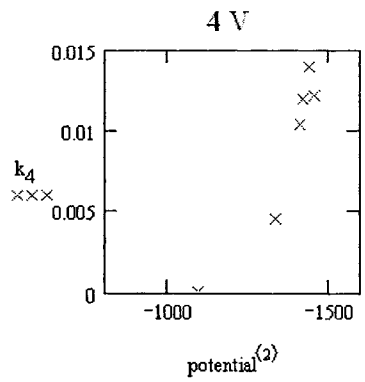

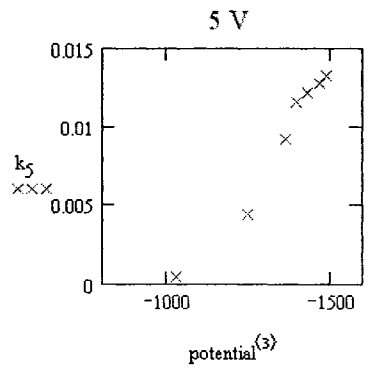

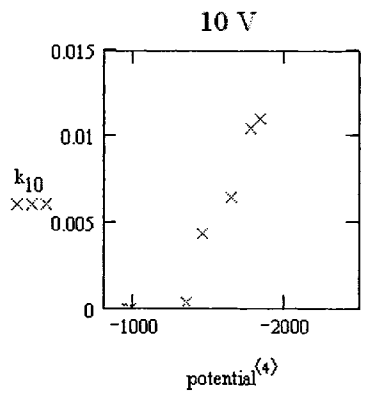

B.3 Supplemental Figures

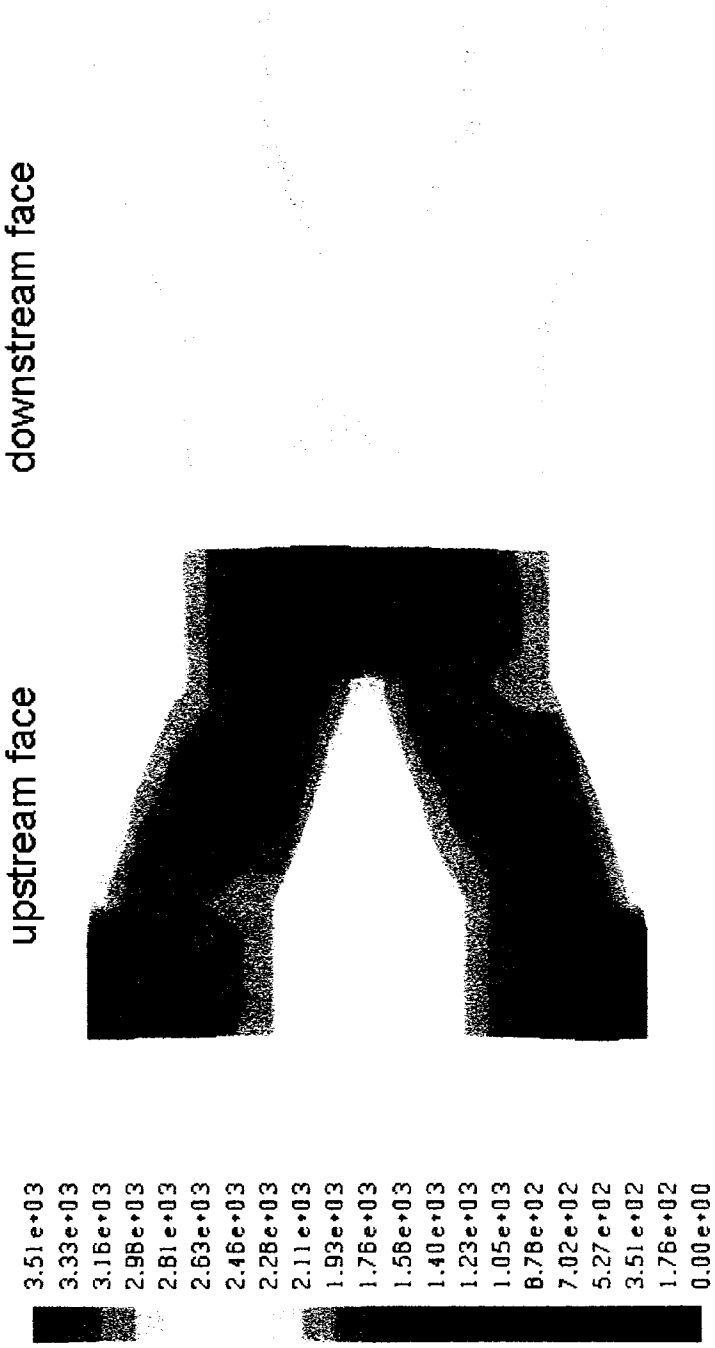

Figure B–1 Contours of current density (mA m^{-2}) on the downstream and upstream cathode surface.

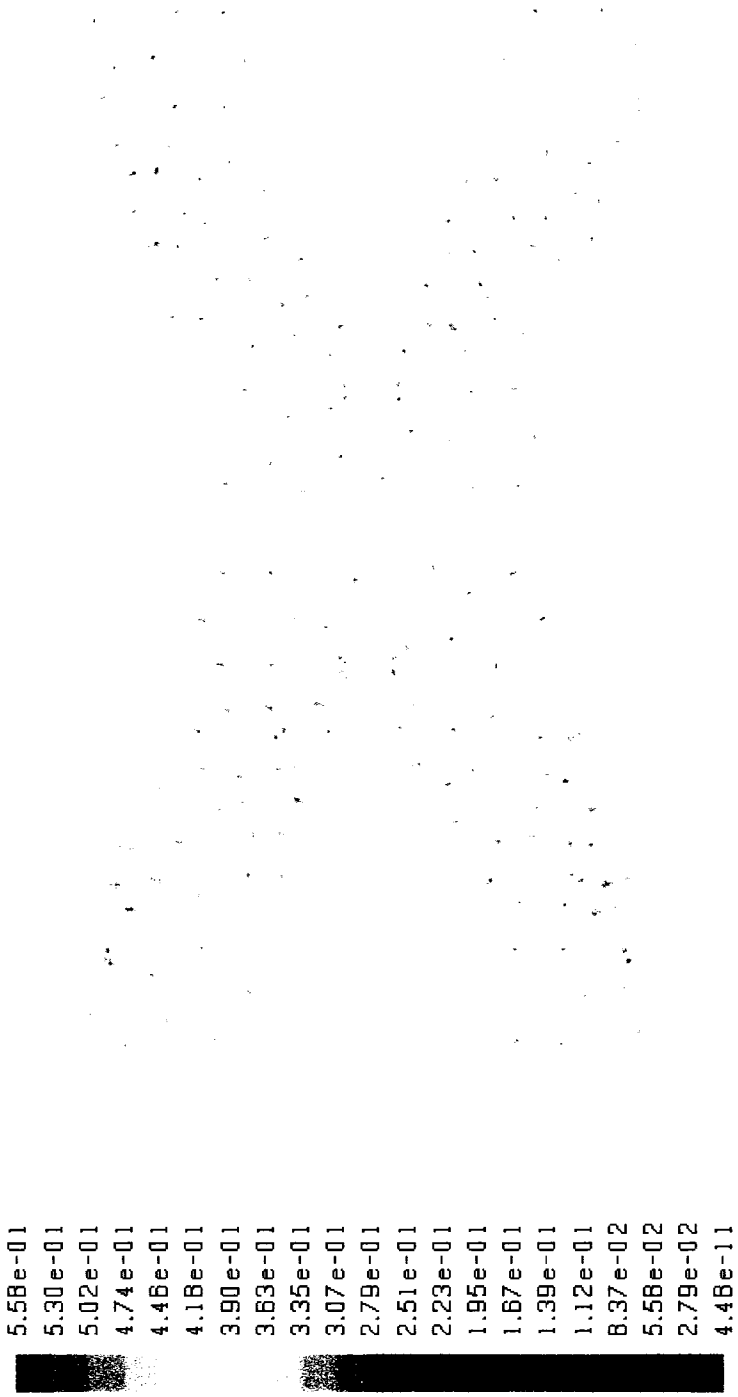

Figure B–2 Vectors of RDX diffusion flux (kgmol m^{-2} s^{-1}) at the downstream and upstream cathode surfaces of the flat electrode. Vector size directly correlates to flux magnitude.

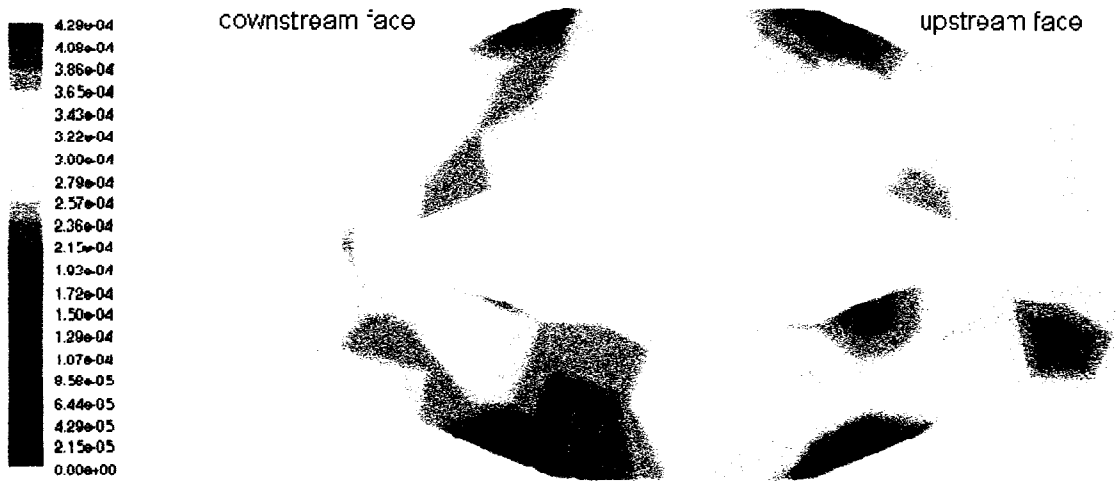

Figure B–3 Contours of Da_{mod} (A.U.) over the front and back cathode surface of the flat geometry electrode.

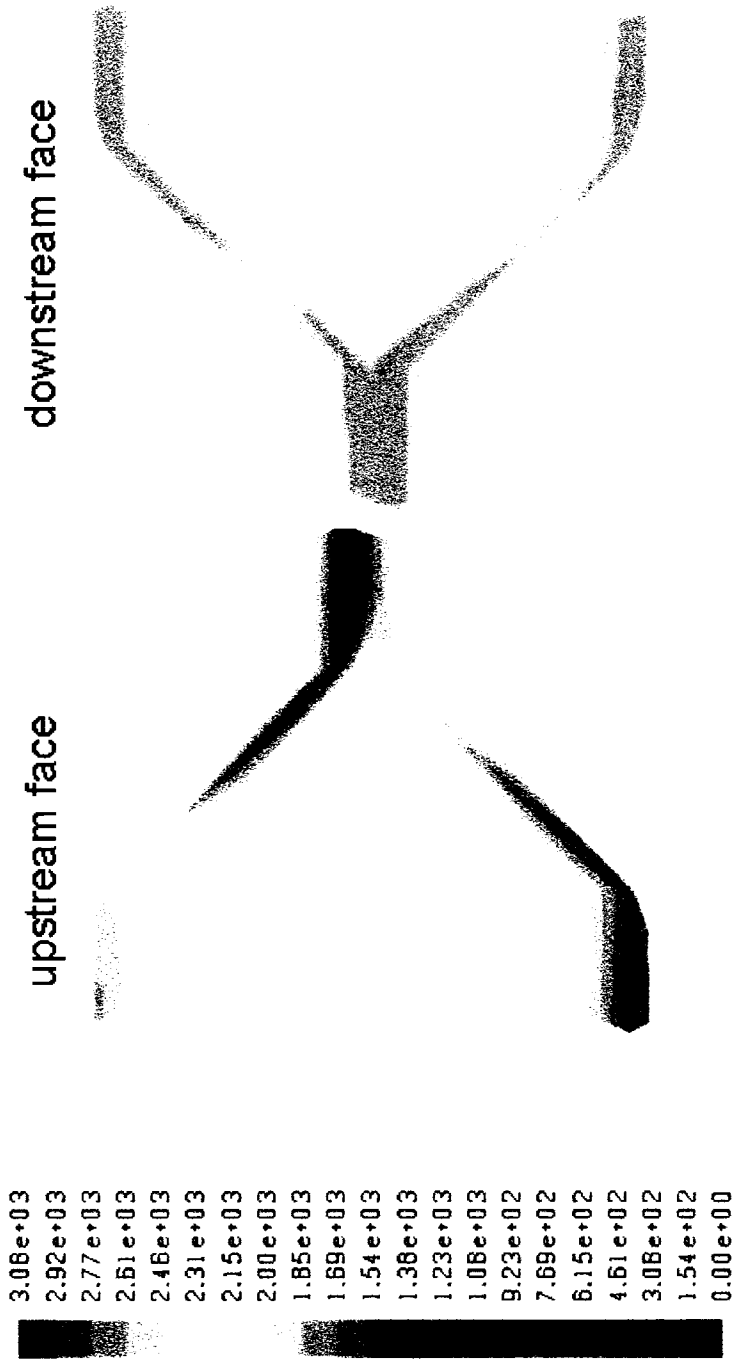

Figure B–4 Contours of current density (mA m^{-2}) over the front and back faces of the flat geometry cathode surface.

Figure B–5 Vectors of RDX diffusion flux (kgmol m^{-2} s^{-1}) at the upstream and downstream faces of the flat geometry cathode surface. Vector length directly corresponds to flux magnitude.

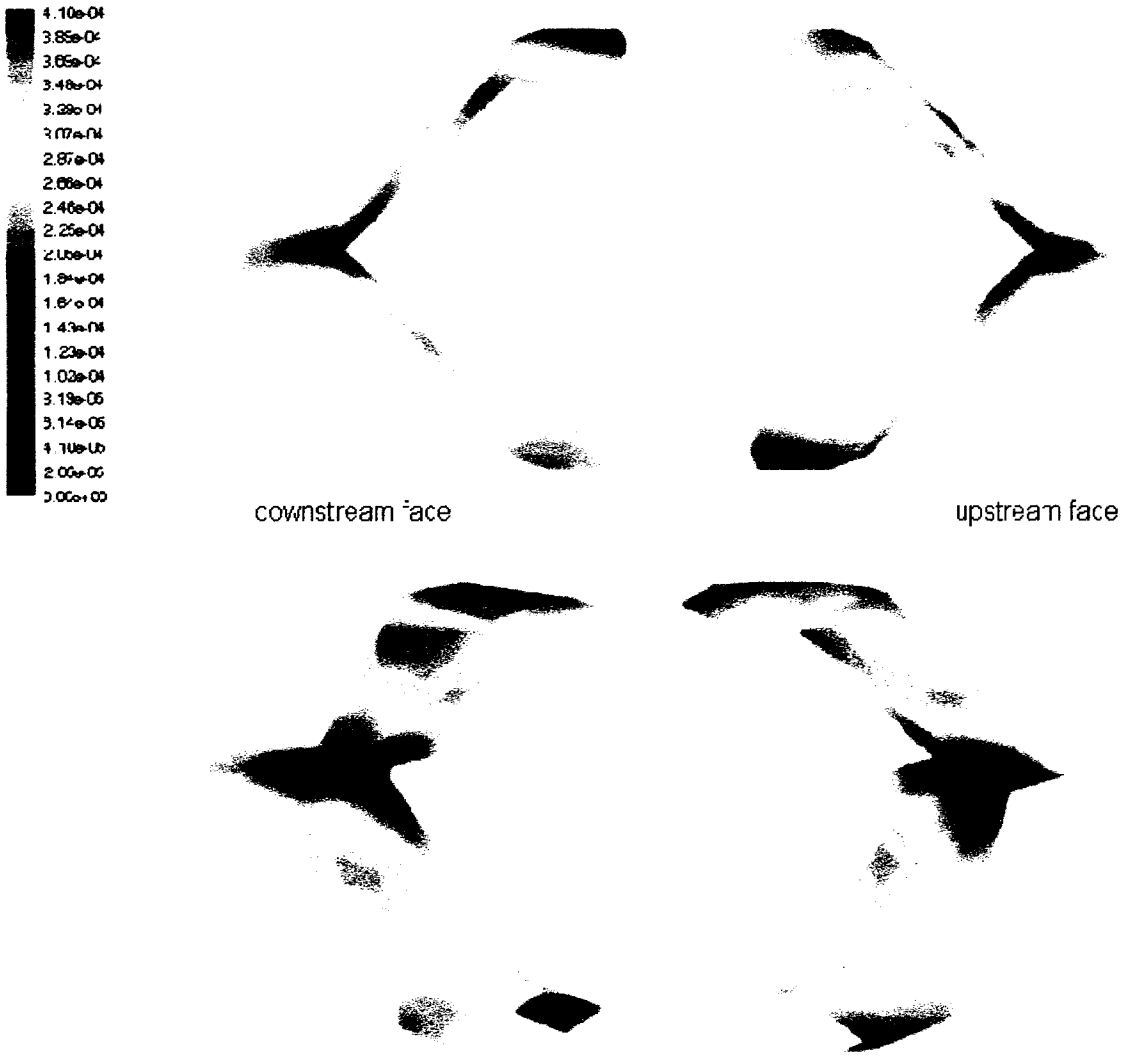

Figure B–6 Contours of Da_{mod} (A.U.) over the front and back cathode surface of the sharp geometry electrode from two different views.

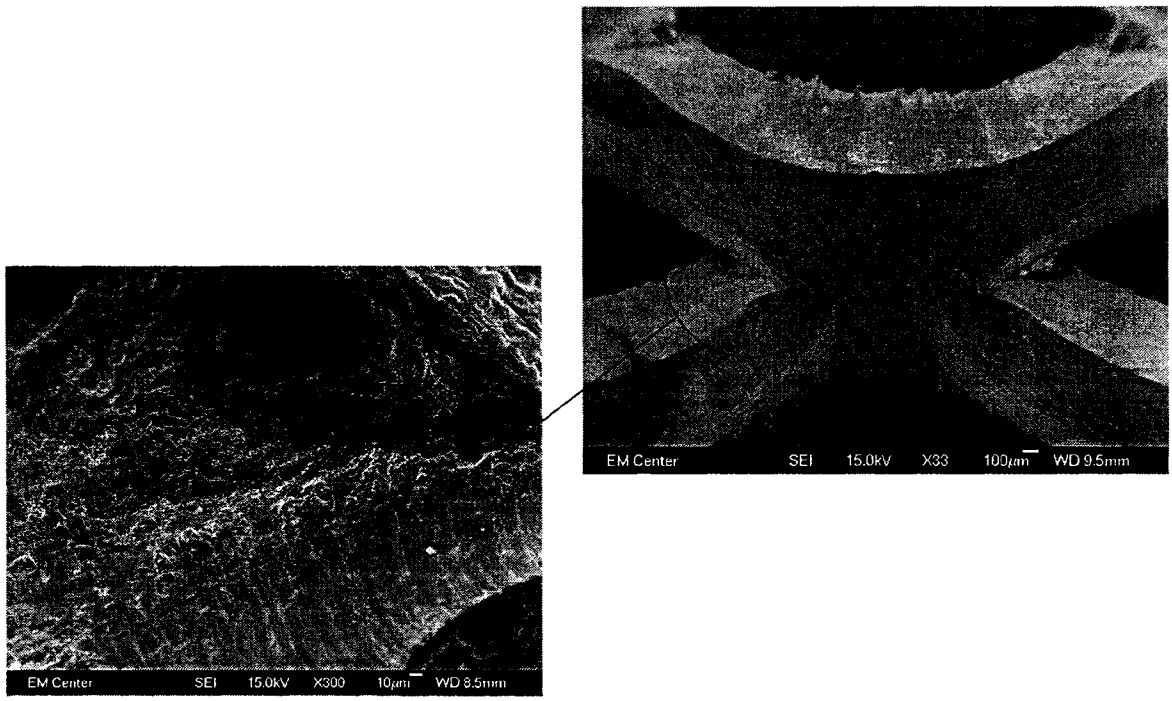

Figure B–7 SEM images of cathode aged by water electrolysis in a $NaClO_4$ electrolyte. The dotted line demarcates a transition from a fresh "cracked-mud" rough morphology to a smooth aged morphology. The transition is indicative of higher current densities in the smooth region over the aging process.

APPENDIX C

Supplement to Chapter IV

C.1 Supplemental Figures

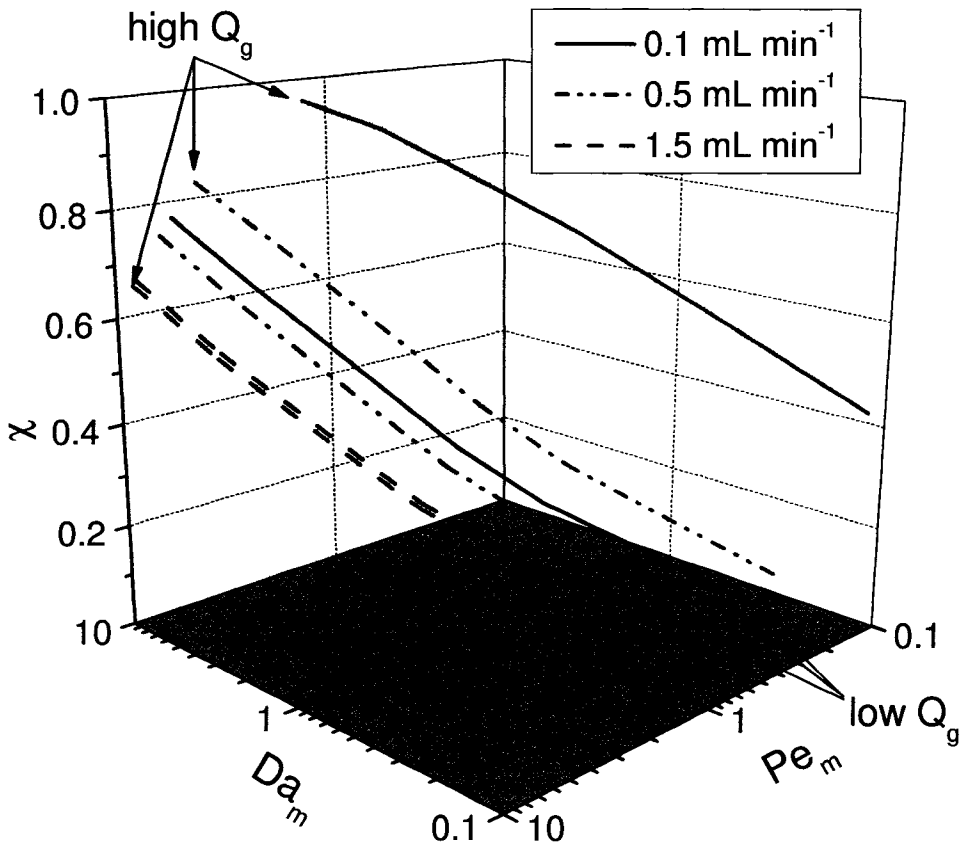

Figure C–1 Conversion as a function of Da_m and Pe_m along lines of constant gas generation at 0.007 (low Q_g) and 0.03 cm^3 cm^{-2} min^{-1} (high Q_g) for the three flowrates evaluated.

C.2 Analytical Calibration Curves

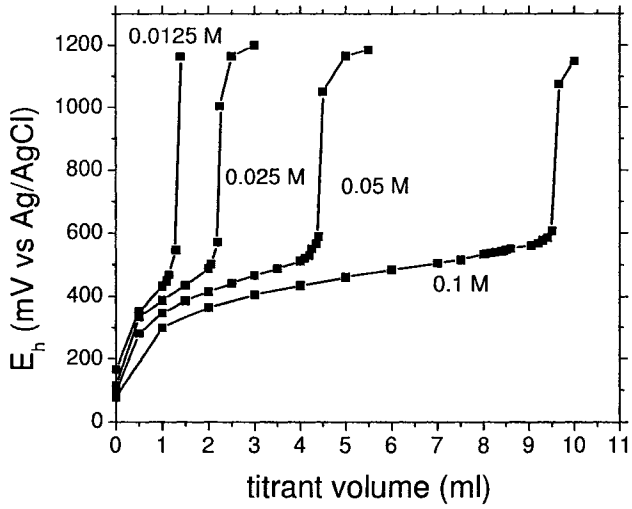

Figure C–2 Redox titration curves for four different concentrations of $K_4Fe(CN)_6$ using 0.1 M $Ce(SO_4)_2$. The titration endpoint was approimxately -700 mV vs Ag/AgCl, and coincided with a solution color change from light pink to reddish purple using N-phenylanthranilic acid as an indicator.

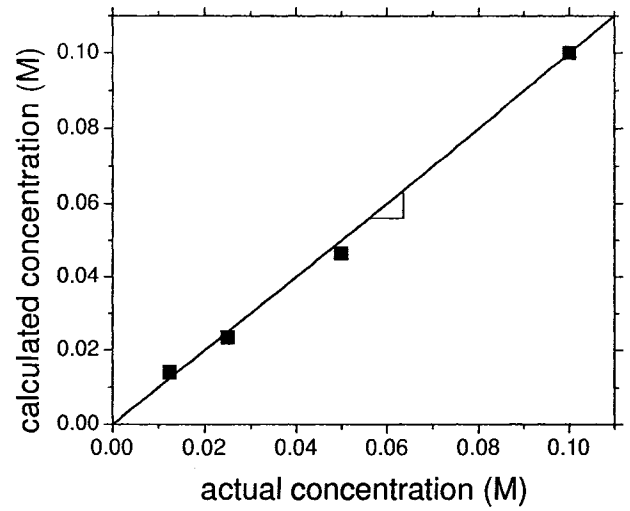

Figure C–3 Comparison of actual concentrations of $K_4Fe(CN)_6$ and calculated concentrations using the titrant volume at the titration endpoint.

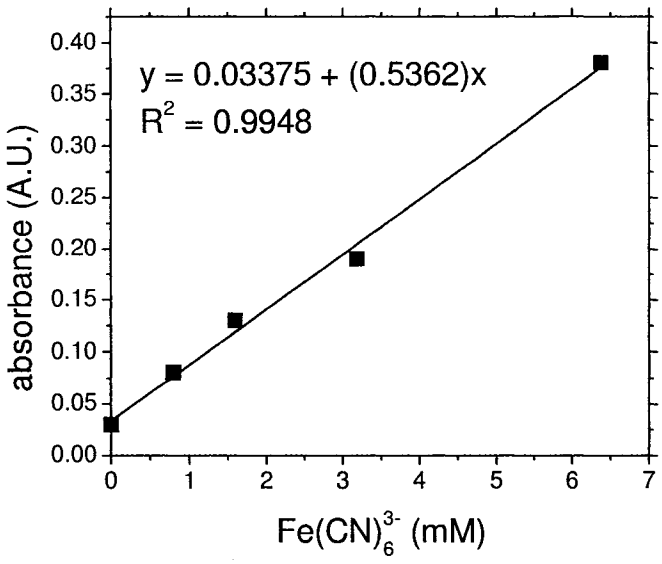

Figure C–4 Ferricyanide calibration curve at $\lambda = 470$ nm in a 0.1 M pH 7 phosphate buffer solution.

C.3 Example Breakthrough Curve Analysis

raw data

time (min) at end of sample

total reactant + product concentration of sample (mM)

time :=

	0
0	52
1	75
2	115
3	148
4	179
5	201
6	249
7	281
8	300
9	320
10	343
11	384
12	436
13	469
14	502

Conc :=

	0
0	-0.217
1	-0.217
2	0.163
3	0.349
4	0.063
5	0.343
6	0.129
7	0.516
8	1.189
9	1.382
10	2.055
11	2.355
12	3.208
13	3.975
14	3.615
15	4.461

Steady-state values (mM) to calculate conversion

$C_{product}$:=

	0
0	2.4
1	2.4
2	2.5

$C_{reactant}$:=

	0
0	2.354
1	2.261
2	2.261

problem constants

Faradays constant definition

$$faraday := 96484.6 \frac{coul}{mol}$$

length of test column (cm)

$$L := 20$$

applied current

$I_{import} :=$ 0.05

$$I := I_{import} A$$

flowrate

$Q_{import} :=$ 0.449

$$Q := Q_{import} \frac{mL}{min}$$

Subroutine to calculate the average and standard deviation of the steady-state reactor conversion.

$Conv :=$

$i \leftarrow 0$

$convsum \leftarrow 0$

$stndsum \leftarrow 0$

for $i \in 0..last(C_{product})$

$X_i \leftarrow \frac{C_{product_i}}{C_{reactant_i} + C_{product_i}}$

$convsum \leftarrow convsum + X_i$

$i \leftarrow i + 1$

$avg \leftarrow \frac{convsum}{length(C_{product})}$

for $i \in 0..last(C_{product})$

$Y_i \leftarrow (X_i - avg)^2$

$stndsum \leftarrow stndsum + Y_i$

$i \leftarrow i + 1$

$stddev \leftarrow \sqrt{\frac{stndsum}{length(C_{product}) - 1}}$

return $stack(avg, stddev)$

Influent concentration (mM)

$C_0 :=$

$i \leftarrow 0$

$total \leftarrow 0$

for $i \in 0..last(C_{product})$

$T_i \leftarrow C_{product_i} + C_{reactant_i}$

$total \leftarrow total + T_i$

$i \leftarrow i + 1$

return $\frac{total}{length(C_{product})}$

$C_0 = 4.7256$

$$Conv = \begin{pmatrix} 0.5149 \\ 0.0101 \end{pmatrix}$$

current efficiency calculation and standard deviation

$$\eta := \frac{C_0 \cdot \frac{mol}{1000liter} \cdot faraday \cdot Conv_0 \cdot Q}{I} \qquad v_\sigma := \left(C_0 \cdot \frac{mol}{1000liter} \cdot faraday \cdot \frac{Q}{I} \right)^2 \cdot (Conv_1)^2$$

$$\eta = 0.0351 \qquad \sqrt{v_\sigma} = 0.0007$$

Response function to a unit step input for a non-ideal PFR. In the function matrix. the first entry is the function, the second is the derivative with respect to the first fitting parameter (dispersion coefficient), and the third is the derivative with respect to the second fitting parameter (interstitial velocity). The guess array contains the inital guess for both parameters in units of $cm^2\ min^{-1}$ (dispersion coefficient) and $cm\ min^{-1}$ (interstitial velocity) respectively. This nonlinear regression package is based on the Levenberg-Marquardt method for minimization.

$$function(t, a) := \begin{bmatrix} \frac{C_0}{2} \cdot erfc\left(\frac{L - a_1 \cdot t}{\sqrt{4 \cdot a_0 \cdot t}} \right) \\ \frac{C_0}{4 \cdot \sqrt{\pi}} \cdot e^{\frac{-(L - a_1 \cdot t)^2}{4 a_0 \cdot t}} \cdot \frac{L - a_1 \cdot t}{(a_0 \cdot t)^{\frac{3}{2}}} \cdot t \\ \frac{1}{2} \cdot \frac{C_0}{\pi^{\frac{1}{2}}} \cdot e^{\frac{-1}{4} \cdot \frac{(L - a_1 \cdot t)^2}{a_0 \cdot t}} \cdot \frac{t}{(a_0 \cdot t)^{\frac{1}{2}}} \end{bmatrix} \qquad guess := \begin{pmatrix} 5 \cdot 10^{-3} \\ 0.046 \end{pmatrix}$$

Results of the least squares non-linear regression algorithm. The cg array contains the dispersion coefficient (first row in units of $cm^2\ min^{-1}$) and interstitial velocity (second row in units of $cm\ min^{-1}$).

$$cg := genfit(time, Conc, guess, function) \qquad cg = \begin{pmatrix} 0.0443 \\ 0.0533 \end{pmatrix}$$

The parameters calculated from the regression analysis were used in a plug-flow plus dispersion model. The regression model was compared to the experimental dataset, and residuals were calculated over the time (X) axis.

$$fit(t) := \frac{C_0}{2} \cdot erfc\left(\frac{L - cg_1 \cdot t}{\sqrt{4 \cdot cg_0 \cdot t}}\right)$$

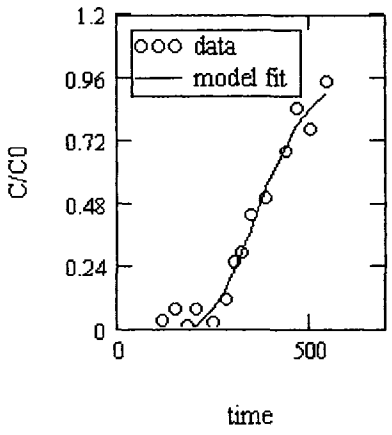

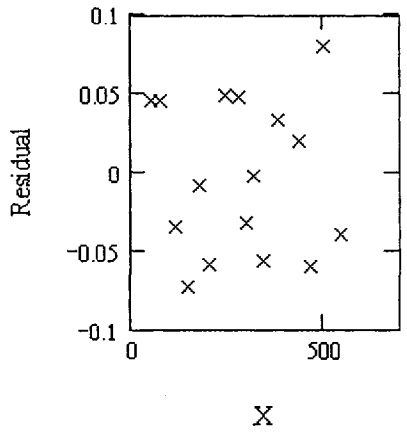

correlation coefficient

$$corr\left(\frac{\overrightarrow{fit(time)}}{C_0}, \frac{Conc}{C_0}\right) = 0.9895$$

Variability Analysis mean square error

$$MSE := \frac{\sum\left(Conc - \overrightarrow{fit(time)}\right)^2}{length(time) - 2}$$

MSE = 0.0581

matrix to calculate variance in the dispersion coefficient and interstitial velocity from the Levenburg-Marquardt method.

$$
\begin{aligned}
D := \;& i \leftarrow 0 \\
& U \leftarrow 0 \\
& \text{for } i \in 0..\text{last}(Conc) \\
& \quad U_{i,0} \leftarrow \frac{C_0}{4\cdot\sqrt{\pi}} \cdot e^{\frac{-(L-cg_1\cdot time_i)^2}{4cg_0\cdot time_i}} \cdot \frac{L - cg_1\cdot time_i}{(cg_0\cdot time_i)^{\frac{3}{2}}} \cdot time_i \\
& \quad U_{i,1} \leftarrow \frac{1}{2}\cdot\frac{C_0}{\pi^{\frac{1}{2}}} \cdot e^{\frac{-1}{4}\cdot\frac{(L-cg_1\cdot time_i)^2}{cg_0\cdot time_i}} \cdot \frac{time_i}{(cg_0\cdot time_i)^{\frac{1}{2}}} \\
& \quad i \leftarrow i + 1 \\
& \text{return } U
\end{aligned}
$$

$var := MSE\cdot(D^T\cdot D)^{-1}$ variance of the two regression parameters

standard deviation of the dispersion coefficient ($cm^2\ min^{-1}$)

$stdev_{cg\_0} := \sqrt{var_{0,0}}$ $stdev_{cg\_0} = 0.0071$

standard deviation of the intersitial velocity ($cm\ min^{-1}$)

$stdev_{cg\_1} := \sqrt{var_{1,1}}$ $stdev_{cg\_1} = 0.0008$

RTD analysis

time (min) to reach $C/C_0 = 0.5$ and transformation to dimensionless time

$t_{0.5} := root\left[\left(\frac{fit(x)}{C_0} - 0.5\right), x, 100, 400\right]$ $t_{0.5} = 375.0782$ $\theta := \frac{time}{t_{0.5}}$

dispersion number as a quantification of the extent of mixing

$$N_{disp} := \frac{cg_0}{L \cdot cg_1} \qquad N_{disp} = 0.0415$$

F curve is the response to a step increase in tracer concentration

$$F(\theta) := 0.5 \cdot \mathrm{erfc}\left(0.5 \cdot N_{disp}^{-0.5} \cdot \frac{1-\theta}{\sqrt{\theta}}\right)$$

The E(θ) curve is the derivative of the F(θ) curve with respect to dimensionless time, and is the theoretical response to a ideal pulse input function

$$E(theta) := \frac{-1}{\sqrt{\pi}} \cdot e^{\frac{-0.25}{N_{disp}} \cdot \frac{(1-theta)^2}{theta}} \cdot \left(\frac{-0.5}{\sqrt{N_{disp} \cdot theta}} - \frac{0.25}{\sqrt{N_{disp}}} \cdot \frac{1-theta}{theta^{\frac{3}{2}}}\right)$$

$j := 0..\mathrm{length}(\theta) - 1$

Plot of E(θ) and F(θ) curves with respect to dimensionless time.

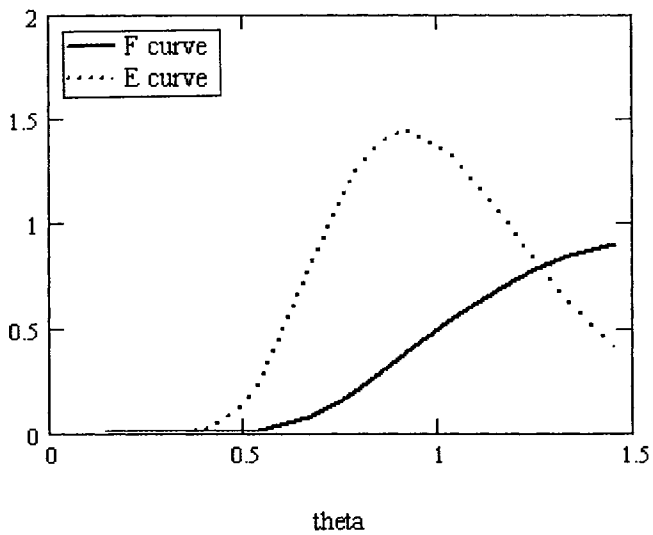

Acronyms

CFD	Computational Fluid Dynamics
CSTR	Continuously Stirred Tank Reactor
DC	Direct Current
DNPH	Dinitrophenylhydrazine
DNT	Dinitrotoluene
DNX	Hexahydro-1,3-dinitroso-5-nitro-1,3,5-triazine
DoD	Department of Defense
DSE	Dimensionally Stable Electrode
e⁻Barrier	Electrolytic Permeable Reactive Barrier
EDS	Energy Dispersive X-ray Spectroscopy
EPA	Environmental Protection Agency
ER	Eley-Rideal
ESTCP	Environmental Security Technology Certification Program
FEW	F.E. Warren Air Force Base
HPLC	High-Performance Liquid Chromatography
HMX	Octahydro-1,3,5,7-tetranitro-1,3,5,7-tetrazocine
LHHW	Langmuir-Hinshelwood Hougen-Watson
MCL	Minimum Contaminant Level
MDL	Method Detection Limit
MNX	Hexahydro-1-nitroso-3,5-dinitro-1,3,5-triazine
MQL	Method Quantitation Limit
MS	Mass Spectroscopy/Spectra/Spectrometer
PCD	Pueblo Chemical Depot
PFR	Plug Flow Reactor
PRB	Permeable Reactive Barrier
RDX	Hexahydro-1,3,5-trinitro-1,3,5-triazine
RPD	Relative Percent Difference
RTD	Residence Time Distribution
SEM	Scanning Electron Microscopy
SHE	Standard Hydrogen Electrode
Ti/MMO	Mixed Metal Oxide Coated Titanium Electrode
TNT	Trinitrotoluene
TNX	Hexahydro-1,3,5-trinitroso-1,3,5-triazine
UV	Ultraviolet Spectrophotometer/Spectra